Fibre Bragg Grating and Long Period Grating Sensors in Polymer Optical Fibres

Bundalo, Ivan-Lazar; Bang, Ole; Nielsen, Kristian

Publication date:
2017

Document Version
Publisher's PDF, also known as Version of record

Fibre Bragg Grating and Long Period Grating Sensors in Polymer Optical Fibres

Ivan-Lazar Bundalo
Ph.D. Thesis

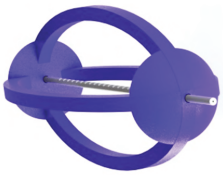

DTU Fotonik
Department of Photonics Engineering
Technical University of Denmark
Ørsteds Plads 345V
DK-2800 Kgs. Lyngby
Denmark

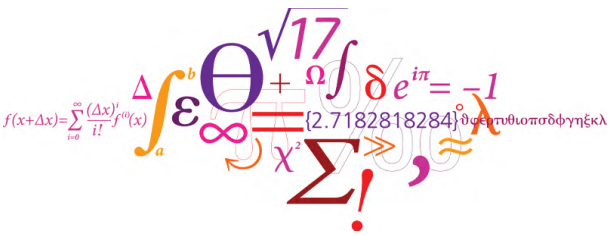

January 2017

Preface

A

This thesis is submitted for the degree of Doctor of Philosophy to the Technical University of Denmark. This PhD-project was prepared by the author between March 2013 and October 2016, and has been carried out as part of the Institute funded project.

The supervisors were:

- Prof. Dr. Ole Bang, Department of Photonics Engineering, Technical University of Denmark, Kgs. Lyngby, Denmark
- Dr. Kristian Nielsen, Department of Photonics Engineering, Technical University of Denmark, Kgs. Lyngby, Denmark

The PhD-project also included a five-month external stay at University of Sydney, Sydney, Australia during which time the progress was supervised by:

- Prof. Dr. Alexander Argyros, Department of Physics, University of Sydney, Sydney, Australia

The goal of the project was to advance the technology of Fibre Bragg Gratings (FBG) in all-solid polymer optical fibres (POF). More precisely, the project was to perfect the FBG fabrication technology in different plastic fibres and to develop various aspects for the commercial application of the technology. The majority of the project was carried out at the Technical University of Denmark, at Institute of Photonics Engineering (DTU Fotonik) where the development was focused on advancing the FBG technology and developing an optical microphone. In the department of Physics at the University of Sydney, the development was focused on Long Period Grating fabrication and development of a pressure based endoscope.

For the analysis of the data, codes were developed in Matlab and in Labview. Citations are indicated by number and the full list of citations is positioned in the last section of the thesis.

All Figures are made by the author unless otherwise stated. Furthermore, a list of abbreviations is located after the conclusion. A few appendices are attached and are referenced within the relevant sections.

Copenhagen, September 30th , 2016

Ivan-Lazar Bundalo

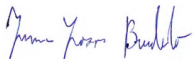

Acknowledgements

I would like to thank all of my supervisors for their support, suggestions, guidance and for making this project possible. I would like to thank my mentor and main supervisor Prof. dr. Ole Bang for giving me the position in the first place, for supporting me in number of ways when I didn't know how to continue, when no exits were apparent – even if that meant sending me to another university to learn. Even though the budget of my institute founded project was much smaller than the budget of my fellow EU funded TRIPOD colleagues, you made sure I was included in all the TRIPOD project meetings, workshops and events, giving me more than fair opportunity to grow and learn on many levels. That was an opportunity for my personal growth also, and I certainly will not forget it.

I have to give my deep thank you to my co-supervisor dr. Kristian Nielsen who was always fresh with ideas, hopeful, cheerful and pushy when things were stuck and annoying. It was truly great experience to work besides you in the lab, I remember well the feeling I had during many of our (sometimes late night) talks about life, science, technology and others. I will miss my Ph.D. for times like these.

During my 4 months stay in Sydney, Australia, I had the opportunity to learn a lot from prof. dr. Alexander Argyros. I never had a more practical, resourceful, engaged and lab-helping supervisor to work with. I learned a great deal from you about how to brainstorm and approach problems from different angles.

I had the opportunity to visit labs at Aston University and at Cyprus University of Technology (CUT) where prof. dr. David J. Webb and prof. dr. Kyriacos Kalli allowed me to work with them and their students. After experience I acquired at Aston, my Ph.D *de facto* started, and at CUT I discovered how fast things can move with good preparation. Both things I found indispensable for good final outcome of my Ph.D.

I am thankful that I had great colleagues and partners to work with in the lab: Getinet Woyessa, Hafeez Ul Hassan, Christos Markos and Alessio Stefani (for the short time you were here, you were indeed helpful) – that lab where the light was mostly off was not so dark with you around. And for the office guys, Søren Michael Mork Friis and Christian Rosenborg Pedersen, with whom I spent most of the time cracking jokes and discussing all sorts of possible and impossible topics, I will miss the relaxed atmosphere we had.

To Antoni Torras Rosell and Denis Ganziy I owe sincere gratitude for giving me a considerable amount of their time, for getting the necessary equipment and components (such as professional microphone membranes), and for understanding and developing POFBG microphone. It was not an easy task but it was interesting every step of the way.

Since I was very active with OSA, SPIE and EPS student Chapters, I have to say big thank you to all the guys with whom I had the chance to plan and organise events with. Among them a special thank you goes to Miranda Mitrovic, Niels-Kristian Kjøller and Kasper Meldgård Røge. Dara McCutcheon and Dragana Vukovic, I spent a lot of time with you in labs, on lunches, in and out of institute, it was always a pleasure to hang out with you and share thoughts on research life.

Now since I started expanding my thanks, I have to thank also my friends in Denmark, especially closest ones (Dhushyanthini, Medina and Pavle) who listened to my moaning when times were hard. Or who did not, and they stopped me. Thanks for that too!

And finally, I would like to thank my family, to all of my brothers and sisters (there is enough space so I can count you all in): Marta, Filip, Sara, Damjan and Jeremija, for supporting me whenever I needed it, despite that sometimes I was even half a world away from home. Special thank goes to my parents, Rajko and Ljiljana - you were always present, always encouraging and ready to skype, giving me the feeling that I was always near, like if I never left home.

Abstract

B

The work presented in this thesis focuses on improving the fabrication of Fibre Bragg Gratings (FBGs) and Long Period Gratings (LPGs) in microstructure polymer optical fibres (mPOF). It also focuses on exploring new options for biomedical and acoustic sensing with the purpose of expanding the range of applications and pushing the limits. The first part of the work focuses on the fabrication of FBGs in polymer optical fibres. FBGs are a periodic perturbation of the refractive index of the optical fibre core which act as a wavelength specific reflector. The fibres used are made of Polymethyl methacrylate (PMMA) polymer, they are microstructured with a hexagonal 3-ring air-hole structure. FBG is inscribed through a Phase Mask technique where a Phase Mask is a piece of glass with a periodically corrugated surface on the nanometric scale. When the laser light passes through it, it creates diffraction orders which will interfere with each other and together form a periodic pattern. PMMA is an intrinsically photosensitive material, which changes its refractive index upon radiation at UV wavelengths. The PMMA fibre is positioned just below the phase mask so its core refractive index is periodically altered creating a Bragg grating with peak reflection wavelengths at 650 nm or 850 nm, depending on the phase mask. As part of this work the FBG inscription system was optimised. The optimisation routine is presented and after the optimisation inscription time is reduced to just a few minutes, a considerable improvement with respect to previous inscriptions. The influence of the laser intensity on the inscription of the gratings is also demonstrated.

For step index fibres the inscription is a straightforward process. For microstructured PCFs however, the holey cladding region is making it difficult for inscription light to reach the core. The hexagonal holey structure in the cladding is shown to have certain angles, where the strong grating is formed in a short time. At the unwanted angles, grating was not formed at all, or being of a very poor quality, proving the importance of fibre orientation for the inscription.

As polymers are viscoelastic materials, they have properties of both viscous and elastic materials. Therefore, the investigation of long-term strain behaviour of a free-standing,

unembedded polymer optical FBG (POFBG) sensor is presented. It shows that after straining polymer fibre sensor at certain strain level, the relaxation of the fibre happens in two phases, defining two wavelength ranges. The two ranges are called fast relaxation range ($\Delta\Lambda_{fast}$) and slow relaxation range ($\Delta\Lambda_{slow}$). $\Delta\Lambda_{fast}$ is the part with higher strains and in this range fibre behaves generally elastically – it responds instantaneously to the changes in the applied strain. The $\Delta\Lambda_{slow}$ is the wavelength range at lower strain levels, near the complete relaxation of the fibre, and in it the fibre is behaving generally viscously. Fibre sensor operating in the slow range cannot relax fast enough and experiences a time lag. The amount that these two ranges take of the total strain range depends on four factors: strain amount, strain duration, relaxation duration, and the number of cycles that sensor was strained and relaxed. Their dependency is reciprocal - as one increases the other one decreases: the $\Delta\Lambda_{slow}$ increases with strain amount, strain duration, increasing number of cycles, and it decreases with relaxation duration. For strains up to 0.9%, fast relaxing $\Delta\Lambda_{fast}$ range takes no less than 65% of the total strain range. Increase in $\Delta\Lambda_{slow}$ due to cyclic straining and relaxing seems to reach an equilibrium value, suggesting that $\Delta\Lambda_{slow}$ would never cover the whole strain range. When increasing the strain to 4.9%, the relative amount of $\Delta\Lambda_{slow}$ grows with respect to $\Delta\Lambda_{fast}$, but so does the absolute amount of $\Delta\Lambda_{fast}$. With the proper prestrain covering $\Delta\Lambda_{slow}$, the free standing FBG fibre sensor could operate in "real-time" entirely in $\Delta\Lambda_{fast}$. It would have the highest sensing range around 3%.

In the last part of the FBG section, a simple fibre FBG microphone is investigated, and the influence of a membrane amplifier on sound detection is also investigated.

In the last part of the thesis the LPG inscription system is shown. In this system a high power CO_2 laser is used for the inscription. An LPG is also a periodic perturbation of the guided core mode in fibre, but unlike FBG which reflects the core mode, the LPG couples the core mode to a cladding mode outside the core. We have shown that the LPG grating can be formed through two mechanisms in polymer fibres using a CO_2 laser. One is etching and the other one is perturbation of the microstructured region.

After inscription of LPGs, the concept of a biocompatible distributed medical endoscope is presented, where an all-plastic LPG based device is produced. A transducer pod is made which translates the outside pressure into strain on the fibre. The transducer consisted of a 3D printed skeleton through which the fibre is pulled. A latex material is then wrapped around it and all the holes were sealed in order to prevent the air from leaking out. The pod transducer was tested for forces acting on its arms, and subsequently put into a pressure chamber. It showed good initial results for pressures up to 150 mBars, proving itself suitable as a potential biocompatible endoscope.

Résumé in Danish

C

Denne afhandling præsenterer arbejde med fokus på at forbedre fabrikationen af fiber Bragg gitre (FBG) og lang-periode gitre (LPG) i mikrostrukturerede polymer optiske fiber (mPOF). Der er også lagt fokus på undersøgelsen af nye muligheder indenfor biomedicinsk og akustisk måling med det formål at identificere nye anvendelser og flytte på grænserne for hvad der er muligt med teknologien.

Første del omhandler fabrikationen af FBG i polymer optiske fibre. FBG er en periodisk variation af fiber-materialets brydningsindeks, hvilket medfører en bølgelængde afhængig refleksion af lys. De anvendte fibre er lavet af polymeren polymethyl methacrylate (PMMA), og har en photonic crystal fiber (PCF) struktur med tre ringe af lufthuller placeret i et hexagonalt mønster omkring kernen. En 50 mW HeCd laser med en bølgelængde på 325 nm er anvendt til inskription af gitrene via fase maske teknikken. En fase maske er et stykke glas med en periodisk rillet overflade på nanometrisk skala. Når laserens lys passerer igennem strukturen spredes lyset ud via diffraktion i forskellige diffraktions-ordner, der indbyrdes vil vekselvirke og til sammen danne et periodisk interferensmønster. PMMA er et naturligt fotosensitivt materiale, som ændrer brydningsindeks ved bestråling af UV lys. PMMA fiberen er således placeret under fase masken så kernen udsættes for en periodisk ændring af brydningsindekset, og derved dannes et Bragg gitter med maksimum refleksion ved 650 nm eller 850 nm alt afhængigt af fase masken. Som en del af dette arbejde blev FBG inskriptionssystemet optimeret. Optimeringsproceduren bliver præsenteret hvorefter inskriptionstiden blev reduceret til et par minutter, hvilket er en væsentlig forbedring i forhold til tidligere. Betydningen af laserens intensitet på gitterinskriptionen bliver ligeledes demonstreret.

For step indeks fibre er inskriptionen ligetil. For mikrostrukturerede PCFer derimod besværliggøres inskriptionen af kappen af lufthuller, der blokerer for lysets adgang til kernen. Den hexagonale hulstruktur i kappen er blevet påvist at have særlige vinkler, for hvilket et stærkt gitter kan dannes på kort tid. Ved uhensigtsmæssige vinkler bliver der enten ikke

indskrevet et gitter, eller også bliver gitteret af lav kvalitet, hvilket er med til at understrege vigtigheden i at orientere fiberen korrekt før inskriptionen.

Da polymerer er viskoelastiske materialer har de både viskøse og elastiske egenskaber. Derfor præsenteres en undersøgelse af langtidsstræk-påvirkningen af en fritstående polymer optisk FBG (POFBG) sensor. Det påvises at efter sensoren er blevet strækket til en vis grad sker den efterfølgende afslapning af fiberen i to faser, der hver defineres ved et bølgelængdeområde. De to områder benævnes hurtig afslapning ($\Delta\Lambda_{\mathrm{fast}}$) og langsom afslapning ($\Delta\Lambda_{\mathrm{slow}}$). $\Delta\Lambda_{\mathrm{fast}}$ er den del med højt strækniveau i fiberen, og i dette område opfører fiberen sig generelt elastisk – det vil sige den reagerer øjeblikkeligt i forhold til ændringer i det påførte stræk. $\Delta\Lambda_{\mathrm{slow}}$ sker for lavt strækniveau tæt på fiberens hvilepunkt, og fiberen opfører sig således mere viskøst. Fiber sensorer der opererer i dette strækområde kan ikke hurtigt komme til hvile, og oplever derfor en tidsforsinkelse. Forholdet mellem de to strækområder afhænger af fire faktorer: mængden af stræk, varigheden af strækket, varigheden af afslapning og antallet af gange sensoren er blevet strækket og afslappet (cyklus). Deres indbyrdes afhængighed er reciprok, dvs. at hvis den ene stiger bliver den anden mindre. $\Delta\Lambda_{\mathrm{slow}}$ stiger med mængden og varigheden af strækket, samt antallet af cyklusser, og mindskes med varigheden af afslapning. For stæk op til 0.9 % udgør $\Delta\Lambda_{\mathrm{fast}}$ ikke mindre end 65 % af det totale stræk. Stigningen i $\Delta\Lambda_{\mathrm{slow}}$ pga. cyklisk stræk og afslapning når efterhånden en ligevægtsværdi, hvilket antyder at $\Delta\Lambda_{\mathrm{slow}}$ aldrig kan udgøre hele det samlede stræk. Når strækket øges til 4.9 % stiger forholdet mellem $\Delta\Lambda_{\mathrm{slow}}$ og $\Delta\Lambda_{\mathrm{fast}}$, men ligeledes stiger den absolutte værdi af $\Delta\Lambda_{\mathrm{fast}}$. Med et passende præ-stræk der dækker $\Delta\Lambda_{\mathrm{slow}}$ vil den fritstående FBG sensor være i stand til at operere i ”real-time”, altså udelukkende i $\Delta\Lambda_{\mathrm{fast}}$. Den ville have den højest mulige måleråkkevidde på omkring 3 %.

I den sidste del af FBG kapitlet undersøges en simpel FBG mikrofon, og påvirkningen af en membran-forstærker på detektionen af lyd bliver ligeledes undersøgt.

I den sidste del af afhandlingen vises LPG inskriptionssystemet. I dette system benyttes en høj-effekts CO_2 laser. Et LPG er ligeledes en periodisk påvirkning oplevet af lyset i kernen af fiberen, men i modsætning til FBG, der reflekterer kernelyset, kobler LPGen lyset i kernen til

kappen. Vi har påvist at et LPG kan dannes via to mekanismer i polymerfibre ved brug af en CO_2 laser. Den ene er ved ætsning og den anden er ved påvirkning af den mikrostrukturerede region.

Efter inskription af LPGer præsenteres konceptet om det biokompatible distribuerede endoskop, hvor et komplet plastisk LPG apparat fremstilles. En transducer er fabrikeret for at oversætte det omgivende tryk til stræk af fiberen. Transduceren bestod af et 3D-printet skelet hvorigennem fiberen er trukket. Et latex materialer er derefter viklet omkring transduceren og samtlige huller forseglet for at undgå lækage af luft. Transduceren blev derefter testet i kræfter påført på armene af strukturen, og anbragt i et trykkammer. De umiddelbare resultater var gode for tryk op til 150 mBar, hvilket beviser dens nyttighed som et potentielt biokompatibelt endoskop.

Contents

List of Publications

E

Journal Publications

1. I.-L. Bundalo, K. Nielsen, C. Markos, and O. Bang, "Bragg grating writing in PMMA microstructured polymer optical fibers in less than 7 minutes," Opt. Express **22**(5), 5270–6 (2014).
2. I.-L. Bundalo, K. Nielsen, and O. Bang, "Angle dependent Fiber Bragg grating inscription in microstructured polymer optical fibers," Opt. Express **23**, 3699-3707 (2015)
3. I.-L. Bundalo, R. Lwin, S. Leon-Saval, and A. Argyros, "All-plastic fiber-based pressure sensor," Appl. Opt. **55**(4), 811 (2016).
4. I.-L. Bundalo, K. Nielsen, G. Woyessa, and O. Bang, " Long-term strain response of polymer optical fiber FBG sensor" (in preparation 2016).

Conference proceedings

5. I.-L. Bundalo, K. Nielsen, and O. Bang, "PMMA mPOF Bragg gratings written in less than 10 min.", Proceedings of Photonics Europe 2014 conference, SPIE. Vol. 9128 SPIE - International Society for Optical Engineering, 2014. p. 91280O.
6. I.-L. Bundalo, K. Nielsen, and O. Bang, "Fast Fiber Bragg Grating Inscription in the Undoped Microstructured Polymer Optical Fibers", Abstract from Danish Optical Society Annual Meeting 2014, Denmark.
7. I.-L. Bundalo, K. Nielsen, and O. Bang, "Analysis of the Angle Dependency in Inscription of the Fiber Bragg Gratings in the Microstructured Polymer Optical Fibers", Proceedings of CLEO Europe 2015, Munich Germany.
8. I.-L. Bundalo, K. Nielsen, and O. Bang, "Pmma fiber viscoelasticity in extremely low frequency regime", 24th International Conference on Plastic Optical Fibers, Pof 2015 - Conference Proceedings. 2015. p. 257-260, Nuremberg, Germany.
9. I.-L. Bundalo, R. Lwin, S. Leon-Saval, and A. Argyros, ", "LPG based all plastic pressure sensors", 24th International Conference on Plastic Optical Fibers, Pof 2015 - Conference Proceedings. 2015. p., Nuremberg, Germany.
10. I.-L. Bundalo, K. Nielsen, G. Woyessa, and O. Bang," Long term strain behavior of PMMA based polymer optical fibers" Proceedings of SPIE. Vol. 96347Y SPIE - International Society for Optical Engineering, Curitiba, Brazil 2015.

Chapter

1 Introduction

The field of optical fibre sensing has been around for about 40 years. Optical fibre sensing has the potential for making small, low cost and lightweight sensors, which are easily multiplexable and are immune to Electromagnetic Interference (EMI) [1]. Fibre sensing possibilities started emerging from the very beginning of optical fibre development with the majority of the fibre sensing technology development being based on silica fibres.

However, in recent years, the development has been slowly gaining pace also in plastic fibres, with the dawn of novel applications, price and potentials unreachable with other materials. The developments of microstructured polymer optical fibres (mPOFs) in 2001 [2] as well as first inscriptions of Fibre Bragg Grating (FBG) in mPOF induced the faster development of the field.

1.1. Optical Fibres

Optical fibres can be described as an optical counterpart to (copper) electrical wires, they are optical waveguides mostly used for communications but also for lighting and entertainment. An optical fibre is a thin piece of optically transparent material such as glass or plastics, which acts as a pipe through which light travels. At the fibre facets, light can go inside and outside of the fibre while the fibre's cladding (a pipe) confines the light to the core of the fibre. The development of the fibre technology started in the 1950s with one of the first fibres being made from polymer [3]. In the following years, the intrinsically higher loss that polymer fibres have over silica (glass) based ones, pushed the development of silica fibres forward in comparison to polymer fibres. The theoretical minimum attenuation of silica fibres lies around 0.15 dB/km at 1550 nm wavelength [4] which is almost the practical limit achieved nowadays. This fundamental minimum is a wavelength window, defined by the Rayleigh scattering at short wavelengths (visible wavelengths towards UV) and several absorption mechanisms at long wavelength (visible towards infrared). These absorption mechanisms at long wavelengths are impurities and absorption due to water vibration levels. The more detailed table showing loss mechanisms in optical fibres are shown in Table 1. Regarding polymer fibres, the limiting factor at lower wavelengths is again the Rayleigh scattering, which increases proportionally to λ^{-4}. At higher wavelengths, the carbon-hidrogen bond vibrational levels make absorption bands which limit the transmission at long wavelengths (starting around 800nm). This Carbon-Hidrogen bond is a basic constituent of polymers which makes it impossible to overcome this limit, as it is impossible to limit Rayleigh scattering. These two mechanisms define a minimum loss region of around 550 nm (see Figure 1-1). The hydrogen atoms can be substituted by some heavier elements, which will shift the excitation of vibrations towards higher levels. That process effectively reduces the loss and extends the low loss band. However, the process is expensive and often chemically dangerous which limits its use in the production of polymer fibres.

The polymers most commonly used for production of optical fibres are the amorphous (non-crystalline) fluoropolymer CYTOP, and the predominantly used poly(methyl

methacrylate) or PMMA [3]. The theoretical lowest loss is about 0.3 dB/ km at 1300 nm [5,6] which is very close to the loss of silica. However, the lowest loss measured in a polymer fibre is about two orders of magnitude higher; 10 dB/km at around 1100 nm wavelength, in a CYTOP graded index fibre.

Table 1: Different loss mechanisms in optical fibres, as presented in Cusano *et al.* [7].

Type of Mechanism	Mechanism	Origin
Intrinsic	Absorption	Vibration modes
		Electronic transitions
	Rayleigh scattering	Density Fluctuations
		Orientation Fluctuations
		Composition Fluctuations
Extrinsic	Absorption	Organic pollutants
		Dust
	Scattering	Micro-fractures
		Bubbles
		Core-cladding fluctuations
	Out-coupling loss	Micro and macro bends

The loss over wavelength for silica (glass) fibre, PMMA and CYTOP is presented in the Figure 1-1.

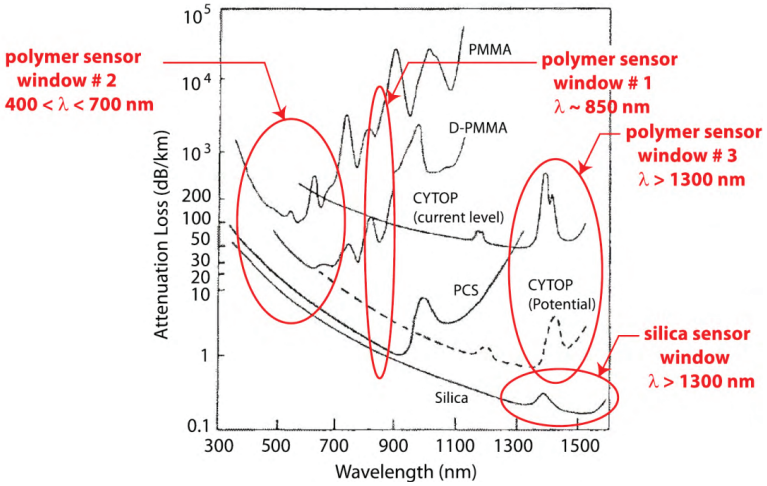

Figure 1-1. Attenuation loss of common optical polymers as a function of wavelength (taken from Kara Peters [8])

The polymer optical fibres are generally produced through two methods. Both methods involve a draw tower. The first method is similar to the way silica fibres are made; a solid preform with the desired structure, is scaled down by drawing. In the other method, the polymer fibre can be drawn directly from a liquid state. The liquid can be unpolymerised material or melted polymer. Drawing the fibre from the preform is a more common practice; the preform has a desired radial structure with a refractive index profile that determines light guidance (see Figure 1-3). In case of microstructured fibres, the cane is drilled to have a desired holey structure (see Figure 1-3).

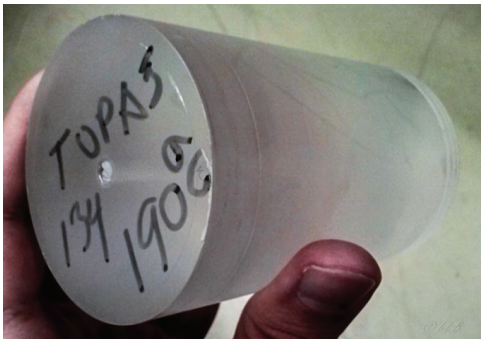

Figure 1-2. Preform for polymer step-index fibre (presented with permission from Andrea Fasano). The cladding was made of Zeonex 480R. The core is 4 mm in diameter, material was TOPAS 134C, it was injection moulded inside the cladding material.

For all-solid POF, step or graded index profile performs, the desired refractive index is achieved by using dopants/dyes, by centrifuging during polymerization or by using two different polymers (in which case their mechanical properties should be similar) [3]. Step index polymer fibres are usually made with the latter technique, which allows for a high refractive index difference. Drawing a preform into a polymer fibre is usually a two-step process. In the first step, the preform is heated above the glass transition temperature of the polymer. As the preform in the hot-zone heats above the glass transition temperature, the polymer becomes a viscous half-liquid, the gravity will then pull the lower part of the preform and between the dropping lower part and the remaining preform a thin cane or fibre is made. After that, the desired thickens of the cane or the fibre is achieved by controlling temperature and drawing speed. Polymer fibres can be directly drawn from preforms but due to delicate procedure requiring high control of temperature, tension and drawing speed, it is easier to draw it in a two-step process. In the first step a preform is firstly drawn to cane, which is about half a centimetre in width and one meter in length. The cane is then again fed into the fibre drawing tower, just like preform before, and drawn into the fibres of desired thickness.

Figure 1-3. Example of a polymer preform used to draw a microstructured antiresonant fibre.

The Numerical Aperture (NA) is a number which characterises the range of angles over which the system can receive or release light. For a step-index fibre it can be defined as the difference between the core and the cladding effective refractive indices:

$$\boldsymbol{NA = \sqrt{n_{core}^2 - n_{cladding}^2} = n_{air}\, sin\Theta_{air}} \qquad (1)$$

The NA determines acceptance angle Θ of the light entering or exiting the fibre as presented in Figure 1-4, and together with the core dimensions determines confinement of light or guiding properties of the fibre. The normalized frequency, or V parameter, gives the information about the number of optical modes that can propagate in the fibre. It is directly related to the NA through:

$$\boldsymbol{V = NA\frac{2\pi a}{\lambda}} \qquad (2)$$

Where a is a diameter of the fibre core and λ is a free space wavelength.

For many applications, the few- or single-moded fibre is desired (the behaviour achieved for ≤ 2.405) if not even an imperative. To reduce the number of modes of the fibre we need smaller Numerical Aperture (small refractive index difference) and a small core. Both of these are quite hard to achieve in fabrication. Firstly because it is hard to control the manufacturing process, and because a small core increases the loss due to scattering at the interfaces. In

addition to that, V is dependent on wavelength, and the low loss window of polymer fibres is at lower wavelengths which again increases the normalized frequency. Manufacturing single-mode polymer fibre is therefore a difficult task.

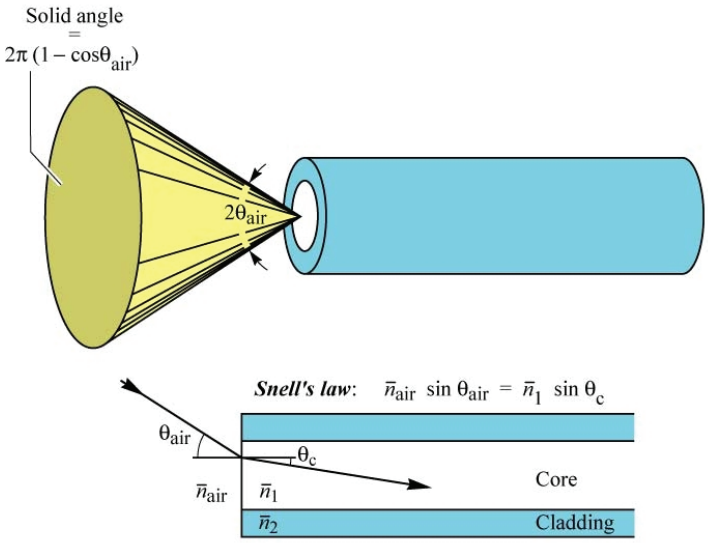

Figure 1-4. Illustration of the Numerical Aperture (NA) of a step index fibre adopted from [9]. The NA determines the acceptance angle **Θ** of the light which can propagate through the fibre.

However, for some short-range communication applications, such as FTTx (Fibre To The Home, Building, Business, Desktop, Node, etc.), fast business and home networks, the single mode fibres are not necessary and thick multimode POF fibres are sometimes desired [10–13]. The low cost highly multi-mode fibres are of great interest as the need for the low cost is more important than capability for high data transmission given by single mode fibres. These fibres are usually graded index fibres being 0.5-1 mm thick.

The low cost of production and higher flexibility of the polymer materials in comparison to silica are the main reasons for the recent fast development of polymer fibres. Some of the advantages that POFs hold over their silica counterparts are the lower Young modulus, the lower density which makes it lighter than glass, the higher strain breaking limit (10% compared to about 1% in silica [14]) and biological compatibility [7]; each of these properties open possibilities for various sensing applications. For instance, silica fibres have a Young modulus

of about 72 GPa [15] while a POF made of PMMA (polymethyl methacrylate) has a Young modulus of about 2-3 GPa (the exact Young modulus depends on the drawing conditions [3,16–18]), which is about 30 times smaller than that of silica. The high elastic yield is particularly valuable when measuring large material stresses, bendings and strains under which silica fibre would normally break.

Further differences between silica and polymer fibres include failure strain. Silica fibre typically has a failure strain of about 5-10%, for the polymer fibres failure strains of over 100% were reported [14]. However, this is strongly dependent on the fibre production process where the slightest mechanical damage to the silica fibre surface can lower this percentage. Polymer fibres failure strain also depends strongly on drawing conditions (usually done between 100°C and 180°C), but it is possible to improve its tensile properties through the process of annealing. By annealing the fibre, the fibre is subject to an elevated temperature of around 80°C [19] for several hours in order to release built in stress from the drawing process. The limit of quasi-elastic behaviour of POF is around 6% [14]. For certain in-vivo applications polymer fibre is preferred as upon breakage it does not produce dangerous debris.

1.2. Microstructured Fibres

Microstructured fibres are commonly single-material fibres; the light is not confined in them by conventional refractive index difference between the two materials but their guiding properties are determined by hollow cores going along the fibre length. As their guiding properties are based on properties of photonic crystals, they are also called Photonic Crystal Fibres or PCFs. They have been demonstrated for the first time in silica fibres in 1996, with fibre consisting of a pure silica core surrounded by a silica – air photonic crystal material having a hexagonal symmetry [20].

The microstructured fibres can be divided into two classes depending on the guiding principle: total internal reflection (TIR) based, or so-called index-guiding, and photonic bandgap guiding. The latter are based on the absence of solution to Maxwell's equations for the electromagnetic field in the cladding, which as a result forces the light to remain in the core.

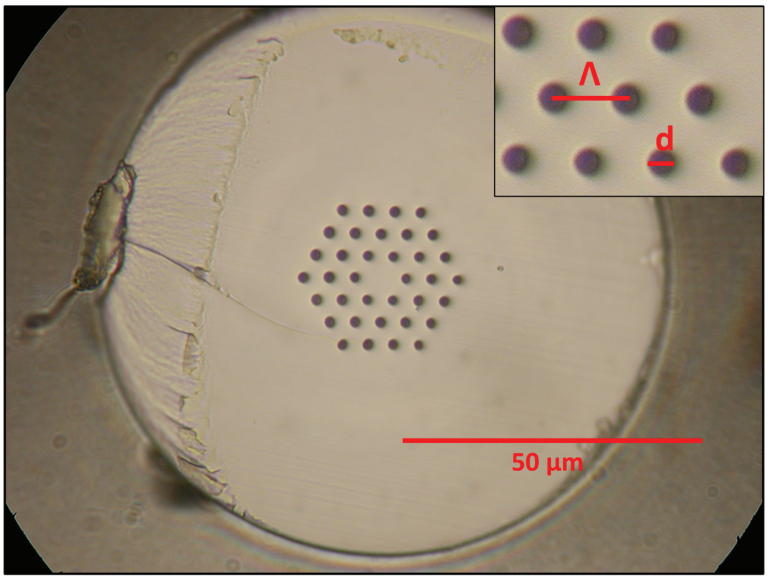

Figure 1-5. Microscope image of a 180 µm microstructured polymer optical fibre facet. The inset image is a zoom-in to the microstructure region. The ratio between the hole diameter d, and the pitch (distance between the holes) Λ is 0.32, which makes this fibre endlessly single mode according to equation (3).

With photonic crystal structures, it is possible to tailor the dispersion and it is also possible to make the fibre endlessly single mode. That means that the fibre can be used for single mode guidance over a broad range of wavelengths and that the fibre can be single moded with bigger core.

In TIR based microstructured fibres the holey area effectively reduces the refractive index of the cladding. The endlessly single mode guiding is achieved independently of the fibre material [21], through carefully designed hexagonally spaced circular holes as presented in Figure 1-5, to be:

$$\frac{d}{\Lambda} < 0.42 \qquad (3)$$

The first microstructured polymer optical fibre, commonly denoted mPOF, was reported in 2001 by Van Eijkelenborg *et al.* [2]. The preform for the mPOF can be made by drilling the bulk cylinder of desired plastic, extruding or casting it, or by stacking tubes, similar to the method used when producing silica PCFs. This enables the development of specific fibres for each application as it allows for many different microstructure designs. Probably the most common design of mPOF fibres is that of hexagonal structure with equally spaced holes as shown in Figure 1-5. The higher number of hexagonal rings increases the confinement of the light to the core and therefore lowers confinement loss. While the uniform hexagonal structure is probably the most common design for mPOFs, different designs have been suggested and fabricated allowing unique properties. Some of them are hollow core fibres [22,23], high birefringence fibres [24], twin core and rectangular core [22], multi core [25], graded index mPOF [22,26], randomly microstructured fibre [27] and suspended core fibres [28]. Regarding mPOFs, they have been made from PMMA [2] most commonly, but also from Topas [29–31], Polycarbonate [32] and biodegradable materials [15].

1.3. Fibre Bragg Gratings

For the last three decades Fibre Bragg Grating (FBG) technology has been continuously developed and has matured enough to have its place among standard optical components in sensing [33], telecommunication and lasers [34]. A Fibre Bragg Grating (FBG), in simple words, is a mirror for a narrow band of colours (wavelengths) passing through optical fibre. It is transparent for other wavelengths, which pass unchanged through the fibre. This wavelength-specific, mirror-like effect is achieved by creating a periodic change in the effective refractive index of the fibre core. If the wavelength propagating through the FBG has a period which is a multiple of the period of the Bragg Grating, such that all the reflected components interfere constructively (while forward waves have destructive interference), the wavelength will be reflected. For the case of a constant periodical index modulation, the backward constructive interference occurs in a narrow range of wavelengths around the Bragg condition which can be written down as:

$$\boldsymbol{\lambda_{light} = 2n_{eff}\,\Lambda_{Bragg}} \qquad (4)$$

Where λ_{light} is the wavelength of a light reflected by the FBG, n_{eff} is the effective refractive index of the core mode and Λ_{Bragg} is the period of the refractive index modulation.

The first Fibre Bragg Grating was made in 1978 by Hill *et al.* [35], by two coherent counter-propagating beams, forming a standing wave, inside the silica fibre. The fibre was first doped with germanium to increase photosensitivity of the fibre, which made this experiment also the first of a kind, demonstrating the photosensitivity of the material to UV light. The importance of the finding was soon after recognised, but only about ten years later the discovery was put to practical use [12]. Doping with germanium (increasing the amount of it in the fibre core) is a standard and very common procedure to enhance photosensitivity. Beside it, the fibre can be doped with germanium-boron, doping of the cladding as the refractive index gets lower; and it can be high-pressure hydrogenated, a procedure known as hydrogen loading, in which

case the loss increases due to formation of hydrogen ions [12].

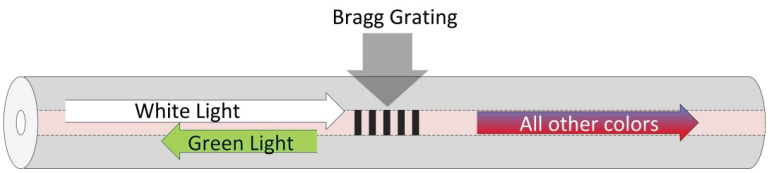

Figure 1-6. Scheme of a fibre having Fibre Bragg Grating. On the broadband (white) incoming light, FBG will reflect only colours which satisfy equation (4)

Inscription of FBG is commonly done through one of the following methods:

Phase Mask technique- as presented in Figure 1-7, a quartz glass with fixed corrugated surface is used for UV inscription of gratings [36]. Bragg wavelength tuning is limited to a small range of wavelengths determined by the corrugations pitch.

Interferometric technique – two coherent beams are used for tailoring the desired wavelength. This technique gives greater flexibility on the resulting grating wavelength [37].

Point-by-point inscription technique – single and two photon absorption (e.g. with Ti:sapphire femtosecond laser) is used for inscription of Fibre Bragg gratings, one groove at the time. It allows for greatest flexibility in determining the pitch and the profile of the refractive index change, such as chirp, and it does not require photosensitivity - fibre can be undoped [38,39].

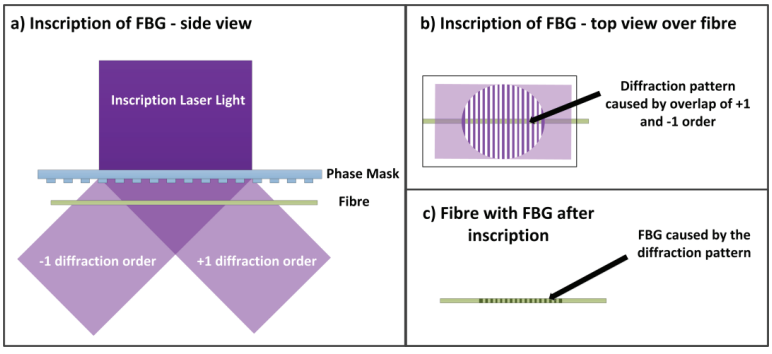

Figure 1-7. A schematic showing phase mask diffraction which is used to create FBG on the fibre bellow the phase mask. In this case, interference of the +1 and -1 order create a pattern which creates FBG

Depending on the photosensitivity mechanism by which the changes of the refractive index are produced in a fibre, there are up to 5 (6) types of Fibre Bragg gratings that have been reported [37], such as type I, type Ia, type II etc.. Different types of Fibre Bragg gratings yield different physical attributes of the produced grating, especially temperature dependency and high temperature response.

Fibre Bragg gratings are used particularly in communications, as wavelength filters, in fibre lasers as reflectors, as chromatic dispersion compensators, mode converters and as sensors [12,40].

1.3.1. Fibre Bragg Gratings in Microstructured Polymer Optical Fibres

In comparison to silica which has very low photosensitivity, polymers have intrinsic photosensitivity, which was reported for the first time in 1970 by Tomlinson *et al.* [41]. He recorded the change of the refractive index in PMMA when exposed to the UV light at 325 nm. It took almost 30 years until, in 1999, Xiong *et al.* [42] produced the first Bragg grating in polymer fibre. The underlying mechanism guiding photosensitivity of polymers was a matter of discussion for a long time. Tomlinson *et al.* suggested [41] that photosensitivity was guided by cross-linking and polymerization under the UV light. In the study by Wochnowski *et al.* [43] the UV effects under short irradiation UV wavelengths at 193 nm and at 248 nm have been investigated presenting changes of the refractive index. The 308 nm wavelength has also been considered but it showed no change of the refractive index. The common FBG inscription wavelength is 325 nm, the HeCd laser emission. In a recent study from Saez-Rodriguez *et al.* [44] the evidence was provided suggesting that the main mechanism guiding photosensivity in PMMA-based microstructured polymer optical fibres under the UV light is a process of both photodegradation and polymerization. When the fibre was increasingly strained under the UV light (325 nm HeCd laser light) it lead to the increased photosensitivity, which is the evidence of photodegradation. Correspondingly, the change in the refractive index of the fibre was measured to be positive, which suggests further polymerization of the material. Depending on

the quality and fabrication process, material composition and preparation, the final result may vary which makes it harder to get a clear picture of the underlying processes.

Bragg gratings have been written in both all-solid and microstructured polymer fibres. The HeCd laser operating at 325 nm is a commonly used continuous wave (CW) laser for grating inscription, with powers ranging from 30-50 mW [36,45,46]. Inscription of FBGs in step or graded index fibre is a straightforward procedure with respect to light reaching the core. Things are more complicated with microstructured fibres as the array of holes surrounding the core hinders the inscription light coming from the side as presented in Figure 1-8. The process is more complicated as more of the light is diffracted from the microstructure [47,48], but with enhanced photosensitivity, such as germanium doping and hydrogen loading, strong grating can still be formed. The first Fibre Bragg grating in microstructured fibre has been successfully inscribed in 1999, by Eggleton *et al.* [49]. The common method is a phase mask technique which minimizes alignment and stability issues.

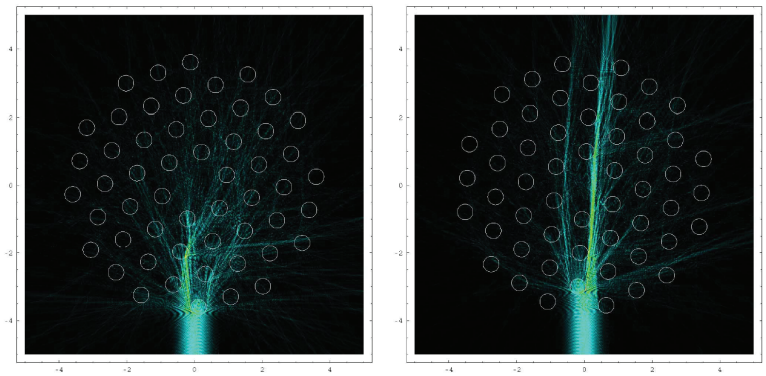

Figure 1-8. Two images showing simulation results of FBG inscription light entering the core of the fibre. Much of the light is diffracted by the air-hole interfaces hindering inscription of the gratings (Marshall *et al.* 2007 [47])

The initial inscription times in PMMA have been lengthy, taking about an hour [7], but with proper alignment and power, they have been lowered to several minutes [36], even in some cases under less than 30 seconds [50]. This fastest inscription was made in mPOF with 248 nm UV radiation with a pulsed laser at low repetition rate, avoiding material ablation. Some of the earlier attempts to speed up the inscription process involved doping the fibre with 10% concentration of benzyl dimethyl ketal (BDK); a photo-initiator which was enhancing UV

induced photo-polymerization [51]. However, the normal photosensitivity is not required in inscription using high-power femtosecond pulse lasers. Grating fabrication with such lasers could ultimately become a standard for on-drawing-tower inscription of gratings [14].

Bragg gratings have been written in many wavelength ranges, starting with telecommunication window at 1550 [52], and to shorter wavelength ranges where polymer has lower loss, such as 850 nm [29,45] and 650 nm [14,53] windows. Fiber Bragg gratings have found applications as tunable filters [54], laser mirrors [55], and biosensing [56].

1.4. Long Period Gratings

A Long Period Grating (LPG) is a periodically changing structure along the fibre, similar to that of a Bragg grating. The period is however, much bigger, on the scale of a millimetre and as a result, Long Period gratings are generally easier to inscribe; they can be written directly into the cladding from the external surface of the optical fibre. While the Bragg grating acts as a mirror for the light propagating through the core mode, the Long Period grating couples the light from the core modes to the co-propagating cladding modes. As light cannot efficiently propagate in the cladding, meaning that it is scattered and attenuated quite fast, the Long Period Grating takes away the core wavelengths which phase-match with its period.

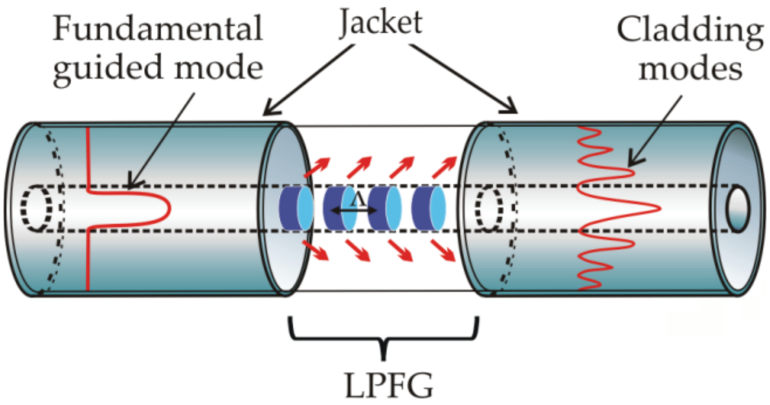

Figure 1-9. Scheme showing working principle of a Long Period Grating. The light propagates through the fibre. For the wavelength whose period is phase matched with the LPG period, upon interaction, LPG changes the modes direction and the core mode is coupled into the cladding mode. As light cannot propagate far through the cladding due to scattering, the LPG acts as a wavelength filter (image taken from Silva *et al.* [57]).

The phase matched wavelengths occur in the transmission spectrum as a loss dip in the spectrum, the coupling wavelength $\boldsymbol{\lambda_{LPG}}$ is given by the phase-matching condition described by the following equation [58]:

$$\boldsymbol{m\lambda_{LPG} = \left(n_{Core}(\lambda) - n^{i}_{Cladding}(\lambda)\right)\Lambda} \qquad (4)$$

With $\boldsymbol{m}$ being the order of coupling, $\boldsymbol{\Lambda}$ is the period of the grating, $\boldsymbol{n^{i}_{Cladding}(\lambda)}$ is the refractive index of the $\boldsymbol{i}$ mode of the cladding, and $\boldsymbol{n_{Core}}$ is the refractive index of the core. If the LPG is exposed to the changes of temperature and humidity, as well as stretched, the parameters of the coupling equation change resulting in the loss wavelength shift at the output end. LPGs have numerous applications such as attenuators, band-pass filters, mode converters, tunable filters, gain-flattenings, temperature and strain sensors [59]. The majority of the work has been done in silica fibres [60–62]; it was difficult to produce single-mode polymer fibres, which has been overcome with microstructured fibres. These gratings are made with periods typically in the range from 100 μm to 1000 μm [63]. LPGs can be fabricated in different ways: LPG can be physically imprinted, made with an electric-arc discharge [61], UV inscribed [64], CO_2 laser inscribed [62], made with acoustic waves [65] and temporary mechanical pressure [66]. In Polymer fibres, LPGs have been physically imprinted [67,68] and UV inscribed [69].

1.5. Optical fibre sensing

Optical fibres found their market at the boundary of telecommunications and optoelectronics. Their development has been mostly driven by telecommunications but they showed potential in applications not covered by telecommunications or optoelectronics. It didn't take long until fibre sensing technology established its own place on the market. The qualities for which it was desirable on the market were relative low cost, light weight and small size, wide bandwidth, rigidity, high sensitivity, immunity to electromagnetic interference and multiplexing ability – in certain arrangements hundreds of sensors can be addressed in a single fibre. The fibre sensors are used in variety of applications, from biomedical monitoring and smart materials to structural integrity monitoring (Figure 1-10).

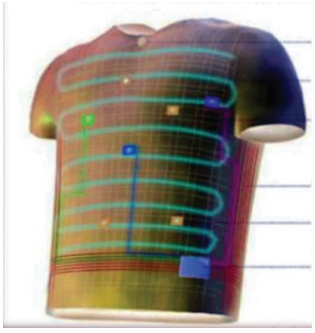

Figure 1-10. Applications of fibre sensors are various; they can be used for monitoring the integrity of building walls and windmill wings, or they can be used for creation of smart materials measuring biosignals such as heartbeats or breathing [7,70–72].

Not less important, the ability of fibre sensors to cover a wide range of applications also made them stand out as multi-purpose sensors. Over the years, fibre sensors have been developed to measure chemical (pH, inorganic and organic compounds) and biological parameters (oxygen and blood glucose concentrations); electric and magnetic fields, position, viscosity, as well as physical parameters such as displacement, stress, temperature, humidity, acceleration, vibrations, pressure, strain, and wind speed [56,70,73].

The fibre sensors can be all-fibre, standalone sensors, or integrated with different components; they use different working principles and materials in configurations that depend on the application. Detection can be based on polarization, spectral detection or amplitude variations. They can be single or multiplexed, local or distributed, embedded and work as interferometers. While silica as a material still holds (weakening) monopoly over the fibre sensing market, fibre sensors are made from other materials such as polymers or other glass materials [70,73,74].

1.5.1. POF sensors

The advantage of polymer as a material makes the fibre sensing in its case rely more on material properties than what is possible with silica. Polymers are stretchable and cheap to produce; they substantially expand with heat, and swell with rising humidity. Probably the biggest market for sensors made of polymer fibre is automotive industry (control, safety, information and entertainment systems [75]), but POF sensors have been used for various applications in other markets as well. Thick multimode polymer fibres are the most used as they are easy to handle. The field where POF sensors find their applications include temperature, humidity, strain, chemical, bio-sensing, geogrids and other [13,56,70,73,75,76]. Single mode fibre has been used in interferometric configuration for ultrasound sensing [77,78], temperature sensing [79] and for strain sensing [80,81]. One of the biggest fields, besides the growing field of distributed sensing, is Bragg Grating POF sensing around which the majority of this thesis is centred. One of the problems facing POF sensors, especially single mode fibre based ones, is its compatibility with present day systems. So far it is almost always necessary to connect POF fibre to a silica fibre, to lower relatively high losses of POF, or to connect to a single mode coupler or a pigtailed source which are available only with silica fibre.

1.5.2. Microstructured optical fibre sensors

The Microstructured fibres, as previously mentioned, have the possibility to tailor light guiding properties inside them. In particular, the ability to be endlessly single-moded to a broad range of wavelengths. This property is particularly important for high sensitivity of Bragg grating based sensors. The other important benefit of microstructured fibres is the accessibility to evanescent field [82] in the microstructure, which can be used for various chemical, humidity and pressure sensing. Furthermore, many sensors have been made which are based on plasmonic resonances [83], fluorescence [84] or birefringence [85]. mPOF based sensors have been reported for analysis of aqueous solutions [86,87], gas detection [88,89], aqueous solutions analysis, Raman spectroscopy [90,91], biosensing [28,56,77,84], determining the acidity (pH) [92], hydrostatic pressure and temperature measurements [24,85].

1.5.3. Fibre Bragg grating based sensors

Bragg sensing is in principle a localised sensing, meaning that the measurement is done in a small region of a grating. That does not mean that the measurement acquisition system needs to be necessarily near the measurand, one of the bigger advantages of fibre sensors is that acquisition system can lay quite far away from the measurement scene. The sensing is done over a Bragg grating region, which is usually no more than 1-2 cm long. The sensing is based on detecting the shift of the Bragg grating peak. The shift happens due to change of the grating structure, which could be due to physical change (e.g. elongation of the fibre) or due to radiation induced change in the refractive index. For that reason, the FBGs find use in environmental and mechanical parameter measurements. The shift can be detected in transmission and reflection, where the latter one is especially convenient as it does not require both sides of the fibre to be connected to the system – one side of the fibre acts as the input and the output. In comparison to other types of sensors, FBGs are small and compact, practically insensitive to EM radiation and electrical power fluctuations, and importantly - they are relatively cheap. Sensors based on FBGs have been demonstrated for temperature, humidity, strain, acceleration, vibration, chemical, electro-magnetic fields detection [12,73,93,94] and infrared radiation detection [95].

FBGs also have the possibility of multiplexing. This important advantage gives rise to the embedded sensor grids also known as “Smart structures”. Multiplexing several FBGs and embedding them in certain materials, for example airplane wings, produces a grid of sensors which give detailed information of the structural behaviour and health of the host material. The structures under examination can be various so the smart structures are used in buildings, roads, dams, bridges, wind turbines, airplanes, etc. The real time monitoring of smart structures helps improve the safety of the structures by allowing timely repairs, noticing excessive wear and preventing unwanted damages [73]. In addition to structural engineering, multiplexed sensors forming a grid can also be used for biomedical purposes, in particular so-called bio-textiles have emerged as an important application [71].

One of the downsides related to Fibre Bragg Grating based sensors is its interrogation system. Production of FBGs is a relatively cheap procedure with the present-day mass

production, but the interrogation systems can be very costly and complex. The common way of interrogating fibres is by using a broadband light source and a wavelength interrogation system. The cross-sensitivity is a common problem with FBG based sensors: the FBG peak wavelength will shift under stress but also under the temperature. This is particularly challenging for high sensitivity applications. To remove the influence of temperature, one of the ways is to have additional fibre with FBG which is completely unstrained. Upon temperature calibration of the two FBGs one can eliminate the wavelength peak shift induced by the temperature [96]. However, this procedure requires another fibre with FBG which makes the whole system more complex.

FBGs in microstructured fibres have some additional advantages for sensing as their basic properties are the same as in all-solid fibres, but also having the possibility of specifically tailored dispersion. Microstructured fibre based FBGs also have access to the optical mode through the holey cladding, which allows for their use in liquid and gas detection, as well as determination of composition [12,37].

1.5.4. POFBG Based Sensors

Polymer fibre Bragg Grating based sensors essentially cover all the sensing range of applications that their silica counterparts can do. They have their down sides and limitations due to their higher sensitivity to temperature, humidity, and their higher loss. But for many applications big distances are not an issue as sensing is done in ranges where loss doesn't have much of an impact on the systems. When POFs are used as strain sensors, especially on higher strains, FBG response might experience hysteresis to increasing and decreasing strain as shown in Figure 1-11. After bigger strain is applied it takes up to several days for the sensor to relax back to its original state. This does not present a big issue as vast majority of fibre sensors are commonly embedded in host material which reduce the effects of fibre relaxation hysteresis (Figure 1-12). Sensors have been reported for temperature and humidity, for strain and bend detection [97–99]. The real benefit of polymer sensors is visible in applications requiring its low Young's modulus such as in Plastic fibre bio-textiles [100,101]. Sensors for breathing of the patient, monitoring of a heartbeat and others have been investigated. In these applications,

it would be hard and sometimes impossible to implement the similar sensor with silica as stiffness of silica would stiffen the structure itself [102].

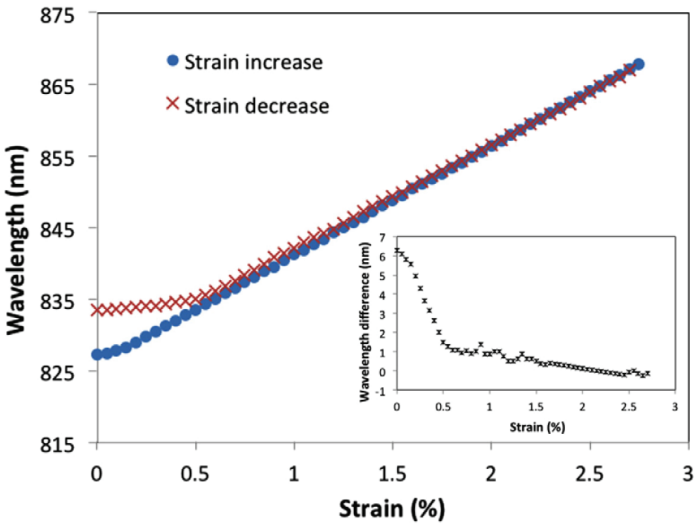

Figure 1-11. FBG wavelength peak versus strain, for the POFBG sensor in PMMA fibre. The sensor was strained between the fixed and movable stage, and was held at each point for 30 s. Inset shows the wavelength difference between readings taken between increasing and decreasing the strain (image taken from of Abang *et al.* [103])

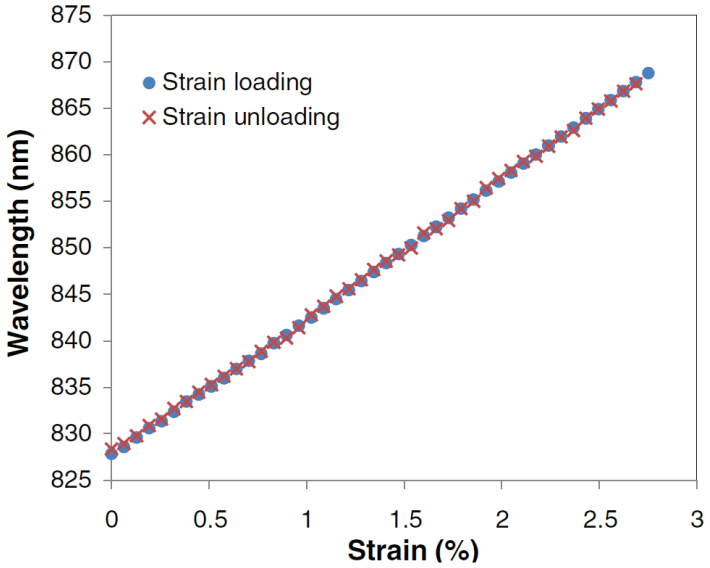

Figure 1-12. Straining and relaxing of a fibre containing an FBG glued to the thicker plastic substrate. When fibre sensors are embedded, the hysteresis of sensors is reduced to great extent (image taken from Abang *et al.* [103])

With respect to strain sensitivity values range from 1.15 to 1.5 pm/με, with majority of the results being in 1.3-1.4 pm/με, for gratings in 1550 nm range [14]. The strain sensitivity of silica FBG in the same region is about 1.2 pm/με.

With small temperature ranges ensuring linear response for POF FBG, the Bragg wavelength shift is given by [104]:

$$\Delta\lambda_B = \lambda_B(\alpha + \xi)\Delta T \qquad (5)$$

That relation is valid in the absence of cross-sensitivity, with $\Delta\lambda_B$ being the Bragg wavelength shift, λ_B is the Bragg wavelength, α is the thermal expansion coefficient, ξ is the thermo-optic coefficient and ΔT is the temperature change. α and ξ are both positive coefficients for silica, ensuring a positive wavelength shift. For polymers, ξ is negative, in which case wavelength shift is dependent on whichever coefficient is bigger. Normally ξ dominates.

This sensitivity depends on the humidity in the environment of the fibre with values ranging from dry $-10°pm\ C^{-1}$ to about $-36°pm\ C^{-1}$ in water [14]. PMMA has the affinity for water,

it absorbs it which makes fibre swell and refractive index to rise, leading to a positive shift in the Bragg wavelength. This dependence is linked to temperature, but in case of no temperature change, the wavelength shift induced would be

$$\Delta\lambda_B = \lambda_B(\eta + \beta)\Delta H \quad (6)$$

With η being the normalized dependence of refractive index on humidity, and β being the swelling coefficient dependent on volumetric change $(\%\ RH)^{-1}$ induced by humidity. For POFs to react on humidity takes about few tens of minutes, which is strongly related to the thickness of the fibre.

1.5.5. Microstructured POFBG Sensors

With respect to microstructured polymer optical fibre Bragg based sensors, their applications are essentially the same as for their silica counterparts. The advantages of the microstructure, such as single mode guidance, are still not exploited to its fullest given that the ability to write gratings in fibres is still new. Some investigated and employed applications are temperature [105] and humidity sensitivity [106], hydrostatic pressure [107], and biochemical concentration sensor [108].

1.5.6. Microstructured Long Period Grating based Sensors

LPG sensors benefit from the possibility of tailoring the dispersion in Microstructured fibres, to which sensitivity is strongly related [91]. In addition to the possibility of having the holes filled with gas or liquid which influences the propagating mode of the fibre, long period grating sensors are sensitive to the surrounding medium. This allows them to sense water content or gases from the surrounding medium more easily [64,109], in addition to humidity, temperature and bending [58]. In-series concatenated LPGs have also been used for sensing purposes. The pair of identical LPGs is made some centimetres apart where the first LPG couples the core to cladding mode and the second one gets the cladding mode back to the core mode. Due to the phase shift, the light coupled to the core by the second LPG is giving rise to the interference pattern. In-series LPGs have been used to sense external index of refraction, temperature, transverse load and bending [110]. Long period gratings have been made both in silica and polymer fibres [59,62,67].

Chapter

2 Fibre Bragg Grating Inscription

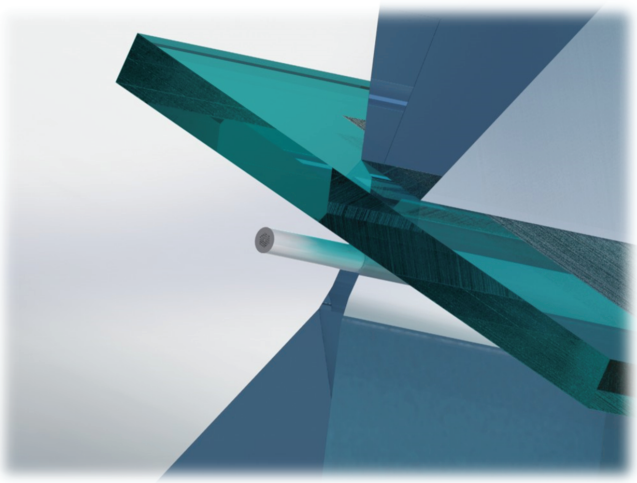

This Chapter along with majority of its graphs, tables and images is based on the following publication: "Bragg grating writing in PMMA microstructured polymer optical fibres in less than 7 minutes" [36].

Fabrication of Bragg gratings in mPOFs, with the phase mask technique, is a time-consuming process. In mPOFs exposure times from 60 to 270 minutes have been reported [45,111,112], for up to 10 mm long gratings, while for the step index fibres times are shorter and typically amount to tens of minutes [14,45,111,113]. The writing time can be reduced by doping the fibre [14,104] but doped fibres are more difficult to fabricate, the transmission loss increases and they are less suitable for in-vivo biosensing. In this work we

demonstrate the fast fabrication of FBGs using the phase mask technique in mPOFs, having reflection peak strengths of up to 26 dBs and being written in less than 7 minutes. Short writing time is important for grating stability and is an important step towards (commercial) on-draw tower writing of FBG in mPOFs. The fabricated gratings have a reflection peak at 632.6 nm on average and are written into a 3-ring PMMA single mode mPOF fabricated at DTU Fotonik.

2.1. Fibre Preparation and Cleaving

To make a Fibre Bragg Grating in our setup, fibre piece of no less than 3 cm had to be cleaved on both ends. Cleaving of a fibre is a controlled break (cut) with intention of making a flat end face. The end-face has to be flat, perpendicular to the longitudinal axis of the fibre. It is important for any application requiring splicing or connecting a fibre to other optical components, or for free space coupling of the light into the fibre. Cleaving of polymer fibres is a not as easy and straightforward procedure as it is with silica fibres. With silica fibres all it takes is to make a small cut with the cleaving scribe (cleaving tile or other similar type of cleaver), and by applying tensile force on the fibre - the fibre will cleave.

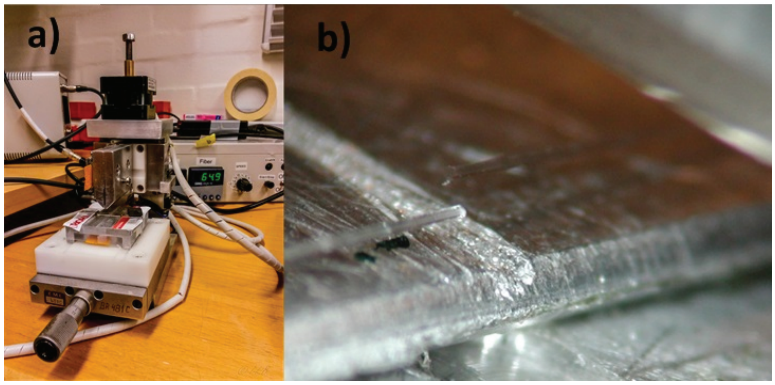

Figure 2-1. (a) Photo of an automatized fibre cleaver used for experiments, (b) image of the fibre holder with groove, cleaved fibre and a blade standing above it. Deep groove, inadequate temperature and blunt blade are the main reasons for bad cleave.

Polymer fibres, since they are made from much softer material and do not have crystalline structure, cannot cleave in that way but require a different method for cleaving. Several methods have been proposed such as UV-laser cutting, focused Ion-beam milling and hot blade

cleaving [17,31]. The first two are impractical and expensive for widespread usage, especially on the field. The latter is the most common method which was employed also at our institute.

An electronic fibre cleaver was made at our institute by Stefani *et al.* [31] and was used for efficient cleaving of the fibres. The cleaver used is shown in Figure 2-1.

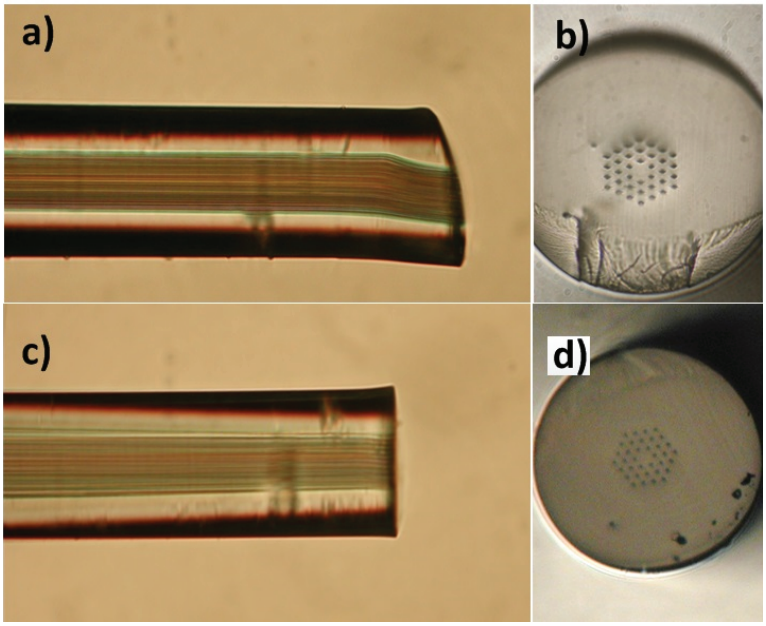

Figure 2-2. Images of good and bad cleave. A bad cleave, shown in side-view (a) and end facet (b), is characterised by bending of the holey structure, squeezing of holes, as well as cracks on the facet due to inadequate temperature, blunt blade and deep groove (see Figure 2-1). A good cleave shown in (c) and (d) shows no traces of bending, or cracks on the end facet.

For optimal results, we used thinnest blades being only 200 μm thick, cutting with the speed of 5.6 mm/s, with the blade and the bottom plate being heated to around 70°C. Initially we used the bottom plate with a grove so the blade does not hit the bottom once it cuts through the fibre, which would ensure longer lifetime of blades. However, the grove in the bottom plate makes fibres bend upon pressure of the blade, which causes a slight deformation in the fibre structure just before the cleaved facet as shown in Figure 2-2 b). This bend makes it hard to couple the light to the core of the fibre, even-more so for microstructured fibres whose holey structure is deformed and sometimes holes squeeze or entirely close.

2.2. FBG inscription setup

The technique we use for inscribing FBGs is the most commonly used phase mask writing technique. A 30 mW HeCd CW laser (IK5751I-G from Kimmon) operating at 325 nm is used for grating inscription. The laser light with a circular Gaussian beam profile and a diameter of approximately 3 mm, was directed through a series of 4 mirrors arriving at the focusing lens. The focusing lens is a plano-convex cylindrical lens (LJ4862-UV from Thorlabs) with a focal length of 25 mm, however the operational back-focal length was found to be 18.65 mm at 325 nm. The lens is focusing the beam through the phase mask down on to the fibre, which was lying about 100 µm below the phase mask. The focal spot diameter was calculated to be about 4 µm. The phase mask has a size of 30 mm x 25 mm x 2 mm, a uniform pitch of 424.84 nm and was custom made by Ibsen Photonics, claiming less than 15% transmission in the 0^{th} order, for writing of 650 nm FBGs using 325 nm laser light.

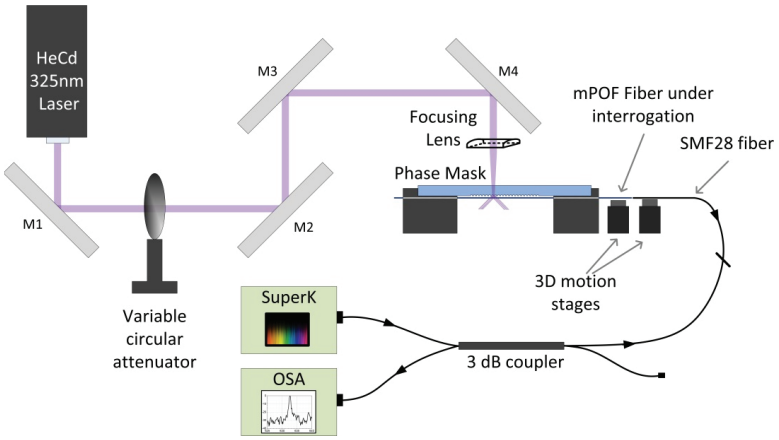

Figure 2-3. Sketch of a writing and interrogation setup. The light was directed from the He-Cd laser

A sketch of the setup and the image of it can be seen in Figure 2-3. and Figure 2-4. respectively.

2.3. FBG The Setup Alignment

The alignment of the setup is crucial for optimal inscription of the fibre. There are five degrees of alignment which have to be taken into account.

1) ***(Focusing Lens - Phase Mask – Fibre) Orientation alignment***

   The corrugated surface of the phase mask should be perpendicularly aligned to the fibre direction. Focusing of the plano-convex lens should be together in the same plane with the phase mask and the fibre.

2) ***Focal distance from the plano-convex lens (through the phase mask) to the fibre:***

   It ensures the maximum delivery of the laser power to the core of the fibre, where the grating should form.

3) ***Space between the phase mask and the fibre***

   This spacing should be as little as possible ensuring the longest inscription region of the grating. Inscription region is formed by the overlap of diffraction modes in the core of the fibre. For the inscription with the scanning laser beam, this plays a less significant role as even with the minimum overlap of the diffraction modes the grating will be made. However if the fibre is put too far below the phase mask, there will be no overlap between the diffraction orders so grating will not be formed. In our setup, a 150 μm in diameter fibre was standing about 150 μm bellow the phase mask.

4) ***Inclination of the plano-convex lens and the phase mask to the fibre***

   Plano-convex lens and phase mask have to be aligned one with another with two coordinate axes to the fibre bellow it, as described under point 1 above. In addition to that, the lens, phase mask and fibre have to be in three parallel planes, one over another.

5) ***Orientation of the microstructured fibre:***

   For inscription of microstructured fibre, orientation of the holey structure to the incoming light makes a big difference with respect to final results. This will be thoroughly examined in the following Chapter.

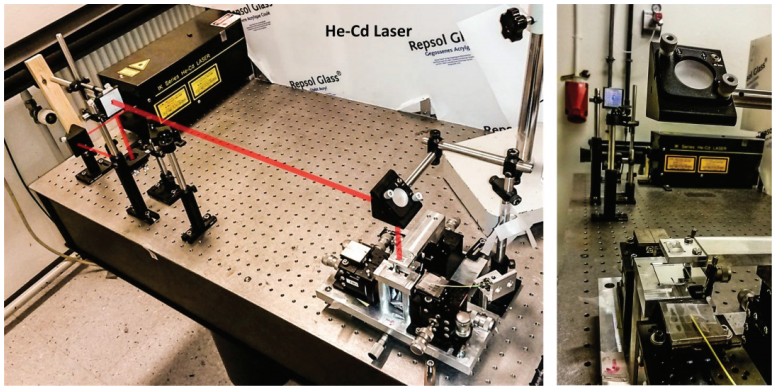

Figure 2-4. Images of the inscription setup. In the left image, the red line shows the trajectory of the laser beam; it starts at He-Cd laser, it passes through series of 4 mirrors and it ends up on inscription stage. In the right image the inscription stage is in the foreground together with the lens which is used for focusing the light, through the phase mask the fibre.

The inscription setup was made with the phase mask holder along with the grooves for fibre, ensuring partial alignment for the cases (degrees of alignment) no. 1 and 3. To align the setup for the cases 1, 2 and 4, we used a pinhole paper on the mirror M3, as visible in the background of the right image in the Figure 2-4. In order to find the optimal distance between the lens and the fibre, as in the case no. 2, and knowing that fibre grooves ensure that the fibre lies about 150 μm bellow the phase mask, we first had to align the plano-convex lens to the phase mask. A slide of fused silica glass with the same dimensions as the phase mask was obtained from Ibsen Photonics. The silica glass was used to create a mirror; approximately 25 nm thick layer of Aluminium was deposited on one side of silica glass using e-beam deposition. The mirror was used to focus the beam precisely at the bottom of the silica glass, which was visible in the back-reflection by matching the original and reflected beams on a pinhole paper attached to one of the mirrors as shown in Figure 2-5. After removing the silica glass mirror and placing the phase mask back in the holder, the focus was shifted for about additional 175 μm further down, which is the optical distance between the phase mask and the core of the fibre that was used. Additional method used to confirm the crude alignment was inscription of a grating in a dummy bulk fibre as shown in section 3.1 of the next Chapter. The fibre was inscribed for 30 minutes after which it was cleaved at the point of inscription so the burnt cross-section can be assessed. Subsequently, the fibre was repositioned and the same procedure was done until the cross-section showed the narrowest inscription mark.

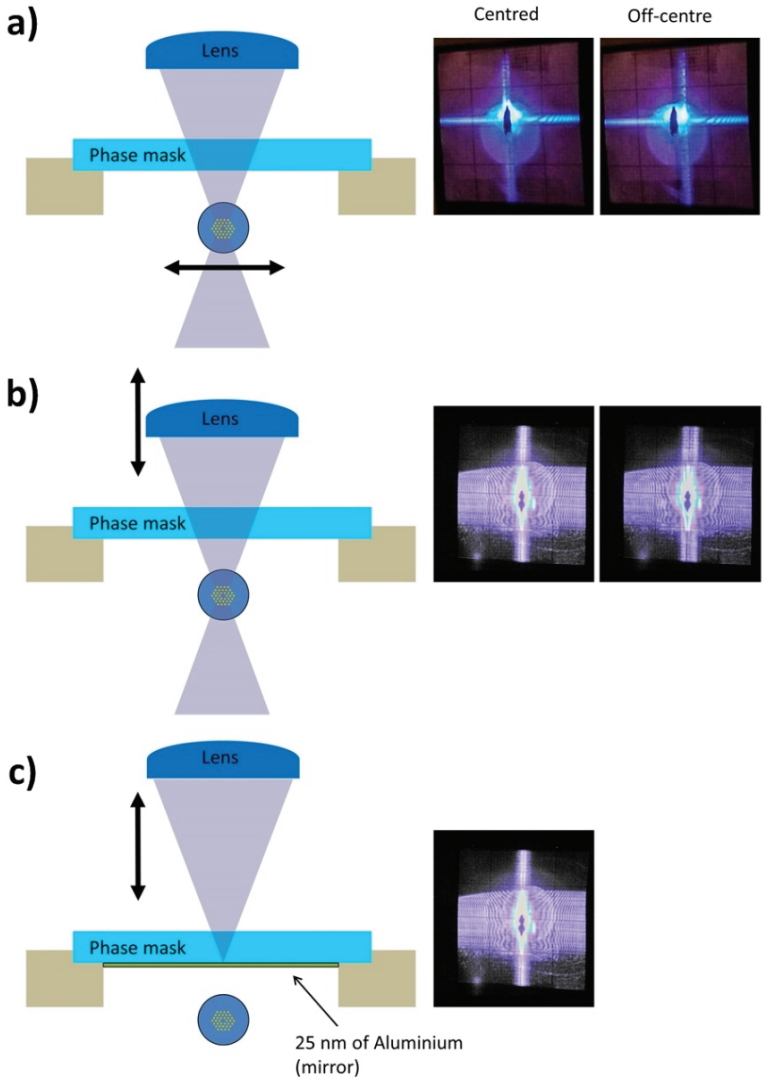

Figure 2-5. Alignment of the fibre with respect to the plano-cylindrical lens. The pinhole paper on the mirror M3 (inset images) can help to easily adjust the position between the lens and the fibre as shown in (a), but for the vertical alignment to the microstructured fibre the light reflects over multiple semi-reflecting surfaces back to the pinhole paper so it is unsure what the focus is on (b). With a mirror made of fused silica glass, we can easily focus to the bottom of the phase mask. Knowing that the fibre core should be about 175 µm bellow it is only necessary to do the fine tuning, which is done while inscribing.

In comparison with step-index fibres, mPOFs are suffering from long writing time due to their microstructured configuration, which scatters the light from the UV laser [47]. Due to this

added scattering, it is necessary that the focus of the writing beam is well aligned with the core of the fibre.

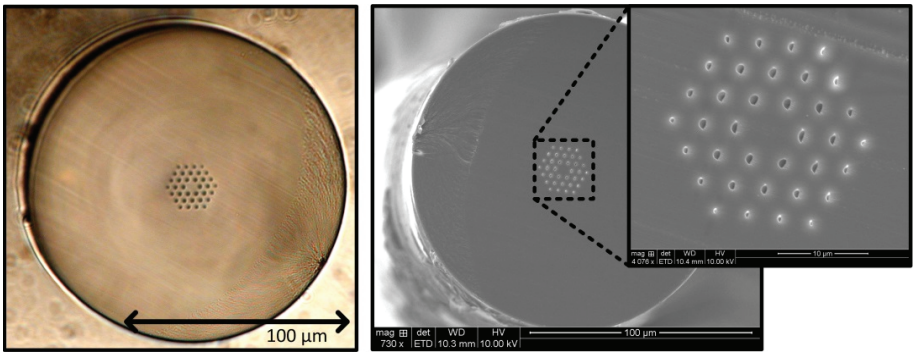

Figure 2-6. Microscope image and Scanning Electron Microscope (SEM) image of the fibre facet.

The fibre used in the experiment presented in the following is an mPOF, fabricated in-house at DTU Fotonik using a polymer draw tower. Commercially available 7 cm PMMA rods were obtained from Nordisk Plast A/S. The rods were machined down to a length of 10 cm and a diameter of 6 cm. The desired 3-ring hole structure was drilled into the preform. The preform was drawn down to canes with a diameter of approximately 5-6 mm. The canes were subsequently sleeved (stacked up inside extra tubes in order to increase their diameter) then drawn again, this time down to a fibre with a diameter of approximately 125 micron. A microscope image and Scanning Electron Microscope image of the resulting end facet is given in Figure 2-6 which shows the cleave made by a fibre cleaver fabricated in-house [31] at 65° C temperatures of both blade and fibre holder. The final optical fibre has a hole size of 1 µm and the pitch (the hole to hole distance) of 3.75 µm. The hole to pitch ratio is 0.26 ensuring that the fibre is endlessly single mode [114]. The fibre has a propagation loss of around 10 dB/m at 630 nm (see Figure 2-7). Note that the holes in the microscope image appear larger due to the diffraction limitations of the optical microscope.

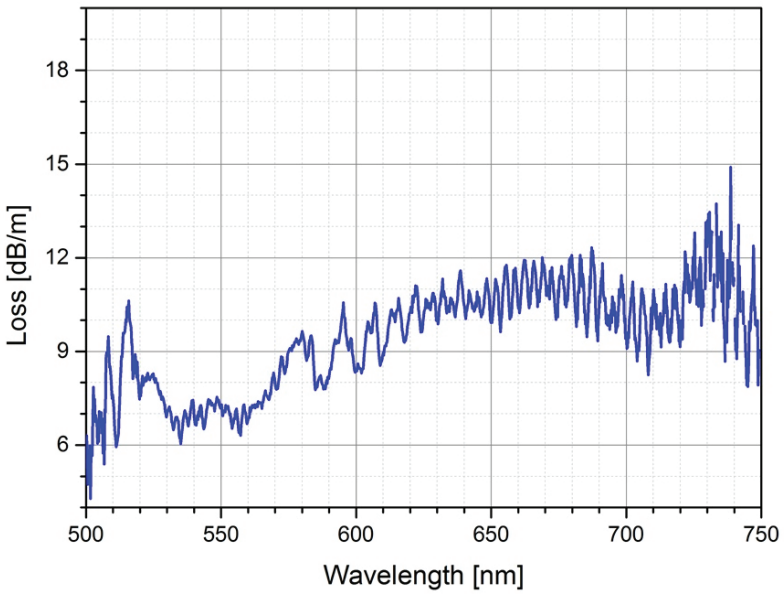

Figure 2-7. Transmission loss of 3-ring PMMA fibre used in experiments.

A SuperK white light source from NKT Photonics A/S was used to interrogate the mPOF. The output fibre was connected to a 650 nm 3dB coupler and, via a connected SMF28 fibre, the light was launched into the mPOF. Index matching oil was put in the space between the SMF28 and the interrogated mPOF to reduce reflections and thereby minimize the noise. The light reflected from the FBG was coupled back through the 3dB coupler and finally to the optical spectrometer (Ocean Optics HR2000) or Optical Spectrum Analyzer (OSA, Ando AQ6315A). For fast monitoring of the FBG growth dynamics the optical spectrometer was used, while for accurate spectrum recording, the OSA was used.

2.4. Bragg Grating Inscription and results

To monitor the grating inscription, i.e. to track and record the peak growth, a LabView controlling software routine for the Ocean Optics Spectrometer was developed. As the spectrometer has a linear scale and a 12-bit analog to digital converter, the integration time had to be changed each time the signal was approaching the limit of 4096 counts. This means that in the output data, a proper scaling was made by scaling the different integration time slices to obtain a smooth curve. The resulting curves are presented in Figure 2-8.

Last section of most of the curves seem noisy, as does the first section of the curve growth. This is due to the repositioning of the SMF28 fibre with respect to the mPOF. Repositioning had to be made in order to optimize the core coupling. At the beginning, as soon as the reflection peak was spotted, an optimization alignment was made. An additional realignment was made just after the laser writing was stopped in order to find the strongest peak reflection.

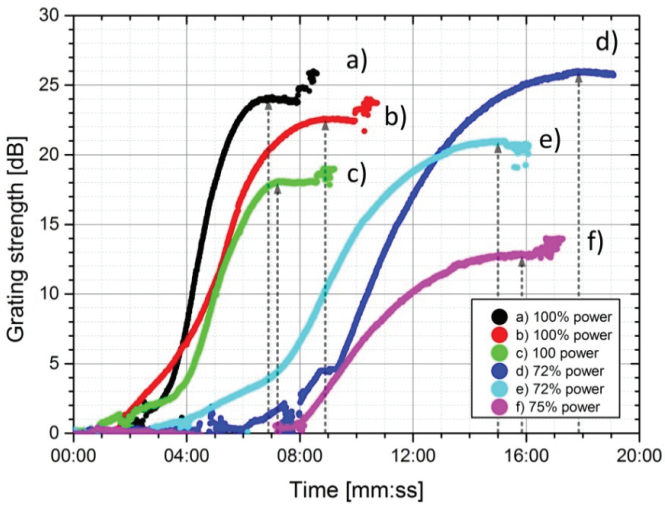

Figure 2-8. Curves showing growth of the Bragg reflection with respect to time. FBGs a, b and c are written at full laser power while FBGs d, e and f are written at lower power. Arrows are showing the highest peak of the saturation region.

As the dynamic range of the Ocean Optics spectrometer is low, the final spectrum was taken with the Ando AQ6315A (OSA), in order to obtain a correct noise floor and peak strength.

Since the relative growth observed with the Ocean Optics spectrometer was correct, the corresponding growth curves were scaled in whole to the final spectrum obtained by the OSA, the corresponding final spectra are shown in Figure 2-9.

In Figure 2-8, six grating growth curves are presented. Curves a, b, and c represent 3 fibres which had Bragg gratings written with maximum power from the laser, while the fibres d, e and f had gratings written with a circular attenuator inserted in the beam path, attenuating the laser light to approximately 72% of the initial power. In Figure 2-9 the final reflection spectra are given normalized to 0 dB at the highest peak for easier comparison. All the gratings have a reflection peak centred at 632.6 nm. With our setup, we were able to inscribe Bragg gratings in 125 µm PMMA fibres consistently in less than 10 minutes. The fastest writing time, the time between opening the shutter of the laser and reaching the saturation region (shown with arrows in the Figure 2-8), is around 6 minutes and 50 secs, with a grating reflection strength of 26 dB (fibre a).

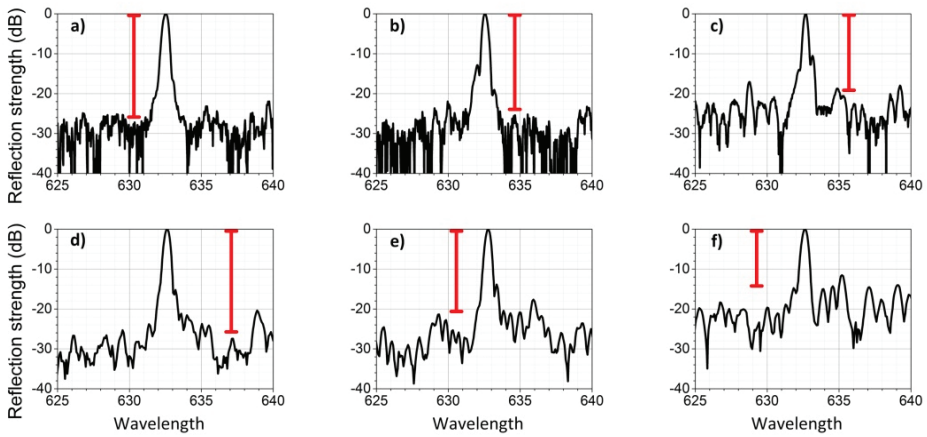

Figure 2-9. Bandwidths of fibres written at full laser power (100% power, *a*, *b* and *c*) and fibres written at lower laser power (72% power, *d* and *e*, 75% power *f*), presented in Figure 2-8.

While there does not seem to be a correlation between the grating reflection strength and the power, there is a strong dependence on power for the writing times and the rate of grating growth.

Table 2. Comparison of growth rates and final quality of the reflection peaks for the 6 fibres investigated in Figure 2-8.

	Growth Rate (10-90%)	Saturation Time (mm:ss)	FWHM	Grating strength
a)	7.9 dB/min	06:50	0.4 nm	26 dB
b)	3.99 dB/min	08:50	0.35 nm	24 dB
c)	3.7 dB/min	07:10	0.3 nm	19 dB
d)	3.18 dB/min	17:50	0.4 nm	26 dB
e)	2.47 dB/min	15:00	0.4 nm	21 dB
f)	2.1 dB/min	15:50	0.425 nm	15 dB

Regarding the quality of grating reflections, the results are summarized in Table 2. The fibre a has a clean noise floor, which is attributed to shorter exposure after the saturation region was reached. For some fibres, not presented here, a clear connection was observed between the writing time after the saturation was reached and the quality of the final reflection peak. Although the writing time is shortened because of the increased laser intensity, the gratings are not significantly stronger. Grating peaks are observed with various strengths: similar final spectra of around 20 dB are obtained by other research groups or by our group with different setup [30,31,45,113,115,116]. From the outside, the fibres which have strong gratings inscribed in them can be visually recognised as they scatter the white light from the core in different directions, as shown in Figure 2-10. The fibres which have weak or no grating in them have a shiny mark to burn of the UV laser at the position where the grating should be. This mark uniformly scatters all the colours in all directions,

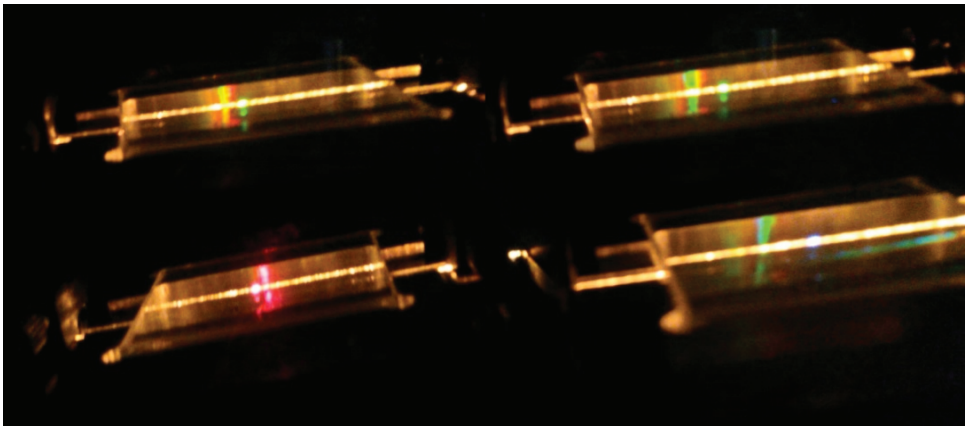

Figure 2-10. The FBG scattering of the white light at different direction. Presented are 4 images taken at different positions capturing different colours that the good FBG scatters. Due to this wavelength's selective directional scattering, it is possible to visually inspect fibres with good and bad quality gratings.

Additionally, it was observed that with lower writing power, the threshold (the time when the grating peak is firstly observed) is shifted as well. That implies that some internal processes might be taking place in the fibre before the grating inscription actually starts. In each curve, it is noticeable that once the peak appears, the growth rate increases rapidly, especially in that initial period. Later on, at around half of the maximum reflectivity, the growth rate begins to slow down. As the grating approaches saturation the growth rate rapidly decreases.

In Figure 2-11 it is more clearly visible that grating formation is possibly occurring in 3 stages. The first stage is "invisible" formation which we could name r_0, as reflectivity doesn't grow. The change of the refractive index induced by a laser light through phase mask is too small then for our instrumentation to detect, the reflected peak is below the noise floor of the system. The growth stage of grating is happening in second (r_1) and third (r_2) stage, where second stage takes smaller amount and is characterised by slow growth of gratings reflectivity. The third stage r_2 is characterised by faster growth of grating reflectivity and it finishes with grating saturation, as the growth decreases to zero. The second (r_1) and third (r_2) growth stage are not always distinguishable but for the tracked grating formations, at more than half of them showed to have them both.

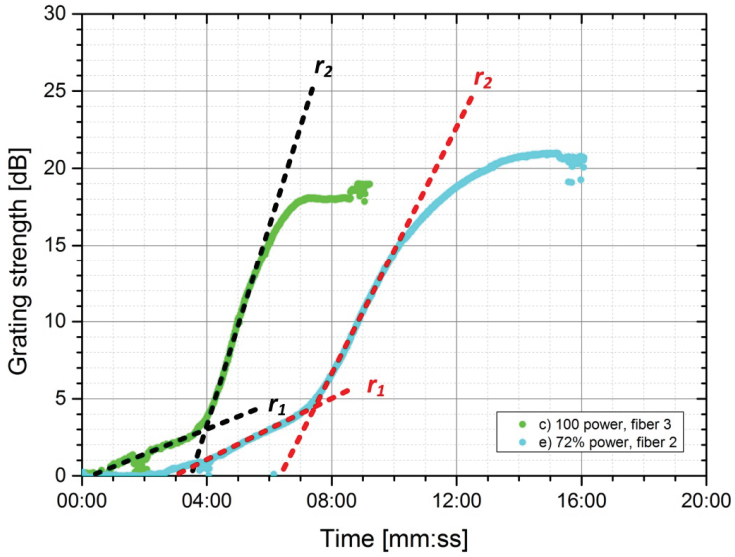

Figure 2-11. Formation of gratings. More than half of investigated gratings showed 2 different inscription rates, here named r_1 and r_2. This indicates that the grating forms in 3 stages, out of which sometimes only 2 are visible. Stage one would be "invisible" formation of gratings which we could label with r0, before a grating starts growing with a rate r_1 or even faster rate r_1.

There are three very important factors for the FBG inscription time, they are the intensity of the laser beam, careful alignment (discussed earlier in this Chapter) to the core of the fibre and orientation of the fibre (the importance of the latter one is discussed in the Chapter 3). In the FBG writing setup used earlier by our [18,29–31,45,111,117,118] and by other groups [52] there was an additional cylindrical lens (at the position of the circular attenuator), which was expanding the beam in order for the illuminated region on the fibre (FBG) to be longer. That lens has now been removed, which effectively increased the laser intensity in the now smaller, 2-3 mm long, illuminated region. To estimate quantitatively the change in intensity entering the fibre, the laser beam size just above the fibre was measured both with and without the first lens. With the first lens, the beam reaching the fibre was about 15 mm long (part of the beam was blocked by the second lens holder), while without that first lens it is now 3 mm long. Additionally, the attenuation of the first lens was measured to be about 0.8 dB. Taking both effects into account, the light entering the fibre is 7-8 times more intense after removing the first lens.

Soon after this study was conducted, the HeCd laser used for inscription of gratings was upgraded from 30 to 50 mW. After initial realignment the inscription quality seemed worse than recorded before, while at the same time fibres were left with a mark of a severe burn after not even 5 minutes of inscription. An optical attenuator had to be used to limit the power which ensured faster inscription of gratings. That prompted us to look further in inside-fibre factors limiting grating inscription which is presented in the following Chapter.

2.5. Summary

In the work presented in this Chapter, we demonstrated a significant reduction in fibre Bragg grating writing times in undoped fibre. With our grating writing setup, we were able to write a 26 dB grating in a single mode 3-ring PMMA mPOF in less than 7 minutes. The fastest writing time was 6 minutes and 50 seconds, which is about 10 times shorter than what was registered before for mPOF using UV phase mask technique. The FBGs which were made are centred at 632.6 nm and have a FWHM of 0.3-0.4 nm which, to our knowledge, is the lowest wavelength fundamental mode Bragg grating in mPOF. We have demonstrated a dependency between grating writing times and laser power showing that fast writing times require more intensity in the core. To our knowledge at the time, this was the fastest FBG writing time as well as strongest FBG reported in mPOF using UV phase mask technique. Nowadays, the shortest inscription times have been pushed down even more by some research groups, to durations of only several seconds [50].

Additionally, we suggest that that grating formation is possibly occurring in 3 stages. The first stage is "invisible" formation where reflectivity doesn't visibly increase. The growth stage of grating is happening in second (r_1) and third (r_2) stage, where second stage takes smaller amount and is characterised by slow growth of gratings reflectivity. The third stage r_2 is characterised by faster growth of grating reflectivity and it finishes with grating saturation, as the growth decreases to zero.

Chapter

Influence of the microstructure geometry on grating inscription

3

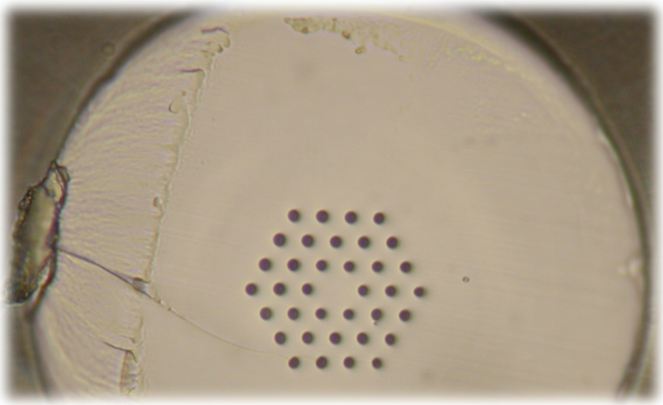

This Chapter along with majority of its graphs, tables and images is based on the following publication: "Angle dependent Fibre Bragg Grating inscription in microstructured polymer optical fibers" [48].

Single mode fibres are usually preferred for their accuracy. However, due to doping difficulties when producing single-mode step-index POFs, a lot of research is currently directed towards making microstructured POFs (mPOFs). These fibres are made from a single material having an air-hole microstructured area acting as a lower refractive index cladding and thereby a good control over the index difference enabling endlessly single-mode guidance. FBGs have been written in both step-index [119] and microstructured POFs [52], but the downside of mPOFs is that the air-holes are making it difficult to inscribe gratings as a considerable amount of the incoming inscription laser light is scattered.

In an effort to understand the influence of the microstructured region on the inscription beam, Marshall *et al.* [47] made computational model as well as experiments, where they measured fluorescence from side coupling of laser light to the core of the silica fibre.

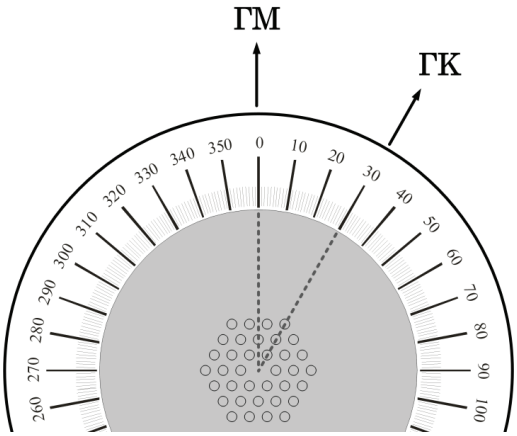

Figure 3-1. Microstructured fibre with marked symmetry directions ГМ and ГК

The results revealed that at certain angles around the angular direction labelled ГК (see Figure 3-1) the coupling to the core was the strongest. Another numerical study was made by T. Baghdasaryan *et al.* [120] focusing on propagation of femtosecond pulses in microstructured fibres, showing very similar results to that of Marshal *et al.* While both studies showed preference for certain angles, a practical study showing formation of the FBGs at different angles is still missing.

3.1. FBG burning

With the aim of further optimizing the setup, we fabricated a bulk PMMA fibre without a core. This fibre, since it didn't have a microstructured region or the core, would have the inscription UV-laser back-reflection having much less of scattering. That would allow for precision alignment of the FBG inscription setup which is not possible with other fibres. In addition to that, we exposed the fibre to longer inscription times, allowing the UV light to burn into the material. When the burn is looked under the microscope, it shows the precision of the focus as well as the intensity distribution of the light in the fibre. Both of which were beneficial to understanding of the grating formation (see Figure 3-2). These clear burns in the bulk fibre motivated us to explore the formation of the gratings in the microstructured fibre.

Figure 3-2. Images of a burned bulk dummy fibre, taken at different rotational position of the fibre. This fibre was around 150 μm in diameter thick, it was used for alignment purposes and irradiation duration determination. The grating used for making an FBG in our setup forms two orders +m and -m, these orders are clearly visible in this burned fibre

After the manufacturing of the mPOF there might be some residual stress in the polymer fibre, this stress is released when the fibre is heated [112]. In order to eliminate any issues arising due to the possible heating during the inscription process, fibres are usually annealed prior to inscription. However, the fibre used in this experiment is a non-annealed 3-ring PMMA fibre fabricated at DTU, which is endlessly single-mode having a hole to pitch ratio of 0.26 and a hole diameter of 1 μm. The outer diameter of the fibre is approximately 125 μm.

Before the inscription, each mPOF was angle-cleaved to avoid direct reflections back to the detector and was cleaned with alcohol using cleaning tissue. Cleaving was done with a fibre cleaver shown in Figure 2-1 in the Chapter 2, where the temperature of both blade and fibre holding plate was set to around 65°C.

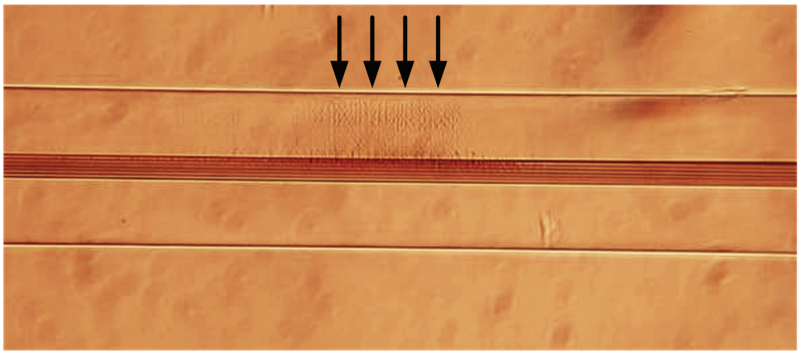

Figure 3-3. Fibre with a normal, non-destructive grating visible in the cladding area from above, after 15 minutes of 325 nm UV laser irradiation (arrows are showing the direction of inscription and grating position)

The FBG inscription was monitored with an Ocean Optics spectrometer and coupling was continuously optimized with a precision alignment stage so that the FBG reflection peak is observed in spectrum as soon as it forms. Each fibre was irradiated for a total of 30 minutes. The FBG spectrum was monitored in reflection as it grows, and when the growth stopped (observed the same way as shown in [36]), FBG inscription was stopped for a while so that a high-resolution spectrum could be taken using the OSA. In this first part of the inscription, which is usually finished within 15 min, the physical appearance of the fibre at the position of FBG was seemingly unchanged, but inscription fringes were visible under the microscope as is seen in Figure 3-3 and Figure 3-3.

The OSA was used to record the maximum FBG reflection in order to obtain a correct noise floor and peak strength. After the spectrum has been recorded by the OSA, inscription is continued until the total irradiation time was 30 minutes. At that point, the irradiated part of the fibre is burned enough to be clearly visible (see 3 examples in Figure 3-4) and the fibre would occasionally even stop guiding.

Figure 3-4. Fibre after 30 min of 325 nm UV laser FBG inscription on 3 different fibre sections

3.2. FBG burn statistics

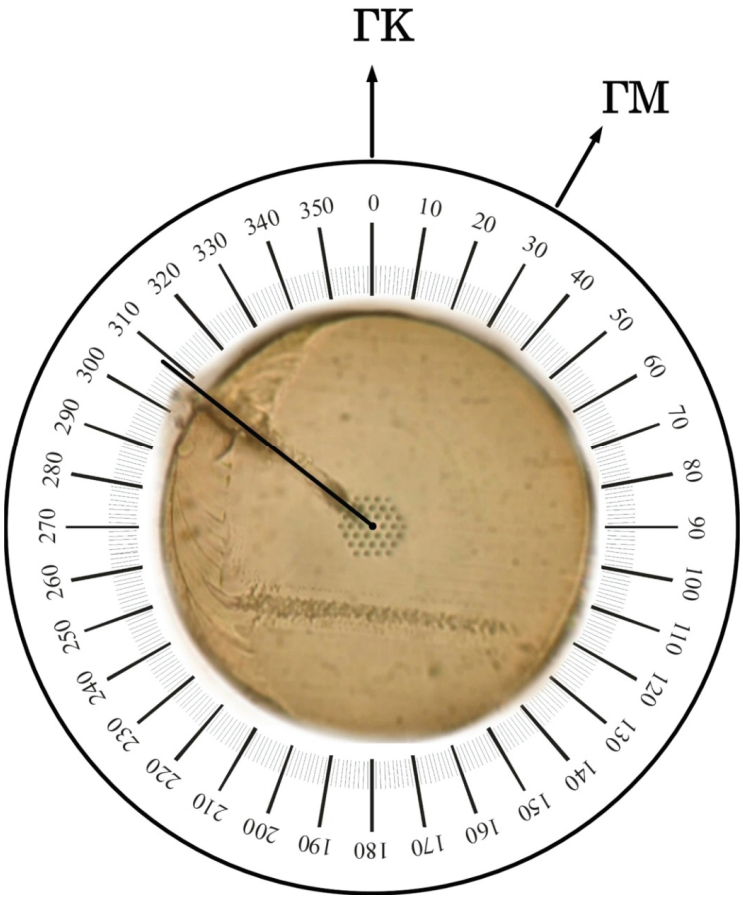

Figure 3-5. The cleave of the burned fibre; the burn was created after the grating was recorded in the mPOF fibre.

After burning, the fibre was removed from the inscription stage and a cleave was made at the position of the FBG. An image was taken of the fibre facet after cleaving and the direction of the burn (incident beam) was marked with respect to ГМ angles as shown in Figure 3-5. The same procedure was made with the subsequent fibres whose resulting images are presented in Figure 3-6. where the direction of the damaged section, caused by the incident beam, can be seen in relation to the microstructure. Each fibre has been oriented such that the inscription

mark is in the upper half of the fibre with one of the ΓM angles pointing up (see Figure 3-1). Correspondingly, all the inscription angles lie between the angles 270° (-90°) and 90°.

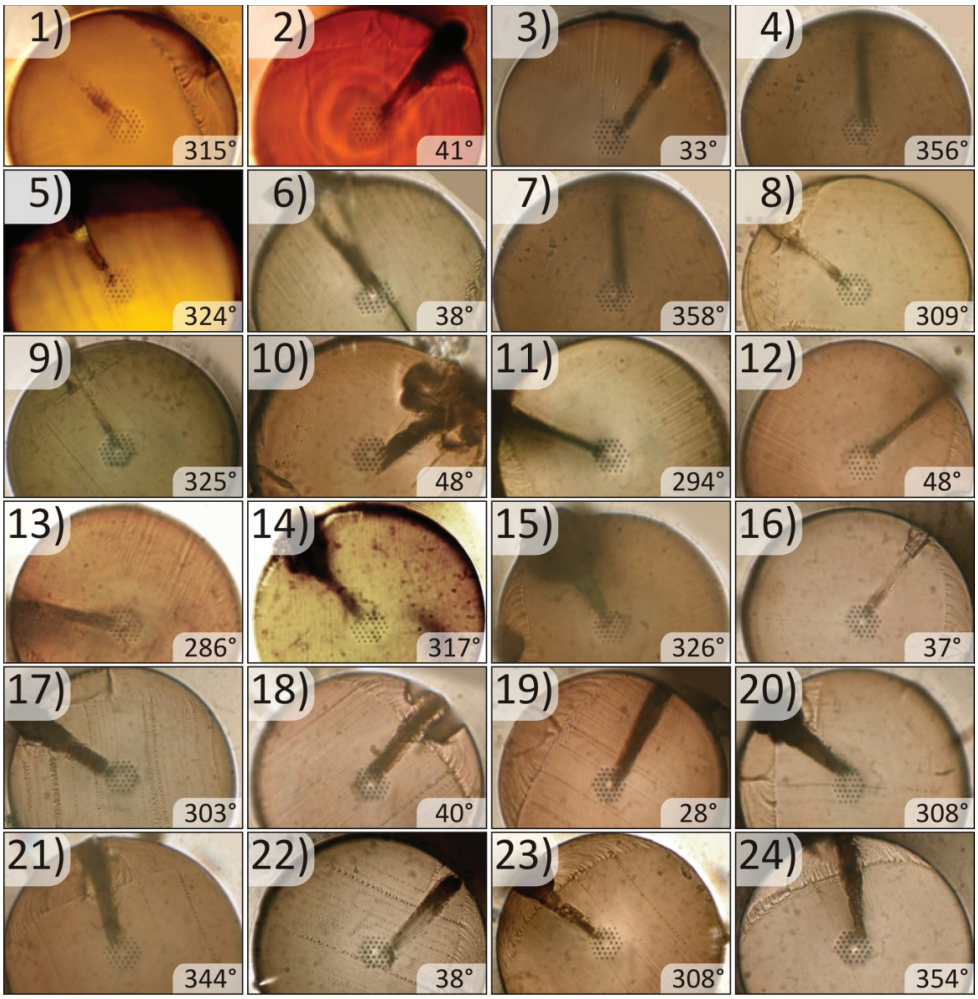

Figure 3-6. Fibres and their cross-sections revealing inscription directions when burned with the strong UV laser radiation

Moreover, due to dihedral (6-fold) and mirror symmetry of the microstructure area, we have mapped all the angles to the 0°-30° range in order to make the angle dependency more clear, as shown in Figure 3-7 and Figure 3-8. The green lines are FBGs having reflectivity between 12-20 dB, orange colour is used to map reflectivity of 1-6 dB, while red colour is used for fibres not having a visible grating after 30 minutes of inscription. The inscription angle

information is presented in the bottom right column of every inset image in the Figure 3-6 while consequent mappings with reflection strengths are visible in the tables presented below. In the tables we also presented the data regarding the FBG reflection strengths as well as inscription times. Tolerances of the obtained data are 1dB for reading the reflection strengths of the gratings, and 2° for the angles.

Table 3. Fibres with strong gratings (12-20 dB in reflection) after 30 min of FBG inscription. Some gratings have exhibited growths after the first apparent saturation, both times are recorded with the first saturation time in brackets. Fibre numbers refer to Figure 3-6.

Fibre number:	3	5	9	15	19
Original angle	33	324	325	326	28
First 30° angle	27	24	25	26	28
Offset [pitch]	¾ left	¾ right	½ left	0	½ left
FBG reflection	16 dB	16 dB	12 dB	18 dB	19 (7) dB
FBG saturation [min]	/	5.5	9	11	25 (12)

Table 4. a) Fibres with weak gratings (1-6 dB in reflection) after 30 min of FBG inscription. Some gratings have exhibited growths after the first apparent saturation, both times are recorded with the first saturation time in brackets. Fibre numbers refer to Figure 3-6.

Fibre No.	2	4	6	7	8	13
Original angle	41	356	322	358	309	286
First 30° angle	19	4	22	2	9	14
Offset [pitch]	1 left	½ left	1 left	½ left	0	0
FBG reflection strength	4 dB	4 dB	6(3) dB	2-3 dB	1-2 dB	5 dB
FBG saturation [min]	/	/	23(15) min	25 min	26 min	23(8) min

Table 4. b) Fibres with weak gratings (1-6 dB in reflection) after 30 min of FBG inscription. Fibre numbers refer to Figure 3-6.

Fibre No.	14	16	18	20 Off centre	21	23	24 Off centre
Original angle	317	37	40	308	344	308	354
First 30° angle	17	23	20	8	16	8	6
Offset [pitch]	½ left	½ right	1 right	1½ left	½ right	½ left	1 ½ left
FBG reflection strength	1-2 dB	3 dB	2 dB	3 dB	1-2 dB	3 dB	2 dB
FBG saturation [min]	20 min	25 min	23 min	15 min	19 min	20 min	20 min

Table 5. Fibres with no gratings after 30 min of FBG inscription. Fibre numbers refer to Figure 3-6.

Fibre No.	1	11	12	17	10 Off centre	22
Original angle	315°	294°	48°	303°	48°	45°
First 30° angle	15°	6°	12°	3°	12°	15°
Offset [pitch]	0	0	0	½ right	2 left	1 left

It can be seen from the information in tables, Figure 3-6 and Figure 3-7 that the best angles for the FBG inscription are between 24°-28° as the strongest gratings have been written in that angular region. Those are also the angles closest to ΓK, the angular direction that offers direct access to the core for the laser light.

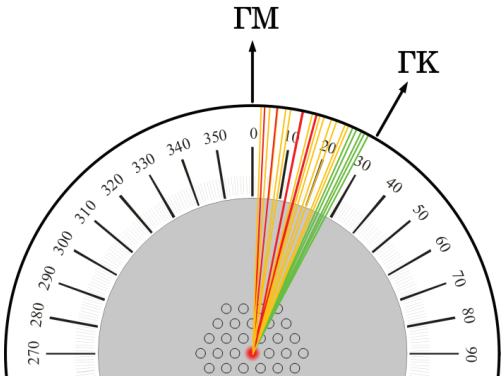

Figure 3-7. The microstructure area has a 6-fold symmetry in addition to the mirror symmetry of the unit segment which enabled mapping of the inscription angles to the first 30°. Green lines represent fibres having FBG reflectivity of 12-20 dB, orange 1-6 dB, and red represent fibres where no FBG formed in 30 min of inscription.

As the orientation of the fibre on the inscription stage was random, we were unable to obtain information on some angles. Angles 29°-30° were regrettably among those, meaning that we are unable to comment on the simulation results of Marshall *et al.* [47] regarding the decrease of the FBG quality at the ΓK angle. According to their simulation work, the best inscription angles are just around but not exactly at the ΓK angle, while this could not be confirmed with experiments.

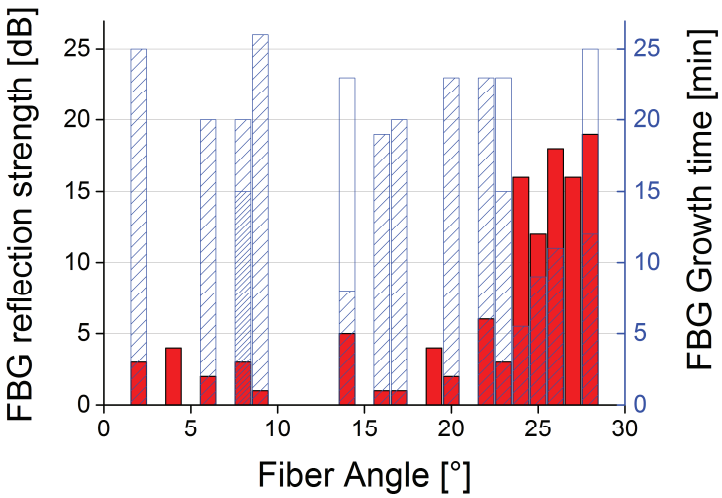

Figure 3-8. FBG final grating strengths (red full-colour bars) and their corresponding inscription times (blue patterned bars) shown on a bar chart for the mapped 30° angle. For the fibres where FBGs were not written or the inscription time was not recorded there are no blue bars. FBG 13 (14°), 6 (23°) and 19 (28°) experienced two saturations which are depicted with stripped and empty bars. FBGs 20 and 23 (both positioned at 8°) have same strength but their respective inscription times were different. Inscription times were not recorded for the FBGs 2 (19°) and 4 (4°).

In this Chapter we presented work where we have not dealt with inscription beam offsets due to limited amount of statistical information we could obtain. We assumed that the light completely or partially hitting the core is the light normally forming the grating.

The Fibres having weak gratings (represented by orange colour) seem to be evenly distributed over the rest of the angles suggesting that gratings can be obtained from all angles. Fibres without FBGs in them (red) are positioned less than 15° from ΓM, but without clear correlation to draw a conclusion why FBGs have not been formed. Some reasons could be insufficiently cleaned fibres, damage on the fibre surface and, the most probable one being, not enough inscription light reaching the core.

When looking at the speed of inscription, it is clear that the strong gratings (green angles) have been inscribed in short writing times, up to 11 minutes. Exceptions are fibre 3 and fibre 19. In fibre 3 (the grating inscribed at 27°) inscription was in the order of 5-10 minutes but the exact duration was not documented. Fibre 19 (the grating inscribed at 28°) exhibited interesting growth, the FBG reflection peak grew and saturated first to 7 dB in 12 minutes, following the

spectrum recording, with continued radiation the peak continued to grow slowly but gradually speeding up. In the final 2 minutes of rapid growth, the peak saturated at 19 dB after a total of 25 minutes. Certain other weak FBGs also exhibited similar growth after the apparent first saturation, where the spectrum was taken and inscription was continued. The saturations of those first growths are written in brackets besides the final saturation time in Table 3,Table 4 and Table 5. In Figure 3-8, both saturation times are presented for fibre number 19 with blue bars (empty and striped pattern). The saturation time in weak FBGs (orange angles, Table 4) was typically around 19-26 min.

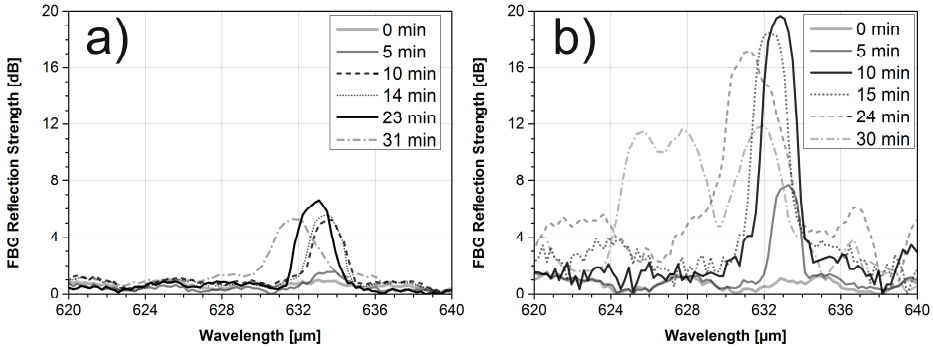

Figure 3-9. The FBG reflection spectra showing slower growth of the a) weak grating no. 13 and b) faster growth of the strong grating no. 15. The growth dynamic of the strong grating (b) shows destruction of the grating after about 30 minutes with the formation of the strong side-peaks while the main peak diminishes. The weak grating has not been destroyed after 30 minutes of irradiation as probably not enough light has entered the core to induce such a destructive change.

It should be noted that those weak FBG peaks were mostly not seen gradually growing but appeared first after longer exposure time, growing up fairly fast until saturation. The reason why good gratings had reflectivity of up to 20 dBs and not more could be due to misalignment of the inscription beam and a fibre.

One of the interesting formations of FBG can be seen in fibres no. 20 and 24 which had an offset of 1.5 times pitch and, from the images, it is visible that the beam was essentially not hitting the core. However, these two fibres managed to get gratings of 2-3 dBs which is about as strong as other (orange) FBGs. While we do not have enough data to confirm it, this could be due to scattering of the holes where the scattered light still managed to reach the core in sufficient amount to create an index change.

3.3. Summary

Starting from simulation and experiment by Marshall et al. in this Chapter we show a confirmation of their predictions that generally, also in the field of polymer microstructured fibres, the strongest gratings are formed around the certain angles named ΓK. The reason is clearly the direct access of the laser light to the core of the fibre. However, it has also been shown that gratings can be formed from practically any angle hitting the fibre. The condition is that there is enough intensity of the laser light, fibre has a clean surface and there is enough scattering by the holes towards the centre of the fibre, so scattered light reaches the core of the fibre.

To get a complete picture of the FBG formation with respect to the power, it would be necessary to repeat the procedure with higher light intensity and better focus. It has been also shown that gratings formed with the laser direction close to ΓK have much faster inscription time and therefore time of saturation. FBGs formed from angles further away from that angle typically start to form after 15 min of irradiation.

Chapter

4

Viscoelasticity of Polymer fibres after long-lasting strains

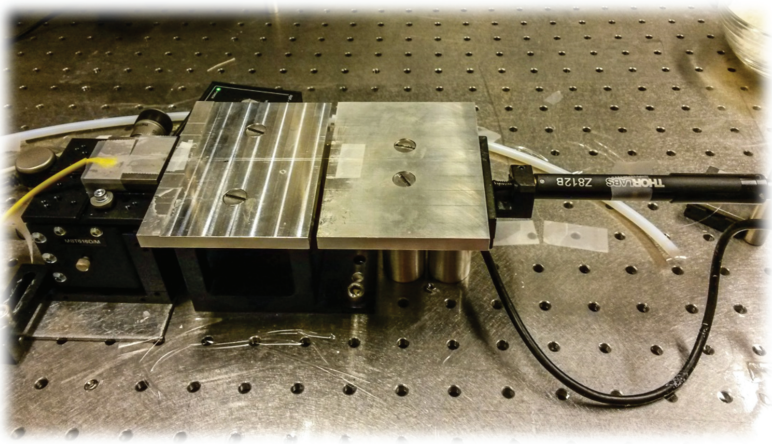

This Chapter along with majority of its graphs, tables and images is based on the publication in preparation titled: "Long-term strain response of polymer optical Fibre FBG sensor"

Unlike silica fibres, polymer fibres are still missing substantial information regarding their mechanical properties. In particular, due to their viscoelastic nature, polymers are experiencing nonlinear behaviour when strained and relaxed [18,46]. The strong viscoelasticity of polymers means that their mechanical properties can vary significantly depending on the duration and frequency of the applied stress [121]. Majority of instruments used to measure viscoelastic properties of materials are only capable of testing a limited range of loading frequencies so, although polymer viscoelasticity was broadly studied for bulk materials, polymer fibres viscoelastic behaviour is still expected to hold somewhat unique properties due to the elongated shape and drawing conditions.

In certain applications such as geogrids, smart textiles, and endoscopic manometers, polymer based sensors would be experiencing different levels of strain for various durations of

time [72]. Fibre relaxation is of great interest for commercialization of plastic fibre sensors, in particular the limits of viscoelasticity under different amounts and durations of strain. The frequency regime of up to 10 kHz, which could be used for acoustic and vibration sensing, has already been investigated by Stefani *et al.* [117]. The quasi-static behaviour of UV-written polymer FBGs, under strain and then relaxed, was also recently investigated [46,118]. In this Chapter we show the study of the behaviour of polymer fibres in low-frequency regime (between high frequency [117] and quasi-static behaviour [46,118]), where the period of straining and relaxation takes place in time scales larger than 1 second.

4.1. The long-term strain setup

The fibre used for the investigation was similar to the ones presented in previous Chapters, fabricated in-house using a polymer fibre draw tower, and is made of Polymethyl methacrylate (PMMA). The fibre has a cladding with a hexagonal 3-ring photonic crystal structure, with a pitch (a hole-to-hole distance) of 3.75 μm and a hole-to-pitch ratio of 0.26, making it endlessly single-mode [122]. The fibre outer diameter was 130 μm. A silica fibre was used to launch light into the POF and collect the reflected response of the FBG. The PMMA POF was prepared by cleaving at an optimal temperature of around 77°C [31] of both the blade and POF to ensure optimal coupling to the silica fibre. The response was monitored using a supercontinuum light source (SuperK Power from NKT Photonics) and the light was analysed using an OceanOptics HR2000 spectrometer. The fibre had an initial length of 14 cm and was strained to a maximum of 0.9% to stay well clear of high strains that might induce material deformation [123].The FBG was inscribed into the fibre using the phase mask technique [36]. After annealing the fibre for 48h at 85ºC, the relaxed FBG peak wavelength was at 618.7 nm.

The fibre has been mounted between a fixed and a motorized linear translation stage, see Figure 4-1 (left). The motorized stage was used to apply the targeted strain for certain duration. In Figure 4-1 (right) the blue curve shows the movement of the motor, which takes less than half a second to apply the strain. The purple dotted curve shows the reflected signal from the FBG; on the upstroke it follows rapidly the movement of the motor, but on the downstroke it

has a time-lag in its response. This unwanted time-lag appears due to the viscoelastic nature of polymer, and is the subject of this investigation.

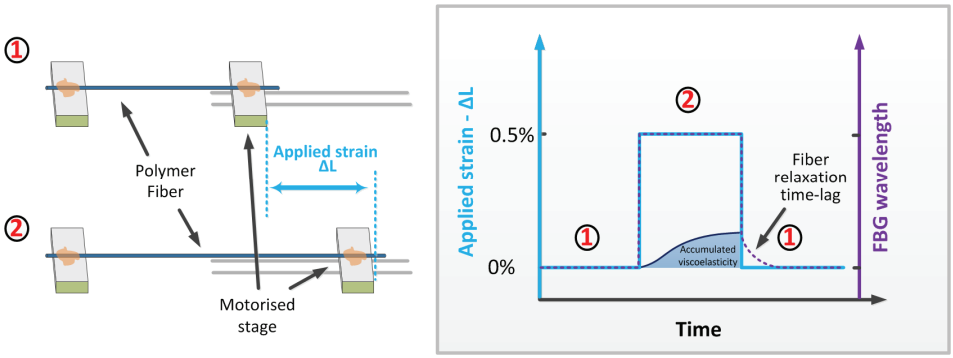

Figure 4-1. Experimental setup - the fibre has been strained with the help of a motorized stage (left). The fibre relaxation was monitored through the FBG peak monitoring. While the motorized stage moved consistently, due to its viscoelastic nature the fibre had a time lag in relaxing to the intial position (right).

The experiment was performed in an environment with a controlled temperature and humidity, where the change of temperature was less than 2°C and the humidity (RH) change was less than 2% in each sequence of experiment. This is important due to the temperature and humidity response of POFs [124].

4.1.1. Strain of 0.4%

The fibre was initially stretched by 0.7 mm, which corresponds to 0.4% strain. The fibre was kept strained for a time T_1 (initially 0.5 minutes), and subsequently released to relax for a time T_2 (always 5 minutes). The time lag of the fibre relaxation was visible in the bottom part of the relaxation curve.

The fibre relaxation can be divided into two relaxation ranges in terms of the wavelength: the fast linear elastic relaxation range $\Delta\lambda_{FAST}$, followed by the slow nonlinear viscous-dominated relaxation range $\Delta\lambda SLOW$. $\Delta\lambda_{FAST}$ is defined as the range where the fibre is following the (rapidly decreasing) strain applied by the motor. $\Delta\lambda_{SLOW}$ is defined as the range in which the fibre has a time-lag when relaxing, and does not follow the (rapidly decreasing)

strain anymore; it is defined to start when the rate of the FBG peak shift has decreased by a factor of 20.

To see the evolution of the time lag and the hysteresis it produces, we repeated the same strain cycle 10 times. The scheme explaining the procedure is shown in Figure 4-2, with $\Delta\lambda_{FAST}$ and $\Delta\lambda_{SLOW}$ ranges indicated in the right side of the figure.

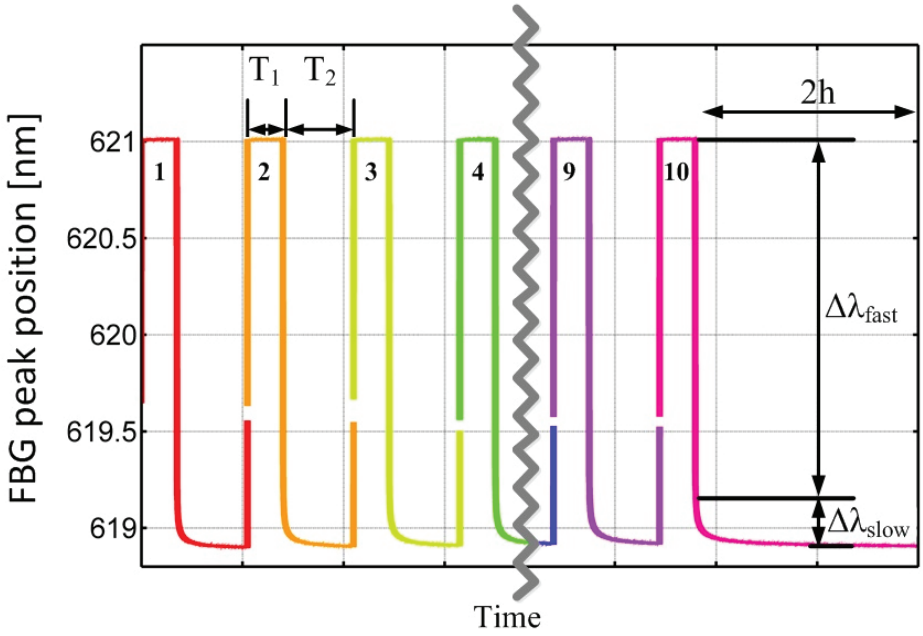

Figure 4-2. Schematic of a sequence of the experiment. The fibre has been strained (here 0.4%) for the duration T_1 after which it was relaxed for the duration T_2. After a sequence (10 repetitions of strain-relax cycle), the fibre was left relaxing for two hours to mitigate possible accumulated stress. The two main relaxation ranges are indicated in the right side of the figure: the linear (elastic-driven) fast relaxation range $\Delta\lambda_{FAST}$, followed by the nonlinear (viscous-dominated) slow relaxation range ΔλSLOW. $\Delta\lambda_{FAST}$ is defined as the range where the fibre is following the (rapidly decreasing) strain applied by the motor. $\Delta\lambda_{SLOW}$ is defined as the range in which the fibre has a time-lag and does not follow the (rapidly decreasing) strain anymore; it started roughly when the speed of the FBG peak shift becames 20 times slower than the motor speed.

The 10-cycle sequence was repeated 4 times with different values of the strain time T_1 (2.5, 5, 10 and 50 minutes), with the fibre relaxation time T_2 kept constant at 5 minutes. After each sequence the fibre was left relaxing for 2 hours to mitigate any possible accumulated stress before the new sequence took place.

In Figure 4-3, each of the 5 windows represents a different value of the strain time T_1. Each window contains 10 curves for 10 cycles (a sequence as shown in Figure 4-2) overlaid one over another.

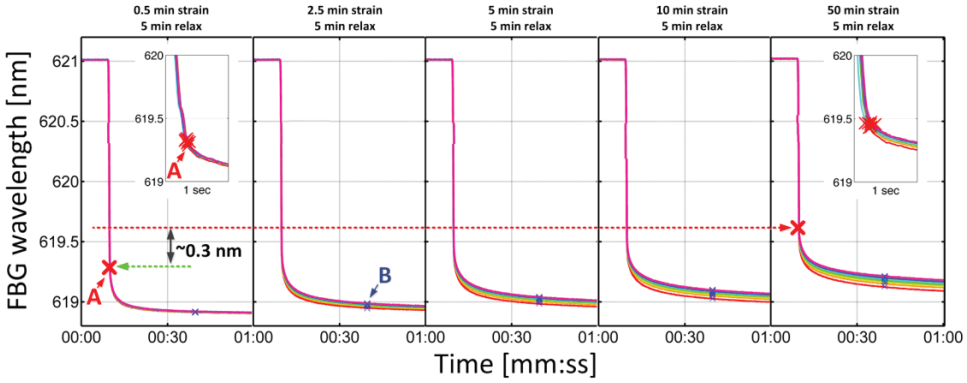

Figure 4-3. Strain-relaxation sequences for a strain level of 0.4%. Each window shows a sequence of 10 overlaid cycles as presented in Fig. 2. The strain time T_1 in the five windows is 0.5, 2.5, 5, 10, and 50 min, respectively, while the relaxation time T_2 was kept constant at 5 min. The point A (red X) marks the boundary between $\Delta\lambda_{FAST}$ and $\Delta\lambda_{SLOW}$, with the inset image showing it more precisely. The point B (blue X) marks the point 30 seconds after the start of the relaxation. It is apparent that with increasing strain duration, the fibre takes longer time to relax. The linear range $\Delta\lambda_{FAST}$ is decreased by 0.3 nm when the strain duration is increased from 0.5 min (dashed green arrow) to 5 min (dashed red arrow), thereby reducing the $\Delta\lambda_{FAST}$ range by about 18%.

For short strain times T_1 = 0.5 min, presented in the leftmost window of Figure 4-3, a relaxation time of 5 minutes is enough for a nearly complete relaxation of the fibre to where the FBG has the fully relaxed centre wavelength 618.7 nm. During the sequence no hysteresis is visible; all 10 curves seem to perfectly overlap one over another. With increasing strain time T_1, the fibre requires longer time to relax (the memory effect of accumulated stress [125]), and the 5 min relaxation time is no longer enough to sufficiently relax the fibre; as a result hysteresis starts appearing.

Looking at the most extreme case of T_1 = 50 min, the rightmost window in Figure 4-3, we find that $\Delta\lambda_{SLOW}$ reaches the value of 0.8 nm. The whole strain range is ≈ 2.3 nm, so $\Delta\lambda_{SLOW}$ takes up as much as 35% of the whole strain range. That means that in sensing application a free POF FBG sensor would not be able to monitor the strain in real-time during the last 35% of the relaxation. However, applying a sufficient prestrain found by monitoring $\Delta\lambda_{SLOW}$, the sensor could function in real time, which is the key subject of our further investigations.

4.1.2. Strain of 0.9%

The whole experiment was repeated with a strain of 0.65% and 0.9%, but for convenience of explanation we are presenting only the data for 0.9% strain, for which the strained FBG has a peak wavelength of 623.85 nm. In the leftmost window of Figure 4-4 it is observable that for 0.9% strain there is a small degree of hysteresis (the point B increases) even for the shortest strain time T_1=0.5 min, as the fibre does not manage to relax to the initial 618.7 nm within 5 mins, but stays above 619 nm. The hysteresis becomes more apparent and pronounced with increasing strain duration. For 0.9% strain $\Delta\lambda_{FAST}$ is more than twice that for 0.4% strain. For the short strain time of T_1=0.5 min $\Delta\lambda_{FAST} \approx 1.8$ nm for 0.4 % strain, while for 0.9% strain it is $\Delta\lambda_{FAST} \approx 3.8$ nm. For the longest strain time T_1=50 min we find $\Delta\lambda_{FAST} \approx 1.5$ nm for 0.4% strain, while for 0.9% strain $\Delta\lambda_{FAST} \approx 4.2$ nm.

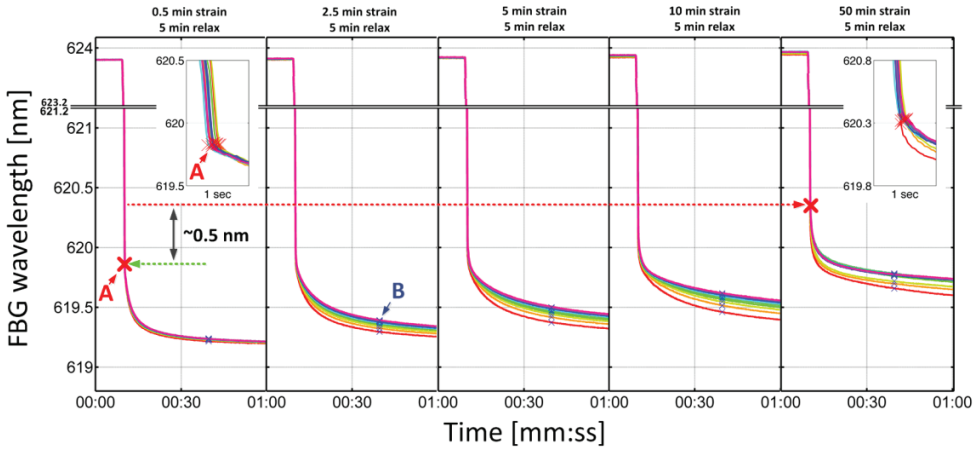

Figure 4-4. 10 cycle strain-relaxation sequence for a strain of 0.9% and different durations of strain T_1 (same marking as in Fig. 3). The wavelength range $\Delta\lambda_{FAST}$ is decreased by 0.5 nm when the strain duration is increased from 0.5 min (dashed green arrow) to 50 min (red arrow), thereby reducing the wavelength range of fast contraction $\Delta\lambda_{FAST}$ by about 13%.

There appears to be an increase in FBG wavelength when the fibre is strained in Figure 4-3 and Figure 4-4, which is more visible in the Figure 4-5. During that straining time the motor stretching the fibre is holding the same position, but the FBG wavelength rises. The wavelength rises for each of the curves (with strain time T_1=0.5-50 min) when comparing the cycle 1 and cycle 10, which means this effect is not due to temperature. Furthermore, it rises more for longer

T_1-s than for shorter. The acrylic glue used to glue the fibre to the motorized stage is more rigid than the fibres which shouldn't make glue's contribution significant.

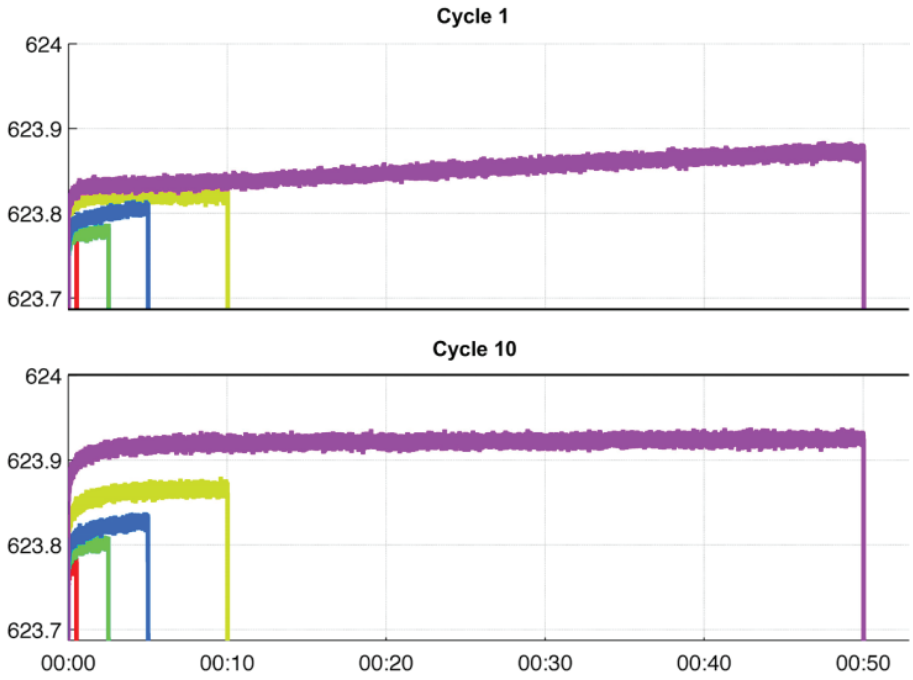

Figure 4-5. FBG growth during the straining time. It appears that for the longer strain times, and especially for the fibre which experienced the longest total strain time (50 minutes, 10th cycle), the FBG wavelength keeps rising to certain value.

We believe that this increase is due to internal rearrangement of the polymer chains which release the tension in the fibre and, through it, influence the FBG wavelength. However, another study would be needed to thoroughly investigate this behaviour. It should be noted that, in case this effect really is due to internal rearrangement of the polymer chains, it could be playing an important role also in embedded sensors.

4.2. Time-lag evolution

To observe the change in the relaxation time-lag, the fibre was examined 30 seconds after the start of relaxation, marked with a blue X and labelled B in Figure 4-3 and Figure 4-4. This point is easy to track automatically and is well into the viscous part of the relaxation in all cases in Figure 4-3 and Figure 4-4. Thus, a significant change in the FBG wavelength at point B should be visible when changing the strain time T_1. The evolution of the FBG centre wavelength at position B with the number of strain cycles is shown in Fig. 6 for different strain times T_1. It is apparent for both 0.4% strain [Figure 4-6 (a)] and 0.9% strain [Figure 4-6 (b)] that for the shortest strain time T_1=0.5 min (red curves) the fibre can follow the strain cycle with almost no hysteresis, i.e., the FBG centre wavelength after each cycle is almost constant.

When increasing the strain duration T_1 (orange, yellow, green, and turquois lines), the accumulated stress influences the subsequent cycles because the fibre cannot fully relax within the fixed relaxation time of T_2=5 min. As a consequence hysteresis starts appearing, i.e., the wavelength at point B increases with the number of strain cycles. However, importantly the wavelength at point B is seen to saturate towards an equilibrium, at which hysteresis has again disappeared. For the longest strain durations T_1, the equilibrium has not been reached after 10 cycles and thus hysteresis is still present. For shorter T_1, it appears that the fibre comes close to an equilibrium at which hysteresis is no longer present.

When comparing 0.4% and 0.9% strain, perhaps the most apparent observation is the big offset in the FBG positions measured at point B. They are different by at least 0.3 nm, which corresponds to about 0.9% strain. The wavelength at the B points is higher for 0.9% strain than for 0.4%, but the FBGs strained for 0.9% still have an overall much bigger fast relaxation range $\Delta\lambda_{FAST}$ due to the larger total strain.

The main reason that the light green curve for T_2=50 minutes in Figure 4-6 (b), is not as smooth as the other curves is due to a drift in the otherwise humidity and temperature controlled environment.

We would now like to investigate the viscoelastic response of the mPOF FBG and in particular follow how the fast and slow response regimes $\Delta\lambda_{FAST}$ and $\Delta\lambda_{SLOW}$ vary with the strain time T_1. It would be highly important for applications if the disappearance of the hysteresis after a certain number of strain cycles observed in Figure 4-6 translates into an upper limit of the slow viscous regime $\Delta\lambda_{SLOW}$. This would mean that the mPOF FBG sensor could be characterized by a constant available fast relaxation range independent of the number of strain cycles. By adequate prestraining, the sensor could then be made to follow the applied strain perfectly.

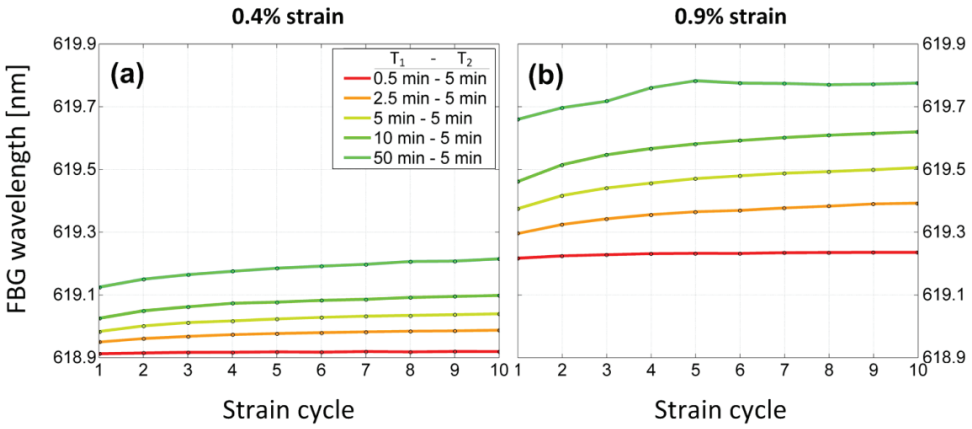

Figure 4-6. Centre FBG wavelength at point B, which is 30 seconds after the start of relaxation (see marks in Figs. 3- 4), versus the number of strain cycles in a 10-cycle sequence. The sequences with 0.4% strain are shown in (a), while the sequences with 0.9% strain are shown in (b). For each strain level we show 5 sequences with varying strain time T_1.

To follow $\Delta\lambda_{FAST}$ and $\Delta\lambda_{SLOW}$ we have manually evaluated the wavelength level separating the two regimes, which is marked as the red point A in Figure 4-3 and Figure 4-4. In Figure 4-7 we plot this wavelength versus the strain time T_1, both when measured in the first strain cycle (blue curves) and in the last 10th strain cycle (red curves). In addition to 0.4% and 0.9% strain, we also plotted the data for 0.65% strain. The results are showing that with increasing strain time T_1, the wavelength at point A (and therefore $\Delta\lambda_{SLOW}$) increases but eventually reaches an equilibrium. This indicates that, at least for these strain levels, there will always be a considerable amount of $\Delta\lambda_{FAST}$ even if the strain durations are longer than 50 min.

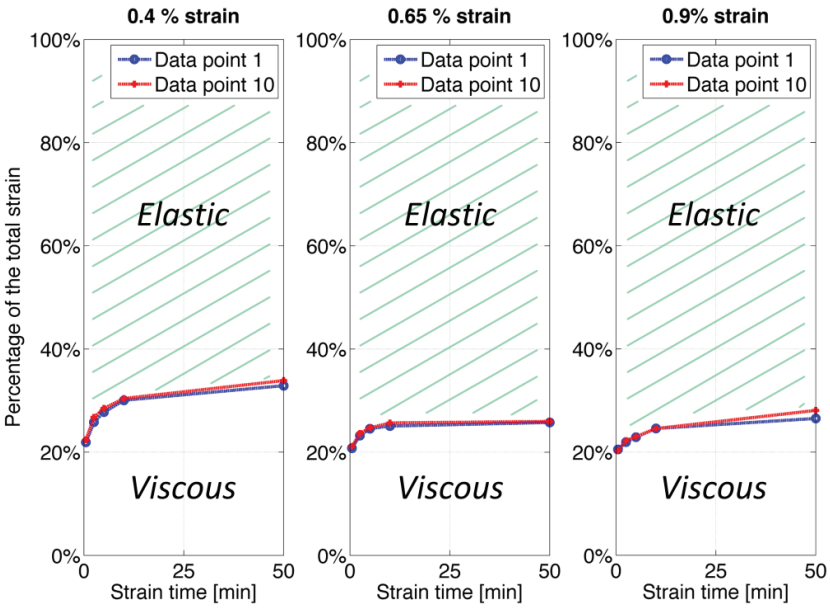

Figure 4-7. Wavelength at point A versus strain time T_1, for 0.4% strain (left), 0.65% strain (centre) and 0.9% strain (right). The Y-axis is scaled to percentage of total strain for direct comparison. For both the first and the last 10th iteration (red and blue curves, respectively), after 50 mins $\Delta\lambda_{FAST}$ shrank to about 70% of the total strain, for each of the different strain levels. The values for the 10th strain cycle differ by less than 3% (of the total strain range) from the values for the first iteration.

Table 6. Summary of $\Delta\lambda_{FAST}$ and $\Delta\lambda_{SLOW}$ for 0.4%, 0.65% and 0.9% strain for shortest and longest strain duration T_1. The values are taken for the 10th cycle (red curves presented in Figure 4-6). The brackets give the percentage of the total strain that the particular wavelength range corresponds to.

	T_1=0.5 min $\Delta\lambda_{FAST}$	T_1=0.5 min $\Delta\lambda_{SLOW}$	T_1=50 min $\Delta\lambda_{FAST}$	T_1=50 min $\Delta\lambda_{SLOW}$
0.4% strain	1.8 nm (78%)	0.5nm (22%)	1.5nm (65%)	0.80nm (35%)
0.65% strain	3.1 nm (79%)	0.8nm (21%)	2.9 nm (74%)	1nm (26%)
0.9% strain	4.2 nm (79%)	1.1 nm (21%)	3.8 nm (73%)	1.4 nm (27%)

The main conclusion from Figure 4-7 and Table 6 is that for the strain times and strain levels tested here, the desired fast relaxation range $\Delta\lambda_{FAST}$ always covers more than 65% of the whole strain range. One should keep in mind that these values are valid for unembedded sensors and that the relaxation will be dependent on the host material if the sensor is embedded [126].

It should be noted that after the experiments were conducted, the fibre took about a week to relax completely to have the FBG centre wavelength at the initial unstrained value 618.7 nm.

4.2.1. Strains from 0.9% to 4.9%

Considering that this study only involves small strain, one remaining question is what happens at larger strain levels. To get an insight into what happens at larger strain levels we repeated a single cycle experiment at several larger strains. After a two-week long relaxation of the fibre, we strained the same fibre for T_1= 5 minutes with the strain of 0.9%, 1.9%, 2.9%, 4.1% and 4.9%. The relaxation time T_2 was kept at 2 hours. The resulting relaxation curves are plotted in Figure 4-8, with time on the x axis shown in logarithmic scale, which more clearly shows the relaxation curve and makes it easier to observe the point A (marked with a black circle).

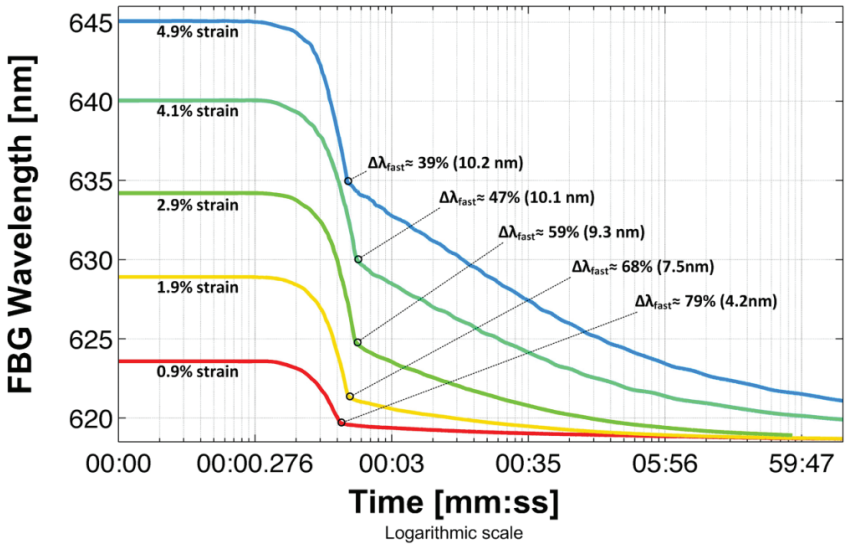

Figure 4-8. Relaxation of the fibre strained for T_1=5min at 0.9%, 1.9%, 2.9%, 4.1% and 4.9% strain.

With increasing strain, we observe that $\Delta\lambda_{FAST}$ is reduced from 79% to only 39% of the total strain amount, as the strain level is increased from 0.9% to 4.9%, respectively. This could be due to the fibre approaching the yield strain, the limit of quasi-elastic behavior, which is usually around 6% [123]. However, the absolute amount of $\Delta\lambda_{FAST}$ was growing each time the

strain level was increased: From 0.9% to 4.9% strain, $\Delta\lambda_{FAST}$ goes from 4.2 nm to 10.2 nm, respectively.

Even though the absolute value of $\Delta\lambda_{FAST}$ increased, the increase is not a linear one. The increase to $\Delta\lambda_{FAST}$ was getting smaller for each increase of strain level. The $\Delta\lambda_{FAST}$ gain between 4.1% and 4.9% strain was only 0.1 nm (from 10.1 nm to 10.2 nm). This behavior indicates that the strain levels at about 4-5% could be the limit for a free-standing sensor requiring real-time response.

It should be noted that the fibre was strained for 5 minutes, making only one cycle at each strain level, so there is a degree of stress memory in fibre that possibly influenced the high strain levels.

4.3. Operational range for FBG sensors

Our results have shown that the viscous range of the sensor, $\Delta\lambda_{SLOW}$, stays below 35% of the total wavelength shift due to the strain, for all the covered strain levels and strain and relaxation times. The apparent saturation in the growth of the undesired slow viscous response $\Delta\lambda_{SLOW}$ is important. It implies that if the mPOF FBG sensor is pre-strained to shift the FBG wavelength sufficiently more than the upper limit of $\Delta\lambda_{SLOW}$ then the response of the sensor would always be in the instantaneous $\Delta\lambda_{FAST}$ regime.

To confirm this, an additional test has been made. A new fibre has been strained for 1 hour at 1% strain (FBG wavelength going from 602.1 nm to 607.9 nm) and after that relaxed to determine the point A (the beginning of $\Delta\lambda_{SLOW}$ shown in Figure 4-3 and Figure 4-4). The value of point A was determined to be at 603.7 nm, which gives a $\Delta\lambda_{SLOW}$ about 28% of the total strain range, which is somewhat lower than expect for 1h strain at 1% according to Figure 4-7 and Table 6. However, one should remember that this is a new fibre from the same fibre spool, but with a new FBG.

For a proof-of-principle experiment we then pre-strained the fibre with 0.6% strain (FBG wavelength at 605.6 nm) to be absolutely certain to have no visible effects of the viscous regime

$\Delta\lambda_{SLOW}$. To push the limit we performed 10 strain cycles with the sensor, in which the fibre was strained to 1% and relaxed to about 0.6%

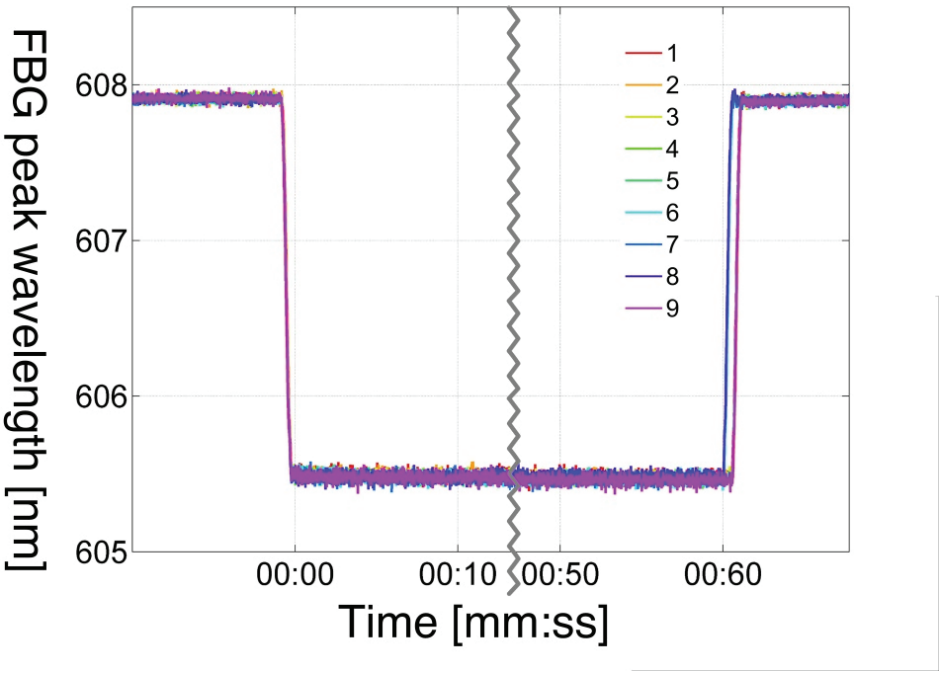

Figure 4-9. A sequence of 10 strain-relax cycles where strain amounted to 1% and relax to 0.6%. The relaxation range $\Delta\lambda_{FAST}$ has been determined after straining the fibre for 1h at 1% and then completely relaxing to find the point A which was standing at 0.28% of the total strain. Afterwards, the fibre has been strained to 1% and relaxed to 0.6%, a value which was selected as it is sufficiently above measured point A. It appears that the FBG peak is following the motor movement very precisely without any time lag in response. A difference in the start of the rise for certain curves originates in counting error of the software running the strain motor, which sometimes adds a second on the 60 seconds count

The 10 overlaid cycles are shown in Figure 4-9 and as expected the FBG peak is indeed seen to follow the rapid motor movement very precisely without any time lag. On the upstrokes seen in the Figure 4-9, there is sometimes a slight time-offset due to software counting error.

These results suggest that even for longer strain times than the ones tested here, we can tailor our sensor for the optimum operation by prestraining it above $\Delta\lambda_{SLOW}$. For longer strains, it would be necessary to first find $\Delta\lambda_{SLOW}$ and then operate the sensor at 10% or more above it.

4.4. Summary

Polymer fibres exhibit viscoelasticity, which makes them more difficult to implement as certain types of sensors, although they have certain properties that make them advantageous over the silica-based sensors. We have shown that, depending on the amount and the duration of the strain, complete fibre relaxation will vary. When cyclically straining and relaxing fibre, hysteresis will appear if the relaxation time is not long enough.

We have also demonstrated that the mainly elastic fast relaxation range $\Delta\lambda_{FAST}$ decreases with the strain duration and the strain amount, while viscous time-lagged slow relaxation range $\Delta\lambda_{SLOW}$ increases. For the investigated time scales of period, viscous relaxation region can amount up to 35% of the total strain applied, for the total strain of 0.9%. With increasing strain, from 0.9% to 4.9%, the total amount of $\Delta\lambda_{FAST}$ increases even though it takes less and less of the total strain range as $\Delta\lambda_{SLOW}$ grows much faster. Furthermore, any appearing relaxation behaviour will become identical for each of the following strain-relax cycles, as after certain number of cycles the hysteresis reaches an equilibrium.

If the fibre is strained and relaxed within its fast relaxation region, the FBG reflection peak will follow the applied strain without a time-lag and, in that region, the optimum behaviour of the sensor can be expected.

Chapter

5

POFBG based Microphone

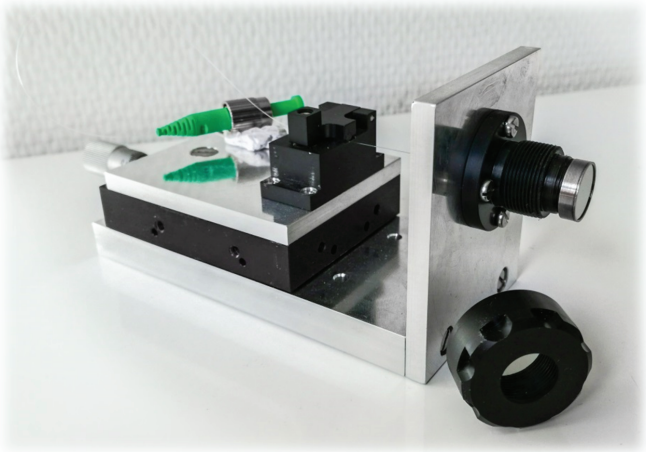

Possibilities of grating based sensors are often limited to their inherent property to sense humidity, strain and temperature. However, like with many other sensors, with a proper transducer, sensing options are enlarged. The technology to sense acoustic waves with fibre optics has been developed in silica fibres for use in harsh environments, or simply in environments where presence of electrical components is unwanted. One possible advantage is remote acoustic sensing, as the signal-reconstruction system can be far away from the sensing head.

A sound wave is a pressure wave travelling through the medium, most commonly air. Commercial microphones strongly rely on membranes; they vibrate with the changing pressure and these vibrations which they produce are translated into small signal through a change in capacity between the membrane and a back plate (or other similar mechanism). Moreover, these

membranes are also acting as simple mechanical amplifiers as they are thin and wide, and are picking up small and fast changes in pressure. As FBGs change the central wavelength depending on the change of Bragg period, and the latter can be induced by sound – the sound pressure changes can be picked up by FBG sensor.

Acoustic sensors of different kinds based on silica FBGs were demonstrated by several groups and some companies [127]. For producing a plastic optical microphone there are two main, mutually dependent limitations. First one is the strength of the signal: the pressure changes translate into very small contractions of the FBG period which produce small shifts of the FBG wavelength. The second limitation is a FBG wavelength recovery system, the peak tracking system has to be fast enough to sample desired frequencies with sufficiently good quality. Present day systems, such as "High Speed IMON" from Ibsen Photonics, can go up to the sampling frequency of 35 kHz at 1550 nm, which is silica low-loss window and is not very suitable for polymer fibres. That sampling frequency is achievable for strongly reflective gratings, which require short integration times. Considering that human ear can hear frequencies from 20 Hz to 20 kHz, even these modern systems are still unable to completely cover those frequencies.

The microphone that was presented by Stefani *et al.* [18,128] had a fork-like mechanical amplifier attached to a membrane; the fibre containing the FBG was standing in a parallel plane to the one defined by the membrane. They showed nearly linear response throughout investigated range of 6 kHz, with the system's resonance standing between 3-5 kHz.

In the experiment presented in the following, we investigate somewhat different approach. We first investigate the sound response of a thin bare fibre containing an FBG at the tip of it. Subsequently we investigate the influence of a fibre with a tip attached to a membrane, acting as a mechanical amplifier, and pointing to the incoming sound field.

5.1. The Bare Polymer fibre FBG microphone

The experimental setup consisted of a speaker, stage for holding the fibre, reference microphone standing above the fibre and the I-MON interrogator from Ibsen Photonics, as shown in Figure 5-1 and Figure 5-2.

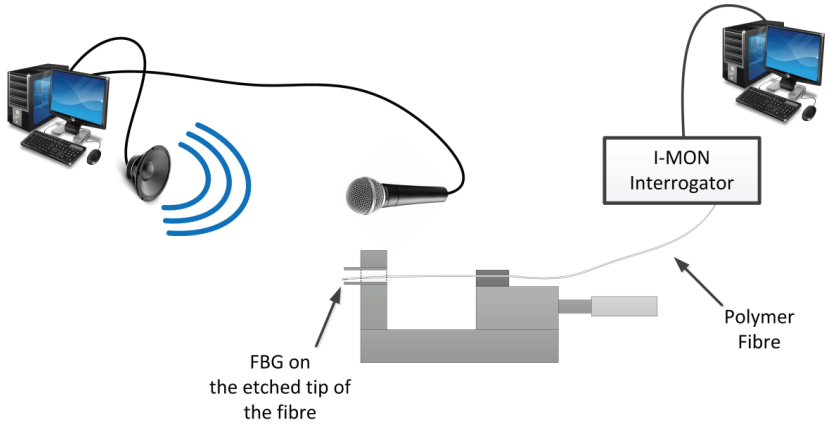

Figure 5-1. Scheme of POFBG microphone test. A speaker was used to create sound signal which was detected by the POFBG attached to the I-MON. The fibre containing FBG was etched to 63 µm at the position of the FBG and was cleaved 3 mm away from it. Commercial calibrated professional microphone model 4192 from B&K was used to measure sound levels for data comparison.

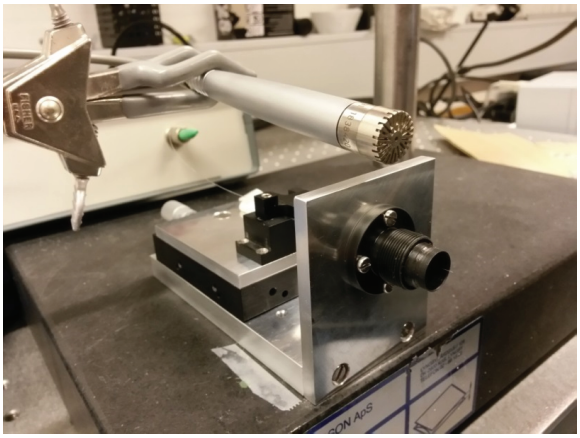

Figure 5-2. POFFBG holder with reference microphone B&K 4192.

The fibre sensor fabricated for this experiment had an FBG centred at 845.6 nm with reflectivity of 28 dB in reflection; it was annealed at 90ºC for 2 hours before FBG inscription. The fibre used was 150 µm in diameter, but was etched with ethanol to 63 µm in diameter at

the position of the FBG to enhance its sensitivity. It was cleaved 3 mm away from the FBG on one end. The other, longer, side of a fibre was sleeved in standard 125 μm ST silica connector from ThorLabs; the surface of the fibre end was polished for optimal performance upon connecting to I-MON.

The interrogation system I-MON 850-FW from Ibsen Photonics detects and records the FBG peak. The peak fitting I-MON software employed the Dynamic Gate Algorithm to obtain the peak central wavelength. The buffer of I-MON allowed for about 11 second of recording before the files had to be saved to disk. The sampling frequency of I-MON depended on the reflectivity of FBG signal; it was set to 8200 Hz to have the optimal results with our grating, and sufficient detectable frequency range of 4 kHz.

The FBG sensor was exposed to the single frequency sound excitations of 92 ±1 dB. The sound pressure was monitored through reference commercial microphone Brüel & Kjær 4192, the microphone was standing couple of centimetres above the fibre with FBG, as shown in Figure 5-2.

5.1.1. Single frequency excitation

Fibre was subject to 6 single frequency excitations: 500 Hz, 750 Hz, 1 kHz, 2 kHz, 3 kHz and 4 kHz, one after another. Fibre tip was standing 1 m away from the speaker and the sound pressure levels measured were 91.8 ± 0.4 dB, except for 500 Hz and 4 kHz when they were 94.8 dBs and 90 dBs respectably. These sound levels are corresponding to the levels produced by a subway train, lawn mower or a motorbike. The fibre output was initially optimised for a maximum at 1 kHz.

During post-processing of data in Matlab, it was found that sampling frequency of I-MON shifts considerably between 8300 Hz and 7700 Hz. That made it difficult to make the Fourier transformation (FTT) on the obtained data. The data presented in the following was linearly interpolated and therefore contains a degree of error as well as considerable amount of Fourier transformation artefacts – some coming from the I-MON itself and some from the interpolated

data. A small discussion on the origin of artefacts is presented in the section 5.2 of this Chapter. The obtained Fourier transform spectra are shown overlaid one over another in Figure 5-3.

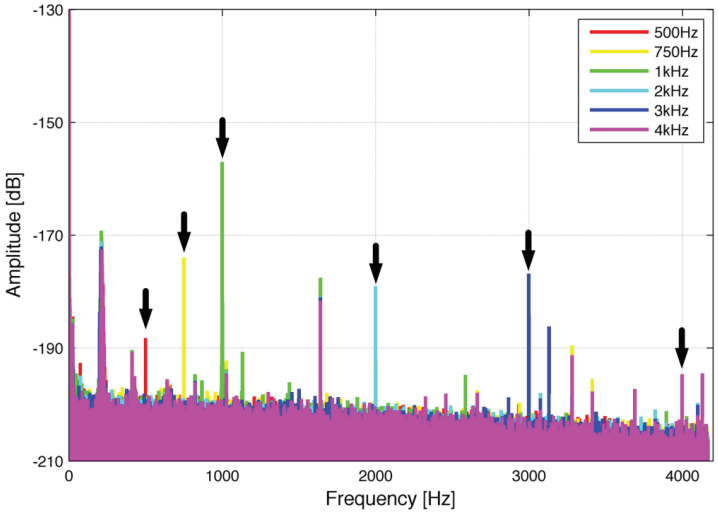

Figure 5-3. Overlayed spectra of single frequency sound excitation obtained with I-MON. Reference of the amplitude dB scale is 1 meter. The speaker, standing 1 m away from the bare fibre tip with an FBG grating, played 500Hz, 750 Hz, 1 kHz, 1.5 kHz, 2 kHz, 3 kHz and 4 kHz pure tones. The I-MON FTT artefacts stand at 250 Hz, 1700 Hz and 3250 Hz; other artefacts are from interpolation (see section 5.2). The resonance of the system is clearly visible around 1 kHz.

In comparison to the sound levels which are varying for 5 dB maximum (between 500Hz and 4 kHz data), the values sampled by FBG have much bigger spread, indicating high nonlinearity of the system. Amplitude displacement is shown in dB scale for easier comparison with membrane and microphone data in the following section. Normalised displacement values range from -194 dB (4 kHz) to -155 dB for (1 kHz). That gives a spread of 39 dB.

5.1.2. Frequency chirp excitation

Following single frequency excitation, a frequency chirp was repeatedly played through the speaker with a period of 1 second. Sound chirp is a sweep excitation signal over a band of frequencies - in our case sound increased from 20 - 20000 Hz, covering the range of frequencies hearable to human. Due to energy being distributed over a broad band of frequencies, the energy delivered to the speaker and to the fibre, for each frequency component was small. The FBG measured signal was therefore small. The signals obtained by the microphone and I-MON are shown in Figure 5-4 and Figure 5-5 respectively. The sound pressure levels were held at 70 dBs not to damage speakers, with two dips of 60 dBs at 1500 Hz and 2500 Hz, and peaks of 76 dBs at 500 Hz and 1200 Hz. These are about 20 dB lower than levels used for single frequency excitation. For reference, sound levels of 70 dB are equivalent to volume of a TV or radio.

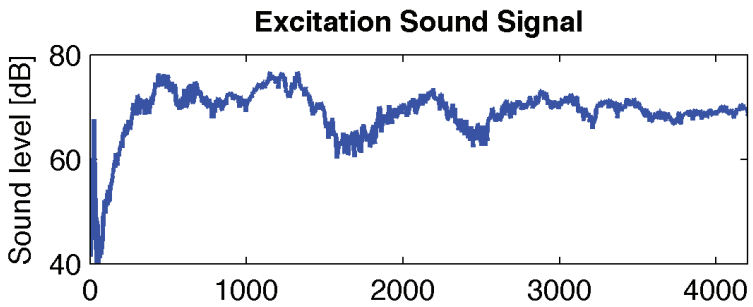

Figure 5-4. Frequency spectrum of chirp sound excitation, measured by the reference microphone Brüel & Kjær 4192.

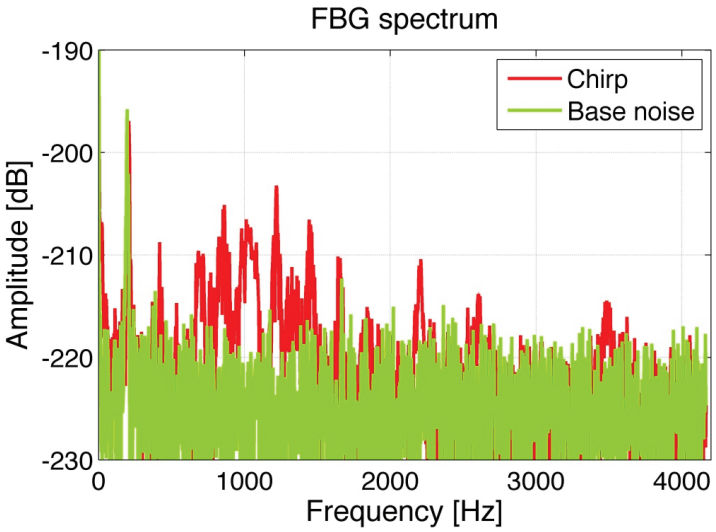

Figure 5-5. POFBG sensor output upon excitation with chirp. The output spectra is very small, barely noticeable on a dB scale, with bandwidth rising around 1 kHz.

The output spectrum that I-MON collected is very noisy and weak. There appears to be a rise around 1000 Hz, 2200 Hz and 3500 Hz but otherwise the signal is reaching only about 10-15 dB at highest levels. The FFT was calculated for each chirp period and the FFT amplitudes of same chirp periods were subsequently averaged lowering the fluctuations of the acquired spectrum.

Even though the resulting signal was weak, for the sensors with extremely small surface area, detection of these signals is already a considerable stretch.

5.2. Membrane assisted POFBG microphone

To enhance responsivity of the FBG to the sound excitation, professional microphone heads from Brüel & Kjær are used, as shown in Figure 6-2 a). The heads are having extremely thin layer of metal foil, half-inch in diameter, stretched over a metallic ring.

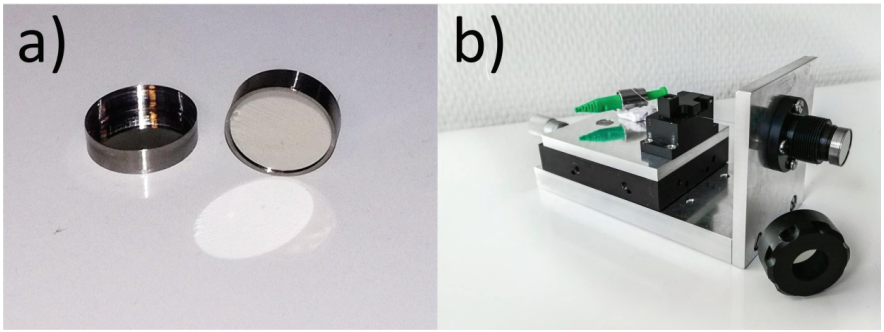

Figure 5-6. Image of a half-inch microphone (membrane) heads from Brüel & Kjær to which POF with FBG was glued (a) and image of the POFBG microphone (b). The internal thread cap, standing by the setup, is used to apply tension on the membrane. The screw standing at the left-back side of the holder was used to apply prestrain to the fibre.

The exact thickness and material of a membrane are not known as the heads are not commercial products. The fibre tip with a grating was glued to the centre of the membrane with a small amount of acrylic (super) glue. Fibre was secured with a clamp, forming about a 5 cm long cavity between clamp and a membrane. The clamp was on a movable stage allowing for pretensioning of the fibre. The membrane was mounted to microphone holder as shown in Figure 5-6 b). The internal thread cap was put over the membrane head; it allowed for adjustment of membrane's surface tension.

To get a better insight into underlying processes occurring when the fibre is attached to the microphone membrane and exposed to the sound waves, the vibrations of the membrane were monitored with Polytec Laser Vibrometer PSV-400-M2. The Vibrometer uses an internal laser and through interferometric technique, it retrieves the vibration velocity of the membrane. From the vibration velocity, Polytec software calculates the displacement of the membrane over frequencies. The new setup is visible in Figure 5-7. The membrane displacement (velocity) was monitored at its centre, where the fibre was attached to it. The fibre sensor, which was free

hanging, was minimally prestrained to straighten-out the fibre, and the membrane was slightly pretensioned. Note that the tension of the membrane was not controllable except for the observable FBG output.

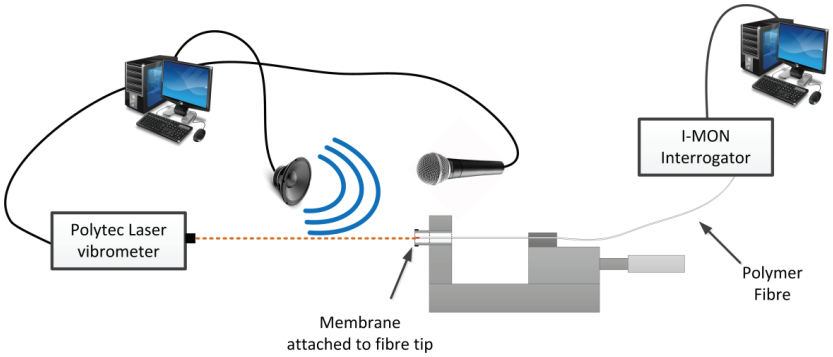

Figure 5-7. Scheme of membrane assisted POFBG microphone experiment. A speaker was used to create a sound signal which was detected by the POFBG attached to the microphone membrane. Laser Vibrometer was used to detect movements at the centre of the membrane where the fibre was attached.

This microphone system was excited by the same single frequency and chirp excitation as presented previously. Results are presented in the following.

5.3. Single frequency excitation

During acquisition of single frequency data with I-MON, in FFT window of the I-MON software the sampled peaks were seen to behave inconsistently, to “jump up and down”. That behaviour could be partially due to excitation of resonances of the fibre and membrane. However, with post-processing it was discovered that I-MON, for unknown reason, changes its sampling frequency. For correct frequency spectrum, for looking at spread and amplitude of different frequency components, it is imperative that sampling is done with a fixed sampling rate.

To recover the signal, a linear interpolation between the data points was made as it is shown in Figure 5-8. The top graph shows 1 kHz and 2 kHz data sampled with laser vibrometer at the centre of the membrane, where the FBG fibre tip was glued. Higher harmonics are visible at 3 and 4 kHz which is common in loudspeaker systems. Middle graph shows normalised FFT of the data obtained by I-MON, both frequencies show offset with respect to central frequency, in

case of 2 kHz excitation – that offset is considerable and amounts to about 120 Hz. Moreover, in case of these two components, offsets are in opposite directions, as it is indicated with black arrows. The bottom graph shows FFT of linearly interpolated signal. The central wavelengths are at correct positions, 1 kHz signal looks cleaner with respect to harmonics which appear in its spectra, but 2 kHz signal unfortunately has many FFT artefacts around the central wavelength.

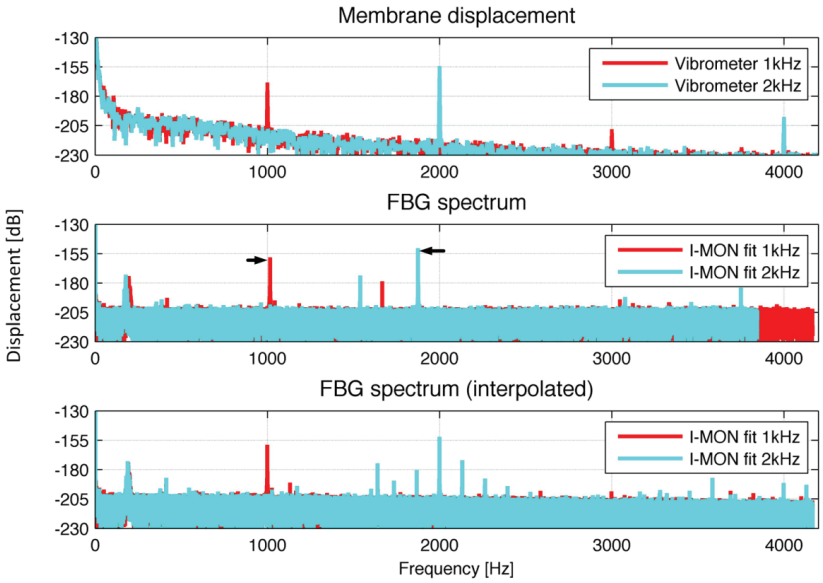

Figure 5-8. Three graphs showing membrane displacement obtained with vibrometer (top), FFT spectrum of I-MON (middle), and FFT spectra obtained over interpolated data (bottom). As I-MON did not use fixed sampling rate, straightforward FFT gave considerable shifts, as shown with arrows in the middle graph. Data had to be interpolated to have more accurate estimate of central amplitudes.

Even when not sampling anything, I-MON spectra shows two or three constant frequency components. They are at 250 Hz, 1700 Hz and 3250 Hz, and are due to errors induced by the system itself.

In Figure 5-9 all single frequency sound excitation signals are shown (500 Hz, 750 Hz, 1 kHz, 2 kHz and 3 kHz). The top graph shows reference microphone levels, middle graph shows displacement of a vibrometer

The FBG shift clearly shows improvement in sound detection with rise of all the single frequencies, especially at 1 kHz and higher. But in comparison to the magnitude of vibrations measured with a vibrometer, the two data do not seem to be correlated with respect to measured magnitudes. When looked at, for example, 750 Hz and 3 kHz, membrane displacement is almost equal but recorded FBG shift shows very small values for 750 Hz and the biggest value for 3 kHz. A similar behaviour can be seen for burst chirp in Figure XX.

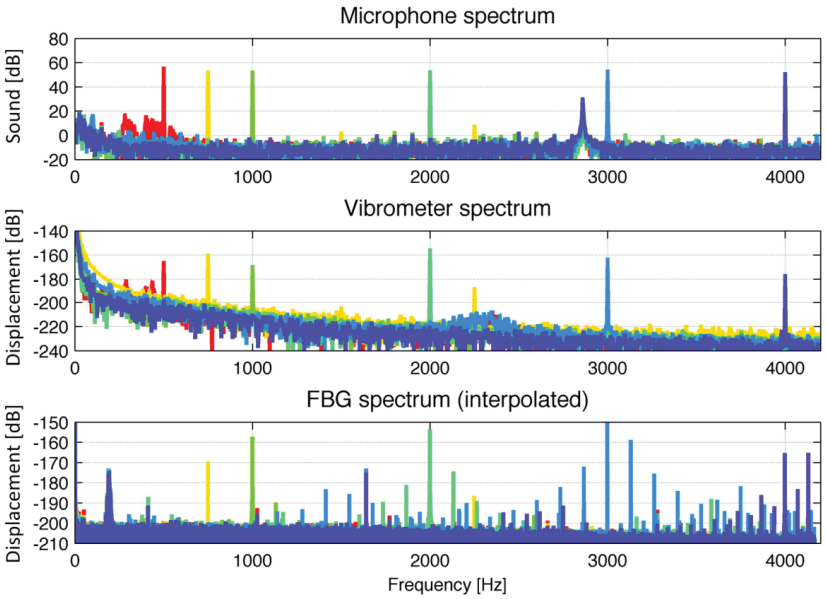

Figure 5-9. Response of the POFBG microphone with membrane amplifier to single frequency excitations. Top graph shows sound levels detected with reference microphone, middle graph shows membrane vibrations and the bottom one shows interpolated FBG spectra. There does not seem to be a strong correlation between amplitudes of membrane displacement and detected FBG frequencies: while incoming sound is quite uniform for each of the frequencies(reference microphone), displacements of the membrane shown with the vibrometer indicate variations of up to 20 dBs between certain frequency components. I-MON spectrum shows similar behaviour, but it is not correlated to vibrometer spectrum: 500 Hz and 1 kHz components, as well as 3 and 4 kHz components grow for the FBG while decreasing for the membrane spectrum (and vice versa).

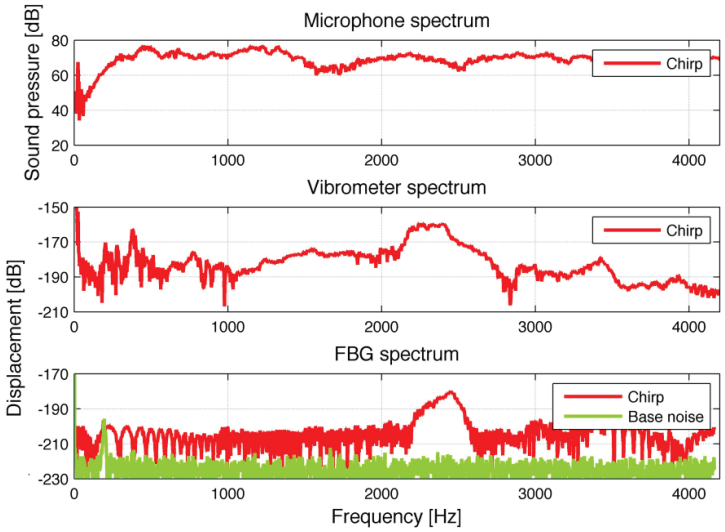

Figure 5-10. Graph showing optimised response of the POFBG microphone (bottom) with respect to sound (top) and membrane (middle) vibrations. The fibre was strained and membrane was tensioned to tune the output for the best results. Effect of different prestrains and membrane tensions to FBG output is shown in Appendix 2.

Prestraining of the fibre seems to influence the overall output much more than membrane tension did, however the real influence could not be determined as only manual adjustment was made; prestrain and tension of the membrane were adjusted by looking at the FFT spectrum of I-MON and maximising its amplitudes. Different frequency bands could be amplified but we were unable to get a uniform and broad spectrum. Figure 5-9 is showing the highest amplification we could achieve through manual adjustment. The most amplified regions is about 500Hz wide, and it stands between 2 kHz and 3 kHz. Amplification in that region rises to -180 dB, while it stays around -200 dB elsewhere.

When comparing the displacement of the membrane and the displacement that FBG measures, vibrometer data was about 2 orders of magnitude stronger (20 dB). At 2 kHz we measured 0.68 pm RMS value of amplitude of I-MON, and 14.3 pm for membrane. However, that is strongly dependent on prestrain and tension that are applied to fibre and membrane respectively. This could be due to number of reasons, some of them are losses of fibre due to its rubbery/viscous nature, Poisson's ratio (wavelengths of measured sound waves are cm long, growing at low frequencies up to meters), glue, etc. Another interesting unknown is how the

FBG output changes with frequency, and why, as in certain cases FBG frequency amplitudes approached values that vibrometer was measuring on the membrane.

5.4. Summary and discussion

It seems that broadband sensitivity of this type of simple microphone setup does not yield uniform and satisfying frequency response. Some of the potential and possible actors in it could be internal resonances of the fibre, viscous dampening, dampening due to glue, Poisson's ratio and other. On the positive side, what was observed is that even bare fibre can pick up considerable sound frequencies. If the fibre was etched even more, cleaved closer to the grating it might be used potentially, even in this configuration, for certain acoustic applications.

One of the big limitations of this experiment was I-MON interrogator which did not sample the data with a fixed frequency. Due to that, much of the data was not completely comparable with the membrane displacement data obtained by Polytec laser vibrometer. The linearly interpolated data give a good insight but are not sufficient for good conclusion.

Some other methods could be used for acoustic sensing, besides peak detection with interrogators such as I-MON, methods that do not depend on reconstruction of the complete FBG peak and therefore are much faster. One such method could be detection of the FBG peak's edge. That would require a narrow bandwidth laser (or a filter), positioned just at the falling edge of the FBG peak. Small shifts of the FBG central wavelength under influence of a sound wave would then be translated into amplitude oscillations which are easily detectable with a high speed photodiode.

Chapter

6

Long Period Grating based All-plastic Endoscope

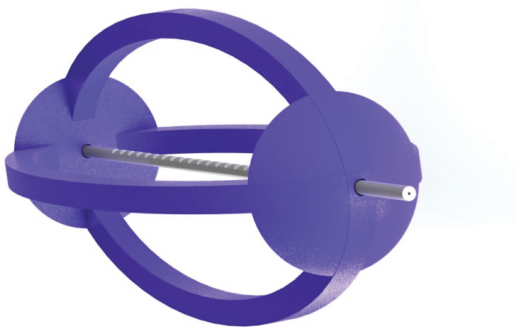

This Chapter along with majority of its graphs, tables and images is based on the following publication: "All-plastic fibre-based pressure sensor" [129]

Both FBGs and LPGs consist of a periodic perturbation in the core of an optical fibre which result in a spectrally narrow reflection (FBG) or attenuation (LPG) band [130], depending on the properties of the fibre and the period of the grating. LPGs have been reported in mPOF and they have been fabricated using mechanical imprinting methods [67] and UV techniques [131]. Different LPG sensing applications have been investigated in various contexts [29,30,45,91,101,105,109,112,132–134]; they were mainly based on strain, temperature and humidity sensing.

In this Chapter we report on the demonstration and characterization of an entirely polymer fibre-based pressure sensor developed at University of Sydney. While there are various pressure

sensors developed with silica fibres, their main limitation is flexibility and sensitivity to pressure [135]. We utilize a single-mode mPOF with an LPG and a transducer to convert pressure to strain. The LPGs in the single-mode mPOF are inscribed using a CO_2 laser for the first time. The response of the sensor consisting of the transducer and fibre grating to lateral force and also pressure is characterized. The role of various parameters such as the fibre diameter, the strain applied to the fibre when assembling the sensor, and the glue used to assemble it is also characterised with a view to optimising the sensor's response.

A motivation for this work was interest in polymer grating-based biomedical sensing, where the polymer's flexibility and biocompatibility offer a potential for in vivo sensing, or sensing in contact with the body. Such potential applications include pressure sensing in bandages [136], or the investigation of colonic motor disorders [137,138]. The diagnosis and study of the latter requires monitoring of the pressure in the colon continuously and in multiple places at once, over a range of up to 250 mBar. This has been achieved recently with silica fibre FBG-based endoscopic sensors [138–140]. When developing new endoscopic equipment, the cost, function and biocompatibility of new devices play a crucial role. This work was the first step towards incorporating the biocompatibility and increased flexibility of polymer fibres into such a sensor.

6.1. CO_2 laser inscription of LPGs in PMMA fibres

Two different microstructured polymer optical fibres, fabricated at University of Sydney, were used in this work. The first was made of PMMA and had a polycarbonate external jacket with an outer diameter of 310 μm. The microstructure consisted of the typical triangular lattice of holes with six rings of holes, a hole diameter of 3 μm, a hole-to-pitch ratio of 0.51, and a core diameter of approximately 8.5 μm. The second fibre had a diameter of 150 μm, was made entirely of PMMA, and contained six rings of 1.9 μm diameter holes with a hole-to-pitch ratio of 0.45, giving a core size of approximately 6.5 μm.

LPGs were inscribed in these fibres using a commercial engraving machine based on a CO_2 laser (DC-K40III, Liaocheng Shenhui Laser Equipement Co.). The resolution of the engraving laser was 30 μm which is adequate for point-by-point inscription of the LPGs, as the pitch is of the order of 1 mm. There are two ways how grating could be formed, one is by etching the fibre and the other one is by perturbing the microstructured region of the fibre:

Etching of the fibre:

Etching of the fibre is done by iterative laser inscription such that each inscription step melts and etches away a small portion of the fibre as shown in Figure 6-1. The method has a high risk of failure as etching should reach the microstructured region, enter it, but not damage the core of the fibre. Laser intensity had to be kept at low powers near lasing threshold. As the etching is dependent on the laser intensity, which was unstable, and the quality of the fibre, it was hard to get consistently good results. The grooves of the gratings were receiving different laser intensities so often parts of the grating would just etch into microstructured region or even cut through the core of the fibre, with the other grooves still not reaching the region,. The gratings which were made through this method were fragile due to deep grooves, and as such they were very sensitive to slightest bends.

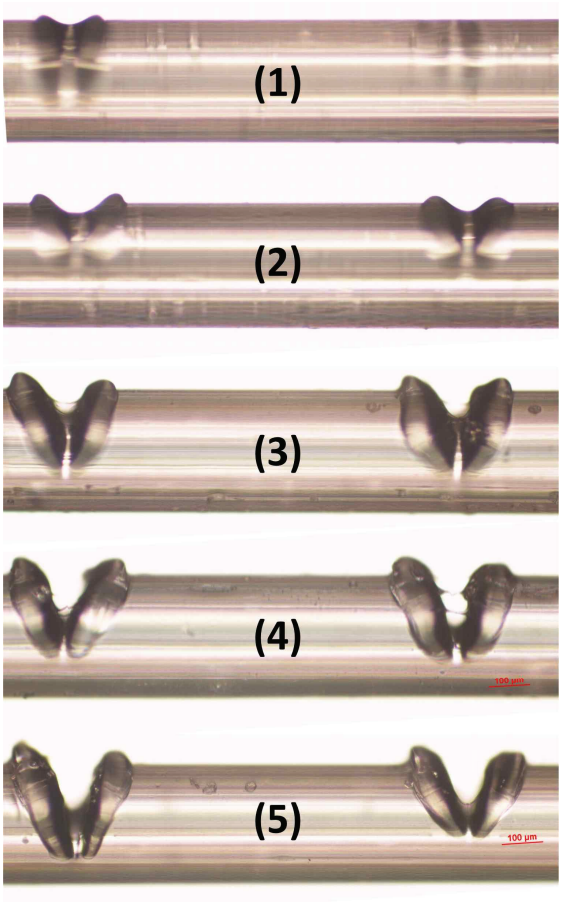

Figure 6-1. Images showing the formation of etched LPG. The numbers are showing number of laser inscription. Already after the cycle (1) the difference between two etched grooves is considerable. After the cycle (5) the fibre is very fragile due to deep groves of the grating.

Perturbing the microstructured region:

This requires heating of the fibre at the positions of the grating grooves, and it is done at lower intensities than the etching method. The complete formation of the grating is not clear, but as the surface effects were small and showing slight melting, we can suggest that the majority of the change is induced in the microstructured region, in addition to potential change in refractive index of the material. However, such refractive index change using a CO_2 wavelength at 9.4 or 10.6 µm has not been reported yet. The resulting grating was much more robust than the etched one so we continued with this method.

The laser was operated near threshold to avoid damaging the fibres from higher intensities, however, this resulted in power fluctuations and the exact power of the laser was not able to be measured. The effect of fluctuations on the grating inscription was minimized by averaging, by performing multiple inscriptions of the same grating whilst monitoring the spectrum of the fibre. The laser ablated the surface and heated the fibre to yield relatively uniform grooves, which over many repetitions formed the grating. Inscription was stopped once the grating had reached a suitable extinction ratio. Examples of the CO_2 laser-inscribed gratings, together with the central microstructured region of the larger fibre facet, are shown in Figure 6-2 (a) and (b).

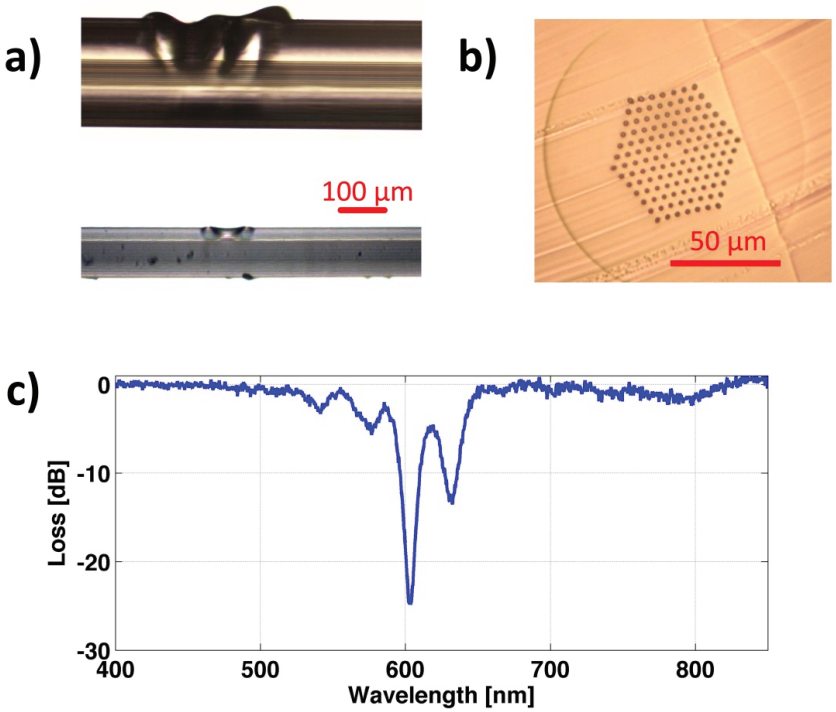

Figure 6-2. (a) Microscope images of the sides of the thicker (310 µm diameter) and thinner (150 µm diameter) fibres used in the experiment, showing parts of the fibre containing the groove comprising the LPG. (b) The central microstructured region of the thicker fibre. (c) Example spectrum of an LPG fabricated with the CO_2 laser in the thicker fibre. This spectrum shows a LPG dip of 25 dB at 603 nm, as well as a secondary 13 dB dip at 631 nm, attributed to the presence of a second core mode.

The gratings inscribed in this work had a pitch between 0.8 mm and 1 mm, giving transmission minima in the range of 590 nm to 670 nm where the fibre losses are lowest, as shown previously in work by Lwin *et al.* [68]. For a given fibre and pitch, the wavelength

repeatability of this technique was better than 10 nm, with variations attributed to the initial strain applied to the fibres prior to inscription, and the alignment between the angle of the fibre and the inscription direction of the engraving laser; precise control of the wavelength was not required in this work so it was not further investigated. Fabricated gratings had good extinction at the grating wavelength of up to 25 dB. An example grating spectrum is presented in Figure 6-2 (c).

6.2. LPG based all plastic endoscope

As the fibres and gratings are not intrinsically sensitive to pressure, a transducer is required to convert pressure to strain, in order for the strain to be detected and the pressure inferred. The transducer must be flexible to deform under pressure and sustain contractions and relaxations, and yet rigid enough to not be crushed. The transducer proposed here, shown in Figure 6-3, offers equal response from applied lateral forces (red arrows) while its shape ensures that applied pressure is converted into elongation (along the green arrows), and hence strain on the fibre. Such pods were made by 3D printing using an objet30 Pro printer and Rigid Opaque blue polymer (VeroBlue RGD840). The pod was 3 cm long in longitudinal direction and 1.5 cm wide at widest point.

As shown in Figure 6-3 (left), the sensing fibre would be pulled through holes in the pod's end-caps so that the LPG is positioned in the centre of the pod. Upon securing the pod-fibre connection, the pod would be wrapped in latex to make it air-tight, and to convert applied pressure from all lateral sides into a lateral force on the pod's arms, and hence into fibre strain.

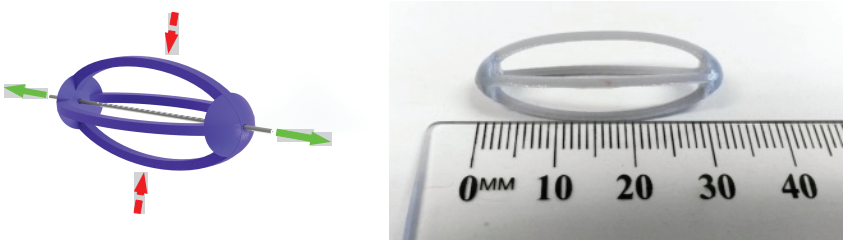

Figure 6-3. 3D model of the pod with a fibre containing LPG [left] and 3D printed pod [right]. The pod acts as a transducer transferring external pressure and force (red arrows) to fibre strain (green arrows). The LPG spectral feature changes with wavelength as the period of the LPG changes with strain.

6.3. Lateral testing of endoscope transducer

To test the effect of the pod as a transducer and also to test different methods of assembling the complete sensor, a fibre was secured in the pod using mechanical clamps and also two different glues. These three methods of securing the fibre to the pod were investigated by applying a force (weight) across two opposite arms. The applied force was monitored and the spectrum of the grating was recorded using an OceanOptics 2000+ spectrometer. Subsequently, the LPG peak was extracted through Matlab processing using a Centre of Gravity (COG) peak fitting method [141], as the spectra of different gratings/fibres had somewhat different shapes, the COG algorithm was optimised in each case.

The above test was carried out twice for each of the three assembly methods, with the force applied across either pair of arms of the pod. There was some variation in the results, attributed to uneven gluing and a slight deformation of the pod during cleaning (the 3D printing method used produces a pod embedded in resin, which must be cleaned). In each case below, the data from the more sensitive pair of arms is presented. A force up to 0.4 N (equivalent of 40 grams) was used, increasing from zero to the maximum and then decreasing again. The time between readings for different steps of the applied force was 20 s. This incorporated the time required to make a change in force, for the setup to stabilise and for the spectrum to be recorded. This analysis showed good regression of the sensor and no deformation of the pods arms.

6.3.1. Mechanical assembly of the transducer

The fibre was mechanically secured by inserting it inside rubber covers at the external edge of the pods and clamping it with wire. This prevented the fibre from slipping when the pod elongated, and translated elongation of the pod into strain on the fibre. The response to applied lateral force is presented in Figure 6-4, and show a small range of wavelength shift of about 1.5 nm. A hysteresis is also observed, quantified as a maximum uncertainty in the force that can be inferred from a wavelength reading, in this case the uncertainty is about 0.1 N.

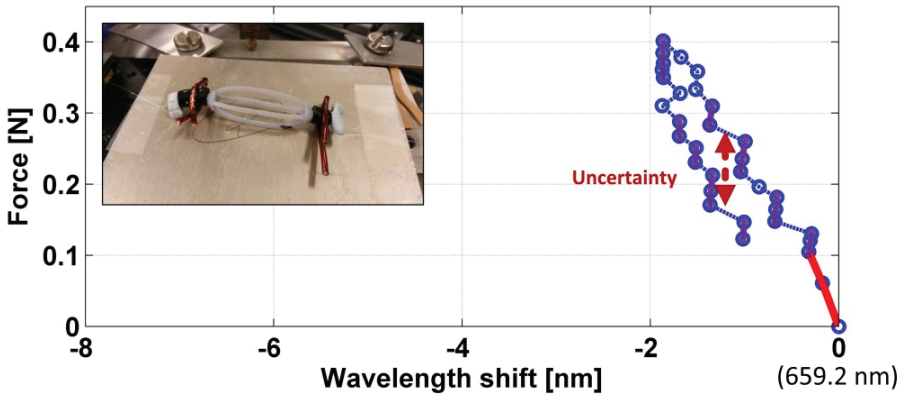

Figure 6-4. Sensor response to the lateral force across one pair of the pod's arms, with the fibre mechanically secured using rubber and wire clamps (see inset). The data reveals a problem of friction and slipping, in which there is no response to a change in force (corresponding to the purple data points). The grating wavelength with no force applied is shown in the brackets in the bottom right, and the red line indicates the beginning of the measurement.

The data in Figure 6-4. reveal a recurring problem with this mechanical assembly. In many instances when force was increased or decreased, the wavelength of the grating remained the same; these instances are highlighted using purple data points. This occurs due to friction between the mechanical clamps and the support of the pod as well as the weight of the clamps, which prevented the pod from elongating/retracting easily in response to small changes in applied force. Whilst this mechanical clamping could be easily disassembled, and would allow repeated testing of the same fibre, grating and/or pod, it was not pursued further.

6.3.2. Soluble polymer gluing of the transducer

To avoid the problems caused by the mechanical clamps, the fibre was glued directly to the pod at the ends. Initially, a glue formed by dissolving a cyclo-olefin polymer Zeonex 480R in cyclohexane was used. This created viscous glue which hardened as the solvent evaporated to give a slightly flexible join. The flexibility was able to absorb shock and protected the fibre from breaking. This approach would also allow the same pod and fibre to be used repeatedly as the glue could be removed with cyclohexane without affecting the fibre or pod.

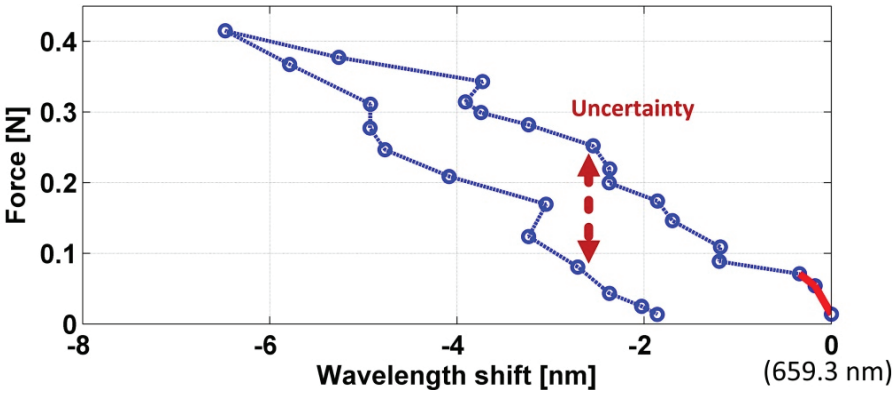

Figure 6-5. Sensor response to the lateral force across one pair of the pod's arms, with the fibre glued to the pod's caps with Zeonex 480R dissolved in cyclohexane. The response had a considerable uncertainty, of up to 0.17 N as indicated by the red dashed line. The grating wavelength with no force applied is shown in the brackets in the bottom right, and the red line indicates the beginning of the measurement.

A test fibre was glued to the pod using this method. A pre-strain of about 0.5 % was applied to the fibre inducing a shift in the grating wavelength from 664 nm to 659 nm, upon which it was glued and left to stiffen overnight. After this, the external strain was released and the fibre relaxed such that the peak shifted back to 662 nm. The fibre was then tested for its response to an applied force, which is shown in Figure 6-5. The maximum wavelength shift was 6.5 nm, more than four times larger than using the mechanical assembly for the same applied maximum force of 0.4 N.

The results of this test also showed a larger hysteresis, with a maximum uncertainty of approximately 0.17 N. This uncertainty is two times larger than observed with the mechanical assembly (Figure 6-4). The main reason for this hysteresis is that the glue does hot harden completely but remains highly viscous. It appears from these results that the timescale over which the glue deforms is larger than the timescale over which the measurement was conducted.

6.3.3. Cyanoacrylate glue (superglue)

The third approach in securing the fibre to the pod was cyanoacrylate glue (superglue). The advantage is rapid stiffening and strong adhesion to the PMMA fibre and pod; however the superglue could not be dissolved without damaging the fibre or pod, preventing repeated

experiments using the same samples. This glue also made the PMMA fibre brittle, and an additional layer of the more flexible Zeonex/cylcohexane glue was applied over the superglue as a protective layer. As the slipping (such as in the mechanical clamp holder) and viscosity (soluble glue) problems were not observed and the cyanoacrylate glue showed the best results, this arrangement was used in further studies into the effects of pre-strain and of the fibre diameter on the response of the sensor.

To investigate how pre-strain affects the response of the pod, we created two samples using the 310 μm diameter fibres but with different pre-strains. As shown in Figure 6-6, there was no appreciable difference between the two, neither in the maximum wavelength shift of about 3.9 nm, nor in the hysteresis uncertainty of 0.08 (0.14) N.

The above measurement was repeated with the 150 μm diameter fibres. The results are shown in Figure 6-7 and differ greatly from those of the thicker fibre of Figure 6-6.

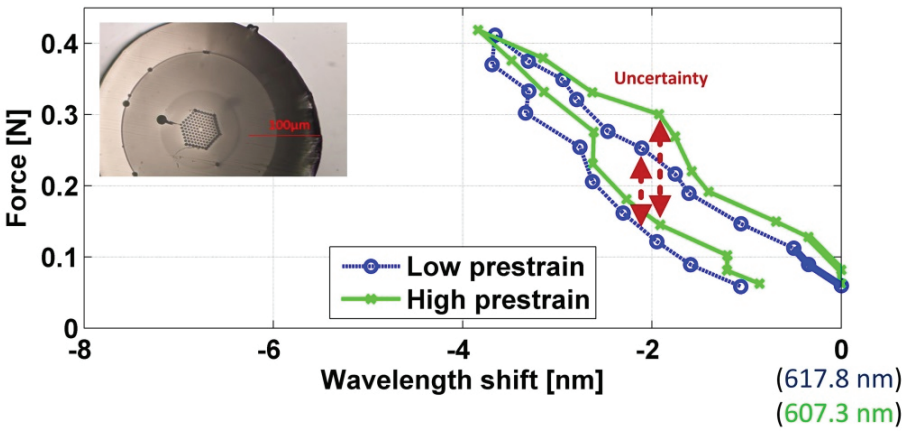

Figure 6-6. Sensor response using the 340 μm thick fibre, comparing high (~2.5%) and low (~0.5%) pre-strain. Both show a similar response with a maximum shift of 3.9 nm and an uncertainty of 0.08 N for the low pre-strain and 0.14 N for the high pre-strain. The grating wavelengths at the beginning of the measurement with 0.05 N force applied is shown in the brackets in the bottom right.

The maximum shift of the low pre-strain case was 7.5 nm while for the high pre-strain it was 4.2 nm, both larger than the thicker fibre. The uncertainty was 0.1 N for the low pre-strain and 0.14 N for high pre-strain.

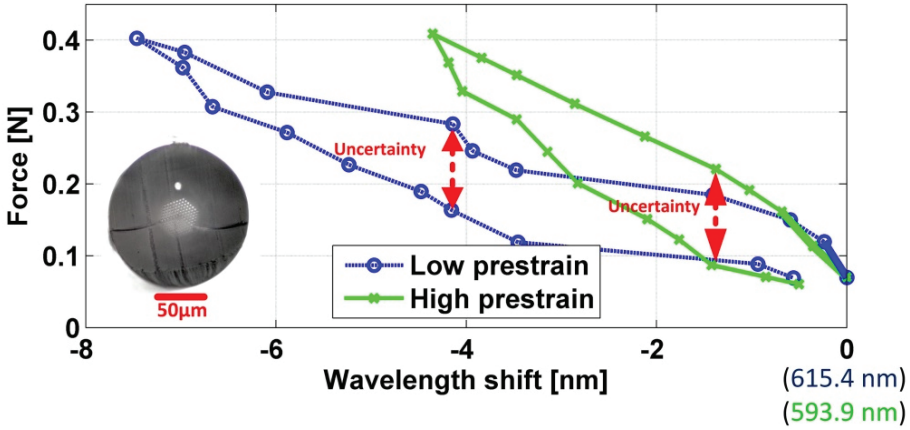

Figure 6-7. Sensor response using the 150 µm thick fibre and high (~2.5 %) and low (~0.5 %) prestrain. The low pre-strain has a larger maximum shift of 7.5 nm compared to 4.2 nm for the low pre-strain. The uncertainty is similar for both at 0.1 N for the low and 0.14 N for the high pre-strain. The grating wavelengths at the beginning of the measurement with 0.05 N force applied is shown in the brackets in the bottom right.

A comparison of the performance of the four sensors (2 diameters x 2 pre-strains) is summarised in Table 7. Comparison of the operation span, uncertainty and sensitivity of different fibres and prestrains. It is clear that the thinner fibre with low pre-strain is preferred as it gives a higher sensitivity than the other combinations. The thicker fibre and the higher pre-strain appear to be reinforcing the transducer pod, resulting in a smaller deformation for a given applied force. Hence, the fibre should have as little prestrain as possible to increase the sensitivity.

Table 7. Comparison of the operation span, uncertainty and sensitivity of different fibres and prestrains.

	Thick fibre		**Thin fibre**	
	High pre-strain	Low pre-strain	High pre-strain	Low pre-strain
Maximum shift at 0.4 N [nm]	3.9	3.9	4.2	7.5
Uncertainty [N]	0.08	0.14	0.1	0.12
Sensitivity [nm/N]	9.8	9.8	11	19

6.4. Pressure response of the transducer

Although the above results showed that a thin fibre with low pre-strain gives the highest sensitivity, due to difficult handling of the fragile thin-fibre pod, the characterisation of the pressure response was carried out on a sensor made of thick fibre under high pre-strain assembled using superglue, for ease of handling. The transducer was sealed with latex, which was glued to the four arms and the end of the pod using superglue, as shown in Figure 6-8. A thin coating of glue was applied to one arm of the pod, to which the latex was attached. The other arms received only a small amount of glue at their centre and the latex was wrapped around the pod and glued again along the whole length of the initial arm. Whilst this resulted in an uneven distribution of glue on the pod, it also minimized stiffening of the pod arms by the glue. Finally, excess latex was removed and the latex was glued to the caps of the pod with both superglue and Zeonex/cyclohexane for higher durability and flexibility of the joins, to protect the fibre.

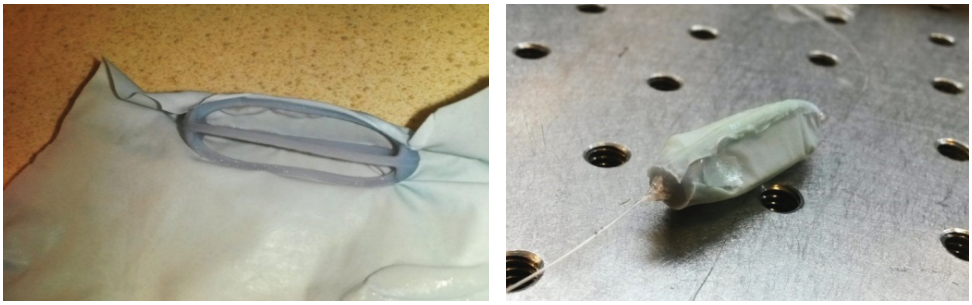

Figure 6-8. Wrapping of the transducer pod in latex cloth (left) and the complete pressure sensor (right)

The wrapped sensor was immersed in water to check for leaks, after which a slight negative pressure was applied to the interior of the pod using a needle and syringe, and the hole made by the needle was sealed with additional glue and latex; this patch is visible in Figure 6-8 (right). This initial negative pressure contributes to the pre-strain, but was not controlled.

The completed sensor was tested in a pressure chamber and the results are presented in Figure 6-9 Due to the limit of the pressure gauge used, the maximum pressure tested was 150 mBar. The grating wavelength was monitored and processed as in the previous

measurements and showed a steady response to the applied pressure, reaching a shift of 1.4 nm at 150 mBar, giving a response of 10.5 pm/mBar. The measurements were complicated by the pressure gauge's integration time, which was of the order of one second, and fluctuations in the pressure on shorter timescales. This effectively resulted in averaging, so the hysteresis observed in the force measurements was not observed in this case. The time in between taking each measurement was about 5 seconds. Multiple such measurements were repeated and yielded consistent results, such as presented in Figure 6-9. It should be noted that due to the method employed, the sensitivity is likely to have been decreased due to stiffening of the pods by the glue and latex, and also by the use of the thicker fibre.

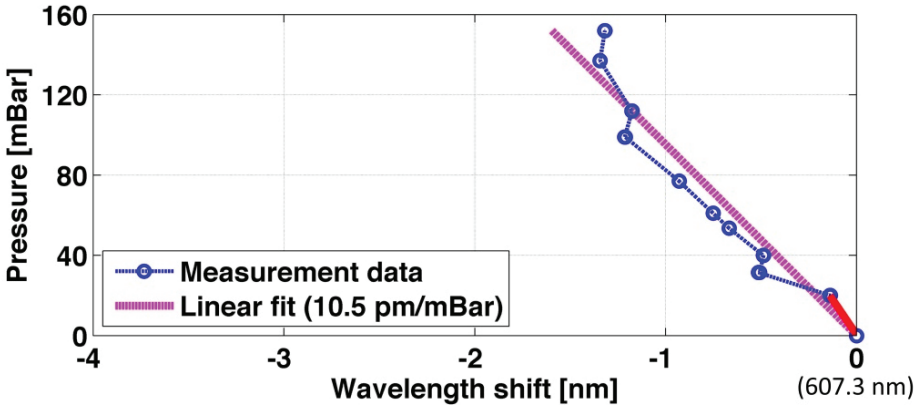

Figure 6-9. Pressure response of the sensor. Due to the pressure gauge's integration time, which was of the order of one second, and fluctuations in the pressure on shorter timescales, the hysteresis observed in the force measurements was not observed in this case. The deviation error from the fitted line was 12 mBar at its maximum.

6.5. Summary

In this Chapter an all polymer fibre-based pressure sensor is demonstrated, a sensor based on LPGs inscribed in PMMA mPOF fibre fixed in a 3D printed pressure-to-strain transducer. Initial analysis using a lateral force showed that a rigid connection between the fibre and transducer pod using superglue was required, and that thinner fibre with a low pre-strain gave the highest sensitivity by about a factor of 2 compared to other combinations of fibre thickness and pre-strain tested. The sensor's response to pressure was found to be 10.5 pm/mBar, noting that the sensitivity was reduced by the choice of fibre and the construction of the sensor. Further optimisation is expected to increase this sensitivity considerably through the use of a thinner fibre and lower pre-strain, and improvements in the pod design and sensor assembly.

When measuring the force applied on pods arms, the errors are mostly coming from the friction between the mechanical clamps and the support of the pod. In addition to that, the reading of the LPG shift value was taking place about 20 seconds after the new force was applied. Taking into account that the pod was made from plastic, a viscoelastic material, that was also contributing to the error in pressure sensing. Concerning improvements of the technology and the pod design, this pressure sensor could be implemented also with Fibre Bragg Grating technology, in which case only one end of the fibre would needed to be controlled. The pod as such could be optimised in terms of arm curvature, arm thickness and type of plastic which is used.

To refer back to the potential application of in-vivo pressure sensing which motivated this work, previous reports of silica FBG-based pressure sensors reported an approximately 0.9 pm/mBar sensitivity [140]*, which is an order of magnitude lower than the presented results. The difference is attributed to the pressure-to-strain conversion. The (unoptimised) sensor examined in this work gave a pressure-to-strain conversion of 0.95 %strain/Bar, whilst the silica FBG equivalent gave 0.075 %strain/Bar* [140,142]*. The response of the gratings to strain was similar in both cases (12 nm/%strain for the silica FBG* [142] *11 nm/%strain for the polymer LPG* [143]*). The significantly lower Young's modulus of the polymer compared to*

silica (3.2 GPa compared to 72 GPa) could be contributing to this difference in the effect of the transducer.

A final comparison should be made with reports of fibre-based pressure sensing which uses neither gratings nor a transducer [144–146]. *Such sensing schemes rely on pressure changing the phase velocity of light propagating in the fibres, or the birefringence of the fibres, and hence the output phase or polarisation. The pressure range over which such sensors have been demonstrated ranges from several Bar to several hundred Bar, hence they are not applicable to the 100 mBar range considered in this work.*

The all-plastic sensors considered in this work offer a means to measure pressures in the 150 mBar range as required for in vivo applications with an order of magnitude higher sensitivity compared to previous reports. The hysteresis, although introducing a degree of error, could be compensated for by recording the history of changes in the signal as we showed in Chapter 4. Implementation of a complete pressure sensing system would require the inscription of several LPGs on the same fibre with different wavelengths, a reinforcing structure around the fibre and further development and optimisation of the transducer pods and sensor assembly.

Chapter

7

Conclusion and Outlook

Since the first demonstration of FBG inscription in polymer fibre in 1999, and even more after first inscription in microstructured polymer fibre in 2004, the development of POFBG has advanced towards the technology which is almost ready for wide-scale commercialisation. Polymer fibres hold several advantages over their silica counterparts which makes them interesting for certain applications, especially in sensing.

In this thesis the focus was development of FBG technology in polymer fibres made from PMMA. It was demonstrated that, with phase-mask technique, formation of gratings is strongly dependent on alignment and the power of the laser. Alignment of the inscription setup is a not a straightforward task as micron precision cannot be visually inspected and adjusted for all degrees of alignment. Through precise construction of the setup and mirror, fabricated from the same piece of glass like phase mask, it is possible to minimise the number of unknowns which could influence inscription. The grating formation is also shown to be occurring in 3 stages. The first stage is “invisible” formation where the change of the refractive index induced by the laser light through phase mask is too small for our instrumentation to pick, the reflected peak is below the noise floor of the system. The growth stage of grating is happening in third and fourth stage, where second stage takes smaller amount and is characterised by slow growth of gratings reflectivity. The third stage is characterised by faster growth of grating reflectivity and it finishes as the growth decreases to zero. The second and third stage are not always distinguishable but for the tracked grating formations, at least half of them shown to have them both.

The formation of gratings inside microstructured fibres is greatly dependent on orientation of the cladding microstructure to the inscription beam. We have statistically shown that gratings inscribed at angles which had direct openings to the laser light showed fastest inscriptions and

highest reflectivity. Gratings which were inscribed at the angles which had air-holes of microstructured cladding hindering the incoming light showed weak growth and reflectivity, or non at all. Holes of the microstructured cladding scatter all the light so grating cannot form in the core of the fibre.

As polymers are viscoelastic materials, they have properties of both viscous and elastic materials. The exact behaviour of polymer (PMMA) fibres, which are made under special drawing conditions, is also different to a bulk polymer. Chapter 4 is focusing on a long-term strain behaviour of a free-standing, unembedded FBG fibre sensors. It showed that after straining polymer fibre sensor at certain strain level, the relaxation of the fibre happens in two phases defining two wavelength ranges. Two ranges are called fast relaxation range ($\Delta\Lambda_{fast}$) and slow relaxation range ($\Delta\Lambda_{slow}$). $\Delta\Lambda_{fast}$ is the part with higher strains and in this range fibre behaves generally elastically – it responds instantaneously to the changes in the applied strain. The $\Delta\Lambda_{slow}$ is the wavelength range at lower strain levels, near the complete relaxation of the fibre, and the fibre is behaving generally viscously. Fibre sensor operating in it cannot relax fast and it experiences a time lag. The amount that these two ranges take of the total strain range depends on four factors: strain amount, strain duration, relaxation duration and the number of cycles that sensor was strained and relaxed.
Their dependency is reciprocal - as one increases other one shrinks: the $\Delta\Lambda_{slow}$ increases with strain amount, strain duration and increasing number of cycles; $\Delta\Lambda_{fast}$ increases with relaxation duration.

For strains up to 0.9%, it appears that the $\Delta\Lambda_{slow}$ never increases for more than 35% of the whole strain range, meaning that the useful, fast relaxing $\Delta\Lambda_{fast}$ range takes up to 65% of the strain range. Further increase in $\Delta\Lambda_{slow}$ due to cyclic straining and relaxing seems to reach an equilibrium value, suggesting that $\Delta\Lambda_{slow}$ would never cover the whole strain range.
When increasing the strain to 4.9% the relative amount of $\Delta\Lambda_{slow}$ grows with respect to $\Delta\Lambda_{fast}$, but so does the absolute amount of $\Delta\Lambda_{fast}$. The increase in absolute amount of $\Delta\Lambda_{fast}$ from 4-5% is almost negligible which is most probably due to yield strain, the limit of quasi-elastic behaviour, which is around 6%. As an overall conclusion, with proper prestrain covering

$\Delta\Lambda_{slow}$, the free standing FBG fibre sensor could operate in "real-time" entirely in $\Delta\Lambda_{fast}$. It would have the highest sensing range around 3%.

The 5th Chapter, the last one dealing with FBGs, is focusing on acoustic sensing. It was demonstrated that strong FBG of 28 dBs in reflection, in etched fibre tip of 60 μm in diameter, is capable of picking up sound levels of 70-95 dBs. These sound levels are equivalent to sound of a TV, to a sound of a motorcycle. A simple microphone membrane attached to the tip of the fibre showed to increase the sensitivity of the the FBG, but it does it in a narrow region and it does it very nonlinearly.

Chapter 6 is focusing on LPGs, their fabrication with high power CO_2 laser in mPOF fibres and use as a medical endoscope. It was shown that LPGs can be fabricated in two was using CO_2 laser: one way is etching – which produces fairly fragile gratings, and the other one is by perturbation of the microstructured region. The latter mechanism is not completely understood as it there was no clear formula as in when the grating was formed and when not. Both methods could produce good quality gratings with high extinction ratios. For certain human colonic problems there are no suitable endoscopes. A plastic endoscope which could measure distributed changes in pressure throughout the colon would be a great help to accurately discriminate certain colonic illnesses. We tried to tackle that need with LPG based endoscope. The LPGs were produced in fibres of different thickness and over them a pod-like transducer was glued. The Pod acted as a lateral to longitudinal force transducer, effectively straining the fibre when the force was applied to its sides. The pod was wrapped with latex cloth to seal off all the holes and to make it a pressure to strain transducer. The wrapped pod transducer in combination with LPG was then tested in a pressure chamber showing good results for tested ranges to 150 mBars.

The final endoscope should be able to sense pressures of up to 250 mBars and should have several pods on the same fibre. The additional improvements to this endoscope would include switching from LPG to FBG, as FBGs require only one side as input/output of the system.

The future of POFBG technology is certainly bright, with a wide spectra of new applications being published in scientific journals and demonstrated at technical conferences around the world each year. The low cost of production and material are the main driving factors, but problems still exist with fast inscription of FBGs with good quality. However, recent improvements pushed the speed of inscription down to the range of several seconds giving hope that soon gratings will be written on a drawing tower, the way they can with silica fibres.

Appendix A

AP

List of Abbreviations

BDK - benzyl dimethyl ketal

CH bond- Carbon Hydrogen bond

CW Laser- Continuous Wave Laser

EM - Electro-magnetic

EMI - Electro-magnetic Interference

FBG – Fibre Bragg Grating

FWHM – Full Width at Half Maximum

HeCd – Helium Cadmium

LPG – Long Period Grating

mPOF - Microstructured Polymer Optical Fibre

NA - Numerical Aperture

PCF – Photonic Crystal Fibre

PMMA – Polymethyl Methacrylate

POF - Polymer Optical Fibre

POFBG - Polymer Optical Fibre Fibre Bragg Grating

RH – Relative Humidity

TIR - Total Internal Reflection

UV- Ultraviolet

References

R

1. A. D. Kersey, "A Review of Recent Developments in Fiber Optic Sensor Technology," Opt. Fiber Technol. **2**, 291–317 (1996).
2. M. van Eijkelenborg, M. Large, a Argyros, J. Zagari, S. Manos, N. Issa, I. Bassett, S. Fleming, R. McPhedran, C. M. de Sterke, and N. a Nicorovici, "Microstructured polymer optical fibre.," Opt. Express **9**, 319–327 (2001).
3. M. Large, G. W. Barton, L. Poladian, and M. A. van Eijkelenborg, *Microstructured Polymer Optical Fibre*, 1st ed. (Springer, 2008).
4. R. C. Lasky, U. L. Oesterberg, and D. P. Stigliani, *Optoelectronics for Data Communication* (Academic Press, 1995).
5. N. Tanio and Y. Koike, "What is the most transparent polymer?," Polym. J. **32**, 43–50 (2000).
6. Y. Koike and M. Asai, "The future of plastic optical fiber," NPG Asia Mater. **1**, 22–28 (2009).
7. A. Cusano, D. Paladino, A. Cutolo, A. Iadicicco, and S. Campopiano, *Fiber Bragg Grating Sensors: Recent Advancements, Industrial Applications and Market Exploitation* (BENTHAM SCIENCE PUBLISHERS, 2012).
8. K. Peters, "Polymer optical fiber sensors—a review," Smart Mater. Struct. **20**, 13002 (2011).
9. E. F. Schubert, *Light Emitting Diodes* (Cambridge University Press, 2006).
10. K. Welikow, P. Gdula, P. Szczepański, R. Buczyński, and R. Piramidowicz, "Microstructured plastic optical fibers for applications in FTTH systems," in *Microstructured and Specialty Optical Fibres*, K. Kalli and A. Mendez, eds. (2012), Vol. 13, p. 84261A.
11. C. M. DeCusatis and C. J. S. DeCusatis, *Fiber Optic Essentials* (Elsevier, 2006).
12. R. Kashyap, *Fiber Bragg Gratings*, second edi (Elsevier, 2010).
13. J. Zubia and J. Arrue, "Plastic Optical Fibers: An Introduction to Their Technological Processes and Applications," Opt. Fiber Technol. **7**, 101–140 (2001).
14. D. J. Webb, "Fibre Bragg grating sensors in polymer optical fibres," Meas. Sci. Technol. **26**, 92004 (2015).
15. A. Dupuis, N. Guo, Y. Gao, N. Godbout, S. Lacroix, C. Dubois, and M. Skorobogatiy, "Prospective for biodegradable microstructured optical fibers.," Opt. Lett. **32**, 109–111 (2007).
16. S. H. Law, M. A. van Eijkelenborg, G. W. Barton, C. Yan, R. Lwin, and J. Gan, "Cleaved end-face quality of microstructured polymer optical fibres," Opt. Commun. **265**, 513–520 (2006).
17. S. H. Law, J. D. Harvey, R. J. Kruhlak, M. Song, E. Wu, G. W. Barton, M. A. Van Eijkelenborg, and M. C. J. Large, "Cleaving of microstructured polymer optical fibres," Opt. Commun. **258**, 193–202 (2006).
18. A. Stefani, S. Andresen, W. Yuan, and O. Bang, "Dynamic characterization of polymer optical fibers," IEEE Sens. J. **12**, 3047–3053 (2012).
19. C. Jiang, M. G. Kuzyk, J.-L. Ding, W. E. Johns, and D. J. Welker, "Fabrication and mechanical behavior of dye-doped polymer optical fiber," J. Appl. Phys. **92**, 4 (2002).
20. T. a Birks, J. C. Knight, P. S. Russell, and D. M. Atkin, "All-silica single-mode optical fiber with photonic crystal cladding," Opt. Lett. **21**, 1547–1549 (1996).

21. N. A. Mortensen, "Semianalytical approach to short-wavelength dispersion and modal properties of photonic crystal fibers.," Opt. Lett. **30**, 1455–1457 (2005).

22. M. A. Van Eijkelenborg, A. Argyros, G. Barton, I. M. Bassett, M. Fellew, G. Henry, N. A. Issa, M. C. J. Large, S. Manos, W. Padden, L. Poladian, and J. Zagari, "Recent progress in microstructured polymer optical fibre fabrication and characterisation," Opt. Fiber Technol. **9**, 199–209 (2003).

23. A. Argyros, M. a van Eijkelenborg, M. C. J. Large, and I. M. Bassett, "Hollow-core microstructured polymer optical fiber.," Opt. Lett. **31**, 172–174 (2006).

24. M. K. Szczurowski, O. Frazão, J. M. Baptista, K. Nielsen, O. Bang, and W. Urbańczyk, "Sensing characteristics of birefringent microstructured polymer optical fiber," in *21st International Conference on Optical Fiber Sensors* (2011), Vol. 7753, p. 77533Z.

25. M. C. J. Large, A. Argyros, F. Cox, M. A. van Eijkelenborg, S. Ponrathnam, N. S. Pujari, I. M. Bassett, R. Lwin, and G. W. Barton, "Microstructured polymer optical fibres: new opportunities and challenges," Mol. Cryst. Liq. Cryst. **446**, 219–231 (2006).

26. R. Lwin, G. Barton, L. Harvey, J. Harvey, D. Hirst, S. Manos, M. C. J. Large, L. Poladian, A. Bachmann, H. Poisel, and K. F. Klein, "Beyond the bandwidth-length product: Graded index microstructured polymer optical fiber," Appl. Phys. Lett. **91**, 1–4 (2007).

27. G. E. Town, R. M. Chaplin, M. J. Wimford, and D. Baer, "Randomly microstructured polymer optical fibre," ACOFT/AOS 2006 - Aust. Conf. Opt. Fibre Technol. Opt. Soc. 102–103 (2006).

28. G. Emiliyanov, J. B. Jensen, O. Bang, P. E. Hoiby, L. H. Pedersen, E. M. Kjaer, and L. Lindvold, "Localized biosensing with Topas microstructured polymer optical fiber.," Opt. Lett. **32**, 460–2 (2007).

29. W. Yuan, L. Khan, D. J. Webb, K. Kalli, H. K. Rasmussen, A. Stefani, and O. Bang, "Humidity insensitive TOPAS polymer fiber Bragg grating sensor," Opt. Express **19**, 19731–19739 (2011).

30. C. Markos, A. Stefani, K. Nielsen, H. K. Rasmussen, W. Yuan, and O. Bang, "High-Tg TOPAS microstructured polymer optical fiber for fiber Bragg grating strain sensing at 110 degrees," Opt. Express **21**, 4758–65 (2013).

31. A. Stefani, K. Nielsen, H. K. Rasmussen, and O. Bang, "Cleaving of TOPAS and PMMA microstructured polymer optical fibers: Core-shift and statistical quality optimization," Opt. Commun. **285**, 1825–1833 (2012).

32. M. A. Van Eijkelenborg, A. Argyros, and S. G. Leon-saval, "Polycarbonate hollow-core microstructured optical fiber," **33**, 2446–2448 (2008).

33. A. D. Kersey, M. A. Davis, H. J. Patrick, M. LeBlanc, K. P. Koo, C. G. Askins, M. A. Putnam, and E. J. Friebele, "Fiber grating sensors," J. Light. Technol. **15**, 1442–1463 (1997).

34. K. O. Hill and G. Meltz, "Fiber Bragg grating technology fundamentals and overview," J. Light. Technol. **15**, 1263–1276 (1997).

35. K. O. Hill, Y. Fujii, D. C. Johnson, and B. S. Kawasaki, "Photosensitivity in optical fiber waveguides: Application to reflection filter fabrication," Appl. Phys. Lett. **32**, 647–649 (1978).

36. I.-L. Bundalo, K. Nielsen, C. Markos, and O. Bang, "Bragg grating writing in PMMA microstructured polymer optical fibers in less than 7 minutes," Opt. Express **22**, 5270–6 (2014).

37. J. Canning, "Fibre gratings and devices for sensors and lasers," Laser Photonics Rev. **2**, 275–289 (2008).

38. A. Martinez, M. Dubov, I. Khrushchev, and I. Bennion, "Direct writing of fibre Bragg gratings by femtosecond laser," Electron. Lett. **40**, 1170 (2004).

39. A. Stefani, M. Stecher, G. Town, and O. Bang, "Direct writing of fiber Bragg grating in

microstructured polymer optical fiber," IEEE Photonics Technol. Lett. **24**, 1148–1150 (2012).

40. A. Othonos, "Fiber Bragg gratings," Rev. Sci. Instrum. **68**, 4309 (1997).

41. W. J. Tomlinson, "Photoinduced refractive index increase in Poly(Methylmethacrylate) and its applications," Appl. Phys. Lett. **16**, 486 (1970).

42. Z. Xiong, G. D. Peng, B. Wu, and P. L. Chu, "Highly tunable Bragg gratings in single-mode polymer optical fibers," IEEE Photonics Technol. Lett. **11**, 352–354 (1999).

43. C. Wochnowski, S. Metev, and G. Sepold, "UV-laser-assisted modification of the optical properties of polymethylmethacrylate," Appl. Surf. Sci. **154**, 706–711 (2000).

44. D. Sáez-Rodríguez, K. Nielsen, O. Bang, and D. J. Webb, "Photosensitivity mechanism of undoped poly(methyl methacrylate) under UV radiation at 325 nm and its spatial resolution limit," Opt. Lett. **39**, 3421–3424 (2014).

45. A. Stefani, C. Markos, and O. Bang, "Narrow bandwidth 850-nm fiber bragg gratings in few-mode polymer optical fibers," IEEE Photonics Technol. Lett. **23**, 660–662 (2011).

46. D. Sáez-Rodríguez, K. Nielsen, O. Bang, and D. J. Webb, "Time-dependent variation of fiber Bragg grating reflectivity in PMMA-based polymer optical fibers," Opt. Lett. **40**, 1476 (2015).

47. G. D. Marshall, D. J. Kan, A. A. Asatryan, L. C. Botten, and M. J. Withford, "Transverse coupling to the core of a photonic crystal fiber: the photo-inscription of gratings," Opt. Express **15**, 7876–7887 (2007).

48. I.-L. Bundalo, K. Nielsen, and O. Bang, "Angle dependent Fiber Bragg grating inscription in microstructured polymer optical fibers," Opt. Express **23**, 3699 (2015).

49. B. J. Eggleton, P. S. Westbrook, R. S. Windeler, S. Spälter, and T. a Strasser, "Grating resonances in air–silica microstructured optical fibers," Opt. Lett. **24**, 1460 (1999).

50. R. Oliveira, L. Bilro, and R. Nogueira, "Bragg gratings in a few mode microstructured polymer optical fiber in less than 30 seconds," Opt. Express **23**, 10181 (2015).

51. Y. Luo, Q. Zhang, H. Liu, and G.-D. Peng, "Gratings fabrication in benzildimethylketal doped photosensitive polymer optical fibers using 355 nm nanosecond pulsed laser," Opt. Lett. **35**, 751 (2010).

52. H. Dobb, D. J. Webb, K. Kalli, A. Argyros, M. C. J. Large, and M. A. van Eijkelenborg, "Continuous wave ultraviolet light-induced fiber Bragg gratings in few- and single-mode microstructured polymer optical fibers," Opt. Lett. **30**, 3296–3298 (2005).

53. F. Berghmans, T. Geernaert, T. Baghdasaryan, and H. Thienpont, "Challenges in the fabrication of fibre Bragg gratings in silica and polymer microstructured optical fibres," Laser Photon. Rev. **8**, 27–52 (2014).

54. K. Kalli, H. L. Dobb, D. J. Webb, K. Carroll, C. Themistos, M. Komodromos, G.-D. Peng, Q. Fang, and I. . W. Boyd, "Development of an electrically tuneable Bragg grating filter in polymer optical fibre operating at 1.55 μm," Meas. Sci. Technol. **18**, 3155–3164 (2007).

55. A. Argyros, "Bragg Reflection and Bandgaps in Microstructured Optical Fibres," University of Sydney (2006).

56. Y. Jin and A. M Granville, "Polymer Fiber Optic Sensors – A Mini Review of their Synthesis and Applications," J. Biosens. Bioelectron. **7**, 1–11 (2016).

57. C. Silva, J. Coelho, P. Caldas, and P. Jorge, "Fibre Sensing System Based on Long-Period Gratings for Monitoring Aqueous Environments," Fiber Opt. Sensors 317–342 (2012).

58. J. Witt, M. Steffen, M. Schukar, and K. Krebber, "Investigation of sensing properties of long period gratings based on microstructured polymer optical fibres," in *Proceedings of SPIE-The International Society for Optical Engineering*, J. L. Santos, B. Culshaw, J. M. López-Higuera, and W. N. MacPherson, eds. (2010), Vol. 7714, p. 76530I.

59. M. A. Van Eijkelenborg, W. Padden, and J. A. Besley, "Mechanically induced long-period gratings in microstructured polymer fibre," Opt. Commun. **236**, 75–78 (2004).

60. B. Eggleton, C. Kerbage, P. Westbrook, R. Windeler, and A. Hale, "Microstructured optical fiber devices," Opt. Express **9**, 698 (2001).

61. G. Humbert, A. Malki, S. Février, P. Roy, and D. Pagnoux, "Electric arc-induced long-period gratings in Ge-free air-silica microstructure fibres," Electron. Lett. **39**, 349 (2003).

62. G. Kakarantzas, T. a Birks, and P. S. J. Russell, "Structural long-period gratings in photonic crystal fibers.," Opt. Lett. **27**, 1013–1015 (2002).

63. J. M. P. Coelho, C. Silva, M. Nespereira, M. Abreu, and J. Rebordão, "Writing of Long Period Fiber Gratings Using CO 2 Laser Radiation," Adv. Opt. Fiber Technol. Fundam. Opt. Phenom. Appl. (2015).

64. D. Sáez-rodríguez, J. L. C. Munoz, I. Johnson, D. J. Webb, and M. C. J, "Long period fibre gratings photoinscribed in a microstructured polymer optical fibre by UV radiation," **7357**, 1–8 (2009).

65. a Diez, T. a Birks, W. H. Reeves, B. J. Mangan, and P. S. J. Russell, "Excitation of cladding modes in photonic crystal fibers by flexural acoustic waves," Opt. Lett. **25**, 1499 (2000).

66. J. H. Lim, K. S. Lee, J. C. Kim, and B. H. Lee, "Tunable fiber gratings fabricated in photonic crystal fiber by use of mechanical pressure.," Opt. Lett. **29**, 331–333 (2004).

67. M. P. Hiscocks, M. a van Eijkelenborg, a Argyros, and M. C. J. Large, "Stable imprinting of long-period gratings in microstructured polymer optical fibre.," Opt. Express **14**, 4644–4649 (2006).

68. R. Lwin, A. Argyros, S. G. Leon-Saval, and M. C. J. Large, "Strain sensing using long period gratings in microstructured polymer optical fibres," Ofs-2011 **7753**, 775394–775396 (2011).

69. Z. Li, H. Y. Tam, L. Xu, and Q. Zhang, "Fabrication of long-period gratings in poly(methyl methacrylate-co-methyl vinyl ketone-co-benzyl methacrylate)-core polymer optical fiber by use of a mercury lamp.," Opt. Lett. **30**, 1117–1119 (2005).

70. G. Rajan and K. Iniewski, *Optical Fiber Sensors Advanced Techniques and Applications* (2015).

71. A. Grillet, D. Kinet, J. Witt, M. Schukar, K. Krebber, F. Pirotte, and A. Depr??, "Optical fiber sensors embedded into medical textiles for healthcare monitoring," IEEE Sens. J. **8**, 1215–1222 (2008).

72. K. Krebber, S. Liehr, and J. Witt, "Smart technical textiles based on fibre optic sensors," in *OFS2012 22nd International Conference on Optical Fiber Sensors, Invited Paper*, Y. Liao, W. Jin, D. D. Sampson, R. Yamauchi, Y. Chung, K. Nakamura, and Y. Rao, eds. (2012), Vol. 8421, p. 84212A–10.

73. S. Yin, P. B. Ruffin, and F. T. S. Yu, *Fiber Optic Sensors*, 2nd ed. (CRC Press, 2008).

74. K. Peters, "Polymer optical fiber sensors—a review," Smart Mater. Struct. **20**, 13002 (2011).

75. S. K. Aulakh, "Applications of Optical Fibers in Automobiles," http://www.ijser.org/paper/Applications-of-Optical-Fibers-in-Automobiles.html.

76. R. J. Bartlett, R. Philip-Chandy, P. Eldridge, D. F. Merchant, R. Morgan, and P. J. Scully, "Plastic optical fibre sensors and devices," Trans. Inst. Meas. Control **22**, 431–457 (2000).

77. D. Gallego and H. Lamela, "High sensitivity interferometric polymer optical fiber ultrasound sensors for optoacoustic imaging and biomedical application," in *Library* (2011), Vol. 7753, p. 775370.

78. D. Gallego and H. Lamela, "Optoacoustic fiber optic interferometric sensors for biomedical applications," in *Sensors (Peterborough, NH)*, S. J. Mihailov, H. H. Du, and G. Pickrell, eds.

(2011), Vol. 8028, p. 80280O.

79. M. Silva-López, A. Fender, W. N. MacPherson, J. S. Barton, J. D. C. Jones, D. Zhao, H. Dobb, D. J. Webb, L. Zhang, and I. Bennion, "Strain and temperature sensitivity of a single-mode polymer optical fiber," Opt. Lett. **30**, 3129 (2005).

80. et al Omid Abdi, "Validation of a single-mode polymer optical fiber sensor and interrogator for large strain measurements," Meas. Sci. Technol. **22**, 75207 (2011).

81. S. Kiesel, K. Peters, T. Hassan, and M. Kowalsky, "Large Deformation In-Fiber Polymer Optical Fiber Sensor," **20**, 2008–2010 (2008).

82. C. M. B. Cordeiro, M. A. R. Franco, G. Chesini, E. C. S. Barretto, R. Lwin, C. H. Brito Cruz, and M. C. J. Large, "Microstructured-core optical fibre for evanescent sensing applications," Opt. Express **14**, 13056 (2006).

83. A. Wang, A. Docherty, B. T. Kuhlmey, F. M. Cox, and M. C. J. Large, "Side-hole fiber sensor based on surface plasmon resonance," Opt. Lett. **34**, 3890 (2009).

84. J. B. Jensen, P. E. Hoiby, G. Emiliyanov, O. Bang, L. H. Pedersen, and A. Bjarklev, "Selective detection of antibodies in microstructured polymer optical fibers," Opt. Express **13**, 5883 (2005).

85. J. Wojcik, P. Mergo, J. Klimek, G. WÄ‡jcik, K. Skorupski, J. PÄ™dzisz, and J. KopeÄ‡, "Technology of high birefringent microstructured polymer optical fibers," Photonics Lett. Pol. **2**, 4–6 (2010).

86. X. Yu, K. S. Lok, Y. C. Kwok, Y. Zhang, H. Wei, and W. Tong, "Chemiluminescence detection in liquid-core microstructured optical fibers," Sensors Actuators B Chem. **160**, 800–803 (2011).

87. F. M. Cox, A. Argyros, and M. C. J. Large, "Liquid-filled hollow core microstructured polymer optical fiber," Opt. Express **14**, 4135 (2006).

88. L. Peng, X. Yang, L. Yuan, L. Wang, E. Zhao, F. Tian, and Y. Liu, "Gaseous ammonia fluorescence probe based on cellulose acetate modified microstructured optical fiber," Opt. Commun. **284**, 4810–4814 (2011).

89. J. Wang and L. Wang, "Carbon dioxide gas sensor derived from a 547-hole microstructured polymer optical fiber preform," Opt. Lett. **35**, 3270 (2010).

90. F. M. Cox, A. Argyros, M. C. J. Large, and S. Kalluri, "Surface enhanced Raman scattering in a hollow core microstructured optical fiber," Opt. Express **15**, 13675 (2007).

91. M. C. J. Large, D. Blacket, and C. A. Bunge, "Microstructured polymer optical fibers compared to conventional POF: Novel properties and applications," IEEE Sens. J. **10**, 1213–1217 (2010).

92. X. H. Yang and L. L. Wang, "Fluorescence pH probe based on microstructured polymer optical fiber," Opt. Express **15**, 16478 (2007).

93. Y. Rao, "In-fibre Bragg grating sensors," Technology **8**, 355–375 (1997).

94. A. D. Kersey, M. a. Davis, H. J. Patrick, M. LeBlanc, K. P. Koo, C. G. Askins, M. a. Putnam, and E. J. Friebele, "Fiber grating sensors," J. Light. Technol. **15**, 1442–1463 (1997).

95. J. Renoirt, C. Caucheteur, M. Olivier, P. Mégret, and M. Debliquy, "Infrared Radiation Detection Using Fiber Bragg Grating," in *Infrared Radiation*, D. V. Morozhenko, ed. (InTech Europe, 2012).

96. F. M. Haran, J. K. Rew, and P. D. Foote, "A strain-isolated fibre Bragg grating sensor for temperature compensation of fibre Bragg grating strain sensors," Meas. Sci. Technol. **9**, 1163–1166 (1998).

97. C. Zhang, W. Zhang, D. J. Webb, and G.-D. Peng, "Optical fibre temperature and humidity

sensor," Electron. Lett. **46**, 643 (2010).

98. X. F. Chen, C. Zhang, D. J. Webb, G.-D. Peng, and K. Kalli, "Bragg grating in polymer optical fibre for strain, bend and temperature sensing," Meas. Sci. Technol. **21**, 94005 (2010).

99. H. . Liu, H. . Liu, G. . Peng, and P. . Chu, "Strain and temperature sensor using a combination of polymer and silica fibre Bragg gratings," Opt. Commun. **219**, 139–142 (2003).

100. K. Krebber, P. Lenke, S. Liehr, N. Noether, M. Wendt, and A. Wosniok, "Distributed fiber optic sensors embedded in technical textiles for structural health monitoring," in *Fourth European Workshop on Optical Fibre Sensors*, J. L. Santos, B. Culshaw, J. M. López-Higuera, and W. N. MacPherson, eds. (2010), Vol. 7653, p. 76530A–76530A–12.

101. J.Witt, M. Schukar, K. Krebber, J. Demuth, and L. Sasek, "Fiber optic heart rate sensor for integration into personal protective equipment," in *Proceedings of the International Conference on Plastic Optical Fibres,* (2011), pp. 573–577.

102. D. J. Webb, H. Dobb, K. E. Carroll, K. Kalli, M. Aressy, S. Kukureka, A. Argyros, M. C. Large, and M. A. van Eijkelenborg, "Fibre Bragg Gratings Recorded in Microstructured Polymer Optical Fibre," in *Optical Fiber Sensors* (OSA, 2006), p. ThE64.

103. A. Abang and D. J. Webb, "Effects of annealing, pre-tension and mounting on the hysteresis of polymer strain sensors," Meas. Sci. Technol. **25**, 15102 (2014).

104. D. Sáez-Rodríguez, K. Nielsen, H. K. Rasmussen, O. Bang, and D. J. Webb, "Highly photosensitive polymethyl methacrylate microstructured polymer optical fiber with doped core.," Opt. Lett. **38**, 3769–72 (2013).

105. K. E. Carroll, C. Zhang, D. J. Webb, K. Kalli, A. Argyros, and M. C. Large, "Thermal response of Bragg gratings in PMMA microstructured optical fibers.," Opt. Express **15**, 8844–8850 (2007).

106. J. Witt, M. Steffen, M. Schukar, and K. Krebber, "Investigation of sensing properties of microstructured polymer optical fibres," Proc. SPIE-The Int. Soc. Opt. Eng. **7714**, 77140F–77140F (2010).

107. I. P. Johnson, D. J. Webb, and K. Kalli, "Hydrostatic pressure sensing using a polymer optical fibre Bragg gratings," in *Proc. of SPIE*, J. Canning and G. Peng, eds. (2012), Vol. 8351, p. 835106.

108. W. Zhang, D. J. Webb, G. D. Peng, and A. Abang, "An intrinsic biochemical concentration sensor using a polymer optical fibre Bragg grating," Microstruct. Spec. Opt. Fibres **8426**, 842619-842619–8 (2012).

109. D. Sáez-Rodríguez, J. L. Cruz, I. Johnson, D. J. Webb, M. C. J. Large, and a. Argyros, "Water diffusion into UV inscripted long period grating in microstructured polymer fiber," IEEE Sens. J. **10**, 1169–1173 (2010).

110. S. W. James and R. P. Tatam, "Optical fibre long-period grating sensors: characteristics and application," Meas. Sci. Technol. **14**, R49–R61 (2003).

111. W. Yuan, A. Stefani, M. Bache, T. Jacobsen, B. Rose, N. Herholdt-Rasmussen, F. K. Nielsen, S. Andresen, O. B. Sørensen, K. S. Hansen, and O. Bang, "Improved thermal and strain performance of annealed polymer optical fiber Bragg gratings," Opt. Commun. **284**, 176–182 (2011).

112. D. Webb, K. Kalli, and C. Zhang, "Temperature sensitivity of Bragg gratings in PMMA and TOPAS microstructured polymer optical fibres," Proc. Soc. Photo-Optical Instrum. Eng. **6990**, L9900–L9900 (2008).

113. H. . Liu, H. . Liu, G. . Peng, and P. . Chu, "Observation of type I and type II gratings behavior in polymer optical fiber," Opt. Commun. **220**, 337–343 (2003).

114. T. A. Birks, J. C. Knight, and P. S. J. Russell, "Endlessly single-mode photonic crystal fiber,"

22, 961–963 (1997).

115. C. A. F. Marques, L. B. Bilro, N. J. Alberto, D. J. Webb, and R. N. Nogueira, "Narrow bandwidth Bragg gratings imprinted in polymer optical fibers for different spectral windows," Opt. Commun. **307**, 57–61 (2013).

116. G. Statkiewicz-Barabach, K. Tarnowski, D. Kowal, P. Mergo, and W. Urbanczyk, "Fabrication of multiple Bragg gratings in microstructured polymer fibers using a phase mask with several diffraction orders.," Opt. Express **21**, 8521–34 (2013).

117. A. Stefani, S. Andresen, W. Yuan, N. Herholdt-Rasmussen, and O. Bang, "High sensitivity polymer optical fiber-Bragg-grating-based accelerometer," Photonics Technol. Lett. IEEE **24**, 763–765 (2012).

118. W. Yuan, A. Stefani, and O. Bang, "Tunable polymer fiber Bragg grating (FBG) inscription: Fabrication of dual-FBG temperature compensated polymer optical fiber strain sensors," IEEE Photonics Technol. Lett. **24**, 401–403 (2012).

119. G. D. Peng, Z. Xiong, and P. L. Chu, "Photosensitivity and gratings in dye-doped polymer optical fibers," Opt. Fiber Technol. **5**, 242–251 (1999).

120. T. Baghdasaryan, T. Geernaert, F. Berghmans, and H. Thienpont, "Geometrical study of a hexagonal lattice photonic crystal fiber for efficient femtosecond laser grating inscription," Opt. Express **19**, 7705–16 (2011).

121. J. Capodagli and R. Lakes, "Isothermal viscoelastic properties of PMMA and LDPE over 11 decades of frequency and time: A test of time-temperature superposition," Rheol. Acta **47**, 777–786 (2008).

122. B. T. Kuhlmey, R. C. McPhedran, and C. Martijn de Sterke, "Modal cutoff in microstructured optical fibers.," Opt. Lett. **27**, 1684–6 (2002).

123. D. X. Yang, J. Yu, X. Tao, and H. Tam, "Structural and mechanical properties of polymeric optical fiber," Mater. Sci. Eng. A **364**, 256–259 (2004).

124. W. Zhang and D. J. Webb, "Humidity responsivity of poly (methyl methacrylate) - based optical fiber Bragg grating sensors," **39**, 3026–3029 (2014).

125. H. F. Brinson and L. C. Brinson, *Polymer Engineering Science and Viscoelasticity* (Springer US, 2015).

126. A. Abang and D. J. Webb, "Influence of mounting on the hysteresis of polymer fiber Bragg grating strain sensors.," Opt. Lett. **38**, 1376–8 (2013).

127. G. Wild and S. Hinckley, "Acousto-Ultrasonic Optical Fiber Sensors: Overview and State-of-the-Art," IEEE Sens. J. **8**, 1184–1193 (2008).

128. A. Stefani, "Bragg Grating Based Sensors in Microstructured Polymer Optical Fibers : Accelerometers and Microphones," Ph.D. Thesis, Technical University of Denmark (2011).

129. I.-L. Bundalo, R. Lwin, S. Leon-Saval, and A. Argyros, "All-plastic fiber-based pressure sensor," Appl. Opt. **55**, 811 (2016).

130. K. Kalli and A. Othonos, *Fiber Bragg Gratings: Fundamentals and Applications in Telecommunications and Sensing* (Artech House, 1999).

131. D. Kowal, G. Statkiewicz-Barabach, P. Mergo, and W. Urbanczyk, "Microstructured polymer optical fiber for long period gratings fabrication using an ultraviolet laser beam," Opt. Lett. **39**, 2242 (2014).

132. M. C. J. Large, J. Moran, and L. Ye, "The role of viscoelastic properties in strain testing using microstructured polymer optical fibres (mPOF)," Meas. Sci. Technol. **20**, 34014 (2009).

133. I. P. Johnson, D. J. Webb, K. Kalli, M. C. J. Large, and A. Argyros, "Multiplexed FBG sensor recorded in multimode microstructured polymer optical fibre," Proc. SPIE-The Int. Soc. Opt.

Eng. **7714**, 77140D–77140D (2010).

134. H. Dobb, K. Carroll, D. J. Webb, K. Kalli, M. Komodromos, C. Themistos, G. D. Peng, a Argyros, M. C. J. Large, M. a van Eijkelenborg, Q. Fang, and I. W. Boyd, "Grating based devices in polymer optical fibre - art. no. 618901," Opt. Sens. II **6189**, 18901 (2006).

135. S. Poeggel, D. Tosi, D. Duraibabu, G. Leen, D. McGrath, and E. Lewis, "Optical Fibre Pressure Sensors in Medical Applications," Sensors **15**, 17115–17148 (2015).

136. D. H.-C. Wang, N. Blenman, S. Maunder, V. Patton, and J. Arkwright, "An optical fiber Bragg grating force sensor for monitoring sub-bandage pressure during compression therapy," Opt. Express **21**, 19799–19807 (2013).

137. E. M. M. Quigley, "What we have learned about colonic motility: normal and disturbed.," Curr. Opin. Gastroenterol. **26**, 53–60 (2010).

138. J. W. Arkwright, I. D. Underhill, S. a Maunder, N. Blenman, M. M. Szczesniak, L. Wiklendt, I. J. Cook, D. Z. Lubowski, and P. G. Dinning, "Design of a high-sensor count fibre optic manometry catheter for in-vivo colonic diagnostics.," Opt. Express **17**, 22423–22431 (2009).

139. P. G. Dinning, L. Wiklendt, I. Gibbins, V. Patton, P. Bampton, D. Z. Lubowski, I. J. Cook, and J. W. Arkwright, "Low-resolution colonic manometry leads to a gross misinterpretation of the frequency and polarity of propagating sequences: Initial results from fiber-optic high-resolution manometry studies," Neurogastroenterol. Motil. **25**, 640–649 (2013).

140. J. W. Arkwright, N. G. Blenman, I. D. Underhill, S. a Maunder, M. M. Szczesniak, P. G. Dinning, and I. J. Cook, "In-vivo demonstration of a high resolution optical fiber manometry catheter for diagnosis of gastrointestinal motility disorders.," Opt. Express **17**, 4500–4508 (2009).

141. D. Ganziy, O. Jespersen, B. Rose, and O. Bang, "An efficient and fast detection algorithm for multimode FBG sensing," in *Proceedings of the Optical Fiber Sensors Conference, Curitiba, Brazil,* (2015), Vol. 1, pp. 2–5.

142. FBGS, "FBGs Draw Tower Gratings," http://www.fbgs.com/productsadv/be-en/6/detail/item/15/page/1/.

143. A. Argyros, "Microstructures in Polymer Fibres for Optical Fibres, THz Waveguides, and Fibre-Based Metamaterials," ISRN Opt. **2013**, 1–22 (2013).

144. J. H. Osório, J. G. Hayashi, Y. a V Espinel, M. a R. Franco, M. V Andrés, and C. M. B. Cordeiro, "Photonic-crystal fiber-based pressure sensor for dual environment monitoring.," Appl. Opt. **53**, 3668–72 (2014).

145. J. G. Hayashi, C. M. B. Cordeiro, M. a. R. Franco, F. Sircilli, and C. J. S. de Matos, "Numerical and Experimental Studies for a High Pressure Photonic Crystal Fiber Based Sensor," AIP Conf. Proc. **1055**, 133–136 (2008).

146. W. N. MacPherson, E. J. Rigg, J. D. C. Jones, V. V. R. K. Kumar, J. C. Knight, and P. S. J. Russell, "Finite-element analysis and experimental results for a microstructured fiber with enhanced hydrostatic pressure sensitivity," J. Light. Technol. **23**, 1227–1231 (2005).